Novel applications of ground-penetrating radar in oil fields

Zhou, F.

DOI
10.4233/uuid:467f9f64-ae55-4e66-be24-0d0cb5f46fc4

Publication date
2020

Document Version
Final published version

Citation (APA)
Zhou, F. (2020). *Novel applications of ground-penetrating radar in oil fields*. [Dissertation (TU Delft), Delft University of Technology]. https://doi.org/10.4233/uuid:467f9f64-ae55-4e66-be24-0d0cb5f46fc4

NOVEL APPLICATIONS OF GROUND-PENETRATING RADAR IN OIL FIELDS

About the author:
Feng Zhou was born in Hubei Province, China in 1979. In 2002, he received a B.Sc. degree in Telecommunication Engineering at The Second Artillery Command College, China. In 2007, he completed an M.Sc. degree in Solid Earth Geophysics at China University of Geosciences (Wuhan). Thereafter, he pursued his Ph.D. study at the same university and completed his first doctorate degree in 2011. From Oct. 2009 to Nov. 2010, he worked at Delft University of Technology as a visiting scholar, funded by a NUFFIC grant. In 2013, under the supervision of Prof. Evert Slob, he started pursuing his second doctorate degree in Geophysics and Petrophysics at Delft University of Technology. His research areas to date include ground-penetrating radar, borehole geophysics, reservoir simulations, and their engineering applications.

Publisher : Gildeprint, The Netherlands
Release Date : 2020-12-10
Genre: Science
Pages : 128
ISBN: 978-94-6384-183-2

NOVEL APPLICATIONS OF GROUND-PENETRATING RADAR IN OIL FIELDS

Feng ZHOU

NOVEL APPLICATIONS OF GROUND-PENETRATING RADAR IN OIL FIELDS

Feng ZHOU

INVITATION

You are cordially invited to the public defense of my doctoral thesis

NOVEL APPLICATIONS OF GROUND-PENETRATING RADAR IN OIL FIELDS

Challenge the Future

on

Monday, January 18th, 2021, at 12:00 am, in the Committee 2, 2nd floor of the Aula Delft, Mekelweg 5, 2628 CC Delft.I will give a presentation before my defence at 12: 00 am.

Feng ZHOU

NOVEL APPLICATIONS OF GROUND-PENETRATING RADAR IN OIL FIELDS

551836-L-bw-Zhou
Processed on: 27-11-2020

NOVEL APPLICATIONS OF GROUND-PENETRATING RADAR IN OIL FIELDS

Dissertation

for the purpose of obtaining the degree of doctor
at Delft University of Technology
by the authority of the Rector Magnificus prof.dr.ir. T.H.J.J. van der Hagen
chair of the Board for Doctorates
to be defended publicly on
Monday 18 January 2021 at 12:30 o'clock

by

Feng ZHOU

Master of Science in Solid Earth Geophysics,
China University of Geosciences (Wuhan), China,
born in Danjiangkou, China.

This dissertation has been approved by the promotor:

Prof.dr.ir E.C. Slob

Composition of the doctoral committee:

Rector Magnificus	chairman
Prof.dr.ir. E.C. Slob	Delft University of Technology, promotor
Independent members:	
Prof.dr. A. Yarovoy	Delft University of Technology
Prof.dr. P. Zitha	Delft University of Technology
Dr. D. Voskov	Delft University of Technology
Dr.ir. B. Kooij	Delft University of Technology
Prof.dr. S. Lambot	Université Catholique de Louvain, Belgium
Other member:	
Prof.dr. A. Giannopoulos	University of Edinburgh, The United Kingdom

The work presented in this thesis was primarily conducted at Delft University of Technology, Delft, the Netherlands, and China University of Geosciences (Wuhan), Wuhan, China. The research was funded by the National Natural Science Foundation of China (41304078, 41674138, 41811530749), the NWO Cooperation and Exchange Fund (040.22.011/7048), the China Scholarship Council grant (201806415048), and the program of HPC-EUROPA3 (INFRAIA-2016-1-730897).

Keywords: Ground-penetrating radar, Borehole geophysics, Enhanced oil recovery, Reservoir estimation

Printed by: Gildeprint, the Netherlands

Front & Back: Feng Zhou

ISBN 978-94-6384-183-2

The electronic version of this dissertation is available at
http://repository.tudelft.nl/.

It always seems impossible until it is done

Nelson Mandela

SUMMARY

Ground-penetrating radar (GPR), usually working in the frequency from tens of megahertz to several gigahertz, is widely applied in mapping near-surface applications. In recent decades, GPR is frequently utilized for fluid-related applications, such as groundwater assessment, contaminant monitoring, and water-filled fracture detection, based on the principle that at these radar frequencies, electromagnetic (EM) waves are sensitive to water content. When operated from the surface, ground-penetrating radars are limited to a survey depth up to tens of meters in most soils. To further extend the detection range, borehole radar is developed by placing the GPR antennas in boreholes close to the underground targets. Different downhole survey modes, e.g. single-hole, cross-hole, and vertical radar profiling measurements, have demonstrated applicabilities for fracture detection, metal ore exploration, or water content prediction, up to a depth of a few hundred meters from the ground. Deeper GPR measurements in hydrocarbon reservoirs have been proposed. Some theoretical studies have shown that a borehole radar is expected to have the capability of mapping structures in the range of a few decimeters to ten meters away from the borehole in most reservoir environments, filling in the gap of the conventional electrical, sonic and nuclear logging methods. More attractively, GPR has a relatively high radial resolution and suits best for the downhole structure and fluid imaging. This thesis aims to explore the potential applications of GPR and assess their values in these oil industry applications. Applicability studies are carried out in the fields of well logging and monitoring of oil production. Numerical simulations are carried out, where joint multiphase flow and borehole radar modelling is established.

Estimating reservoir permeability is proposed as one of the potential applications of borehole radar in oil exploration area. In oil drilling, mud filtrate penetrates into porous formations and displaces the in-situ fluids. The invasion depth is a key indicator of the reservoir permeability because permeability controls the invasion rate. As the permeability varies as a function of the formation depth, the invasion depth varies accordingly. Thus, if the invasion front is finely logged, the permeability curve can be depicted. Unfortunately, the conventional logging tools have no such a high radial resolution to properly determine the invasion depth. With a working frequency of 1 GHz, borehole radar is able to capture the reflection signals generated by the invasion front and subsequently to derive the invasion depth. Time-lapse radar logging with one-transmitting and two-receiving antennas is used to compute a high-resolution image of the invasion depth profile. A logging interpretation chart is established to link the permeability and invasion depth with the required prior knowledge. The proposed methodology proves to effectively and accurately estimate the permeability curve for a realistic reservoir scenario. Low-porosity and low-permeability oil-bearing reservoirs invaded by fresh water-based mud form the ideal application environment.

The recently developed intelligent well (smart well) production technology inspires another potential application of borehole radar in an oil field. Intelligent wells, incorporating downhole monitoring and inflow control technology, allow for sectionalized production strategies to improve the recovery efficiency. Currently, the optimization strategy is constrained by downhole monitoring techniques in the well. This so-called in-well monitoring, whether pressure, temperature or phase sensing, can not activate inflow control policies until the unwanted fluids are flowing into the production well. Conventional fluid imaging methods, exemplified by streaming potential and 4D seismic, are applied to water-flooding productions with a scale from hundreds to thousands of meters. For some reservoir production cases, such as thin oil rims driven by bottom water, steam assisted gravity drainage, and bilateral water sink production, a monitoring range from few meters to ten meters is required. Borehole radar with a working frequency of 100 MHz can satisfy the requirements of the detection range and spatial resolution. A downhole radar imaging technology is proposed by mounting an array of radar sensors along the casing of a production well to monitor the oil-water displacement dynamics. Obtaining real-time information of the flowing oil-water contact, a feedback control production strategy of a smart well is proposed to optimize the oil recovery. Quantitative comparisons are carried out among three different production strategies derived by different monitoring methods to assess the economic values of the borehole radar imaging in oil production. The comparisons show that a production strategy combined with the in-well sensing and borehole radar imaging can accelerate oil production and suppress water production, and thus obtain more net present values than a single monitoring and control method, implying that borehole radar is a promising reservoir monitoring technology and has potentials to improve recovery efficiency.

The proposed borehole radar logging and monitoring methods demonstrate promising applications of GPR in the petroleum exploration and production, respectively. The primary strengths of borehole radar in oil fields are its high-radial resolution and proper detection range, which cover the gap of the current geophysical prospecting methods in oil fields. Challenges mainly exist at technical levels. Novel borehole radar systems are expected to be developed, which are able to steadily work in a permanent downhole environment or be implemented in elaborate logging operations in an open hole.

CONTENTS

Summary vii

1 Introduction 1
- 1.1 Background . . . 2
  - 1.1.1 GPR introduction and borehole radar development . . . 2
  - 1.1.2 Problem descriptions in well logging . . . 3
  - 1.1.3 Problem descriptions in reservoir monitoring . . . 5
- 1.2 Motivations . . . 7
- 1.3 Research objectives and methods . . . 8
- 1.4 Thesis organization . . . 9

2 Extracting mud invasion signals using borehole radar reflection measurements 11
- 2.1 Introduction . . . 12
- 2.2 Modelling . . . 13
  - 2.2.1 Numerical modelling . . . 13
  - 2.2.2 Reservoir scenario . . . 13
  - 2.2.3 Antenna placement . . . 15
- 2.3 Survey method . . . 19
  - 2.3.1 Time-lapse logging . . . 19
  - 2.3.2 Time interval of time-lapse logging . . . 22
  - 2.3.3 Detection range . . . 22
- 2.4 Sensitivity analyses . . . 29
  - 2.4.1 Effects of viscosity . . . 29
  - 2.4.2 Effects of porosity . . . 29
  - 2.4.3 Effects of mud salinity . . . 32
  - 2.4.4 Effects of formation water salinity . . . 34
  - 2.4.5 Effects of diffusion coefficient . . . 36
- 2.5 Conclusions . . . 38

3 Estimating reservoir permeability with borehole radar 41
- 3.1 Introduction . . . 42
- 3.2 Numerical modelling . . . 43
  - 3.2.1 Mud invasion modelling and reservoir scenario . . . 43
  - 3.2.2 Borehole radar configuration and modelling . . . 45
  - 3.2.3 Fluid distribution and radar responses . . . 49
- 3.3 Permeability estimation . . . 53
  - 3.3.1 Estimation of invasion depth . . . 53
  - 3.3.2 Estimating permeability . . . 55

3.4 Conclusions . . . 61

4 Reservoir monitoring using borehole radars to improve oil recovery: Suggestions from 3D EM and fluid modelling 63
4.1 Introduction . . . 65
4.2 Water front monitoring using borehole radar . . . 68
4.2.1 Flow modelling . . . 68
4.2.2 Radar modelling . . . 68
4.2.3 EM responses . . . 74
4.3 Production controls combined with borehole radars . . . 75
4.3.1 Reservoir imaging with radar array . . . 75
4.3.2 Production strategies . . . 80
4.4 Conclusions . . . 87

5 Conclusions 89
5.1 Summary . . . 90
5.2 Future Work . . . 91

Appendices 93

A Mathematical expressions of mud invasion 95
A.1 Multiphase and multicomponent formulas . . . 95
A.2 Rock electrical formulas . . . 96
A.3 Formulas of mud cake growth . . . 97

References 99

List of publications relevant to this work 113

Curriculum Vitæ 115

Acknowledgments 117

1

INTRODUCTION

SUMMARY
Ground-penetrating radar (GPR) is a geophysical tool to obtain subsurface information at high spatial resolution. It has been widely applied in near surface environments. Over the last decades, GPR has become increasingly popular in hydrogeological applications for the significant permittivity contrast between water and the other soil and rock components. Time-lapse GPR measurements have advantages in dynamic fluid monitoring because GPR signals can be enhanced by the changes of saturations over time. Currently, fluid monitoring by GPR mainly focuses on shallow surface, but deep environments are more and more the recent subjects. Borehole radar conducts a survey by placing antennas in a borehole at the depth from tens to hundreds of meters. We think borehole radar can be applied in deeper hydrocarbon reservoirs for oil exploration and production applications. In oil exploration, borehole radar can be applied in well logging to detect mud invasion, thereby evaluating reservoir permeability. In oil production, borehole radar is expected to monitor the time evolution of water-oil displacement, supporting production optimization. Numerical model is established to carry out a feasibility investigation by coupling a multiple phase flow model with a borehole radar model. Borehole radar antennas are designed for the proposed reservoir applications. Time-lapse measurements are carried out to extract the signals reflected from the fluid boundary. Borehole measurement methods are studied for the respective application scenarios. Mud invasion depth is derived in well logging application, and water front advancement is imaged in reservoir monitoring. The achieved results are utilised to assess the potentials of borehole radar in reservoir estimation and enhanced oil recovery, respectively.

1

1.1. BACKGROUND

1.1.1. GPR INTRODUCTION AND BOREHOLE RADAR DEVELOPMENT

Ground-penetrating radar (GPR), also known as georadar, subsurface radar, and ground-probing radar, is an electromagnetic (EM) detection tool that works at the frequency ranging from megahertz to gigahertz [1]. It can be used in many different nondestructive testing or geophysical methods with specific antenna configurations, working bandwidth and operation sequences, being dedicated to achieving a goal. GPR transmits radio waves into the subsurface materials through antennas. When the propagating EM waves encounter an interface between different EM properties, parts of EM energy are scattered and the echoes are recorded by GPR receiving antennas. By analysing the characteristics of the amplitude, phase or travel time of the received waveforms, one can infer or interpret the location, structure or texture of subsurface targets. Basic principles and methods of GPR can be found in several comprehensive textbooks [2,3], and general statements will not be presented here.

In the past decades, GPR has demonstrated to be an effective tool for shallow subsurface imaging, and has been successfully applied in a diversity of areas. Examples include: geological investigations [4,5], archaeological study [6,7], utility detection [8,9], pavement inspection [10,11], forensic investigations [12,13], unexploded ordnance (UXO) exploration [14,15], outer space exploration [16,17], etc. Deep investigation is only possible in a highly resistive material. A typical example is the glacial detection with surface radar in Antarctica, where the survey depth is up to a few thousand meters [18,19].

Conventional surface radar has a limited investigation depth. Specific applications require that data are recorded close to a deep target, and this is achieved by placing GPR antennas in boreholes, which extends the concept of GPR from surface radar to borehole radar [1]. Borehole radar has been used in some special geophysical exploration areas, such as mining [20], cavity imaging [21], fracture characterization [22], and hydrogeophysical investigations [23]. Compared with the conventional surface-penetrating radar, borehole radar is able to work in a much deeper formation, which therefore extends the investigation range. However, the expense is that it has to work in a more complicated environment than at the surface, which means the facilities have to be sophisticated. In the 1970s, Holser *et al.* developed a simple transient pulse borehole radar system with the center frequency of 230 MHz. They tested the system in a salt dome located in Louisiana, USA, finding that the received reflected signals succeeded in depicting the shape of the salt dome [24]. In the 1980s, Nickel *et al.* measured the salt dome at a depth of 3000 m using the developed transient pulse and FMCW (frequency modulated continuous wave) borehole radars, respectively, and captured the structure of basalt and clay inside the salt [25]. In the same decade, the Organization for Economic Cooperation and Development (OECD) launched a so-called international Stripa programme to develop a downhole tool to assess deep fractures and their hydraulic characteristics in nuclear waste sites [26]. In this programme, a directional borehole radar system was developed to conduct a single hole, cross hole and tomography measurement [27]. In the early 2000s, van Dongen *et al.* and Waard *et al.* developed a three-dimensional directional borehole system by installing an arc-shaped reflector behind a cylindrical

dipole antenna, and their single-borehole reflection survey presented a high azimuthal resolution for a near-borehole object [28,29]. Soon afterwards, the U.S. Geological Survey (USGS) developed a three-dimensional directional borehole radar prototype with cavity-backed monopole antennas, and they used it for fracture mapping in a crystalline rock formation [30]. Pisani *et al.* adopted their developed borehole radar to conduct a single borehole reflection survey in a gold mine located in South Africa, and delineated the three-dimensional structure of the gold deposit [31]. Mason *et al.* investigated guided wave phenomena in a fluid-filled borehole, and analysed the effects on the received signals for the cases of monostatic and bistatic antenna modes [32]. In the recent decades, the Commonwealth Scientific and Industrial Research Organization (CSIRO) of Australia utilized the guided waves of borehole radar to predict the drilling depth in coal mines [33,34]. Tohoku University of Japan has been dedicated to developing a fully polarimetric borehole radar to image the structures and hydraulic properties of the subsurface fracture systems [35–37].

The GPR applications mentioned above mainly focus on the ground or in the shallow subsurface (from tens to hundreds of meters). However, its applications in deep environments (up to thousands of meters) become more and more attractive. Some theoretical and experimental studies of GPR applications in deep oil wells and reservoirs have been carried out [38–42]. We think that the potential applications of borehole radar in oil fields could reside in well logging and production monitoring. In both fields, GPR sensors could be placed in a deep wellbore to detect an oil-water contact based on the fact that significant EM reflection occurs at the oil-water contact because of the large electrical property contrast between them.

1.1.2. PROBLEM DESCRIPTIONS IN WELL LOGGING

During the drilling process, mud is injected into the drilled borehole to keep a slightly higher pressure with respect to the formation pressure for the purpose of maintaining the borehole stability. Under the pressure difference, mud filtrate penetrates into the permeable formation and alters the components and fractions of the pore fluids, and therefore changes the electrical properties of the near-borehole zone. This is the so-called “mud invasion” phenomenon often encountered in oil logging. The invasion of mud filtrate into permeable formations is responsible for the development of mud cake (solids deposition) on the borehole wall, as well as for the displacement of existing in-situ fluids laterally away from the borehole [43]. There are several different types of drilling mud according to their respective compositions and application conditions. Regular categories are fresh water-based mud, salt water-based mud, oil-based mud, synthetic-based mud, and pneumatic drilling mud. Water-based mud is the most widely used, by which approximately 80 % of wells are drilled because of its less expensive and more environmental friendliness than the others [44]. Figure 1.1 schematically presents a typical mud invasion process and the resulting formation disturbance. It can been seen that the near-borehole formation is explicitly divided into three zones according to the different fractions of components and phases. The first zone, which is closely adjacent to the borehole wall, is a flushed zone, where almost all the original (or in-situ)

1

formation fluids are displaced away from the borehole; the second zone is a transition zone which contains a mixture of the in-situ fluids and the invading mud filtrate; and the third zone is the virgin (un-invaded) zone which starts at a certain distance from the borehole and is not affected by the mud filtrate [45]. Mud properties and drilling operation variables, such as mud density and chemical constituents, downhole circulation pressure, and filtration time, make significant effects on the inflow rate and spatial distribution status of mud-filtrate invasion. In-situ rock formation properties, such as porosity, absolute permeability, relative permeability, pore pressure, shale chemistry, capillary pressure, and residual fluid saturations, play important roles in controlling both the dynamic growth of the mud cake and the time evolution of the invasion [43].

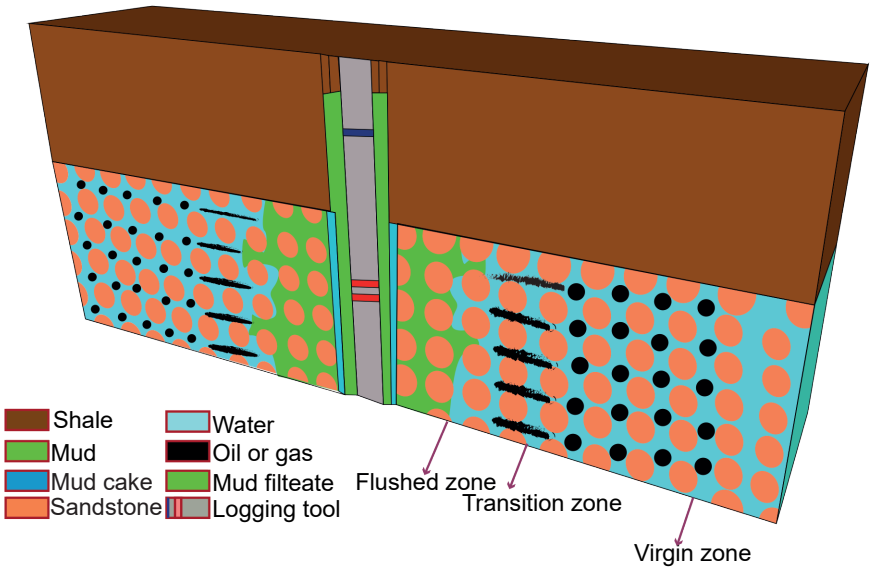

Figure 1.1: Schematic presentation of mud invasion [45].

Mud invasion effects bring disturbance to conventional well logging signals, therefore creating considerable biases on the shallow-reading logging data, such as density, neutron porosity and microlog loggings, which can lead to inaccurate evaluation of reservoir properties. Industry has paid much attention to the mud invasion effects, and has tried to eliminate the negative effects by correcting logging data. Nevertheless, log interpreters find out that the process of mud filtrate flushing in-situ formation presents also an opportunity to study the reservoir hydrodynamic characters [46]. Salazar *et al.* quantitatively analysed how the invasion rate is influenced by the reservoir properties, and inverted porosity, initial water saturation and permeability with array induction logging data [47,48]. Liang *et al.* estimated the reservoir properties using joint induction logging and pressure transient data by means of the invasion rate information [49]. Zhou *et al.* systematically analysed the correlations between the invasion depth and

reservoir properties, especially the initial water saturation, permeability and porosity [50]. However, the existing logging tools provide low radial resolutions and thus low accuracy for the inverted invasion profile. A novel logging tool with higher frequency could solve this problem.

1.1.3. PROBLEM DESCRIPTIONS IN RESERVOIR MONITORING

Potential application of GPR in production environments lies in reservoirs produced with the so-called "smart wells". Smart well (intelligent well) is a well equipped with downhole sensors and inflow control valves (ICVs) to produce hydrocarbons from a reservoir in a measurement and control environment, with the aim to significantly improve oil recovery or net present value (NPV) [51]. However, the realizable smart well production strategies in the oil fields rely on the accurate descriptions of fluid behaviors in reservoirs or wells, and some data can only be acquired by permanently installed downhole sensors [51,52]. Examples of currently applied production monitoring technologies include pressure sensors, temperature sensors and multiphase flow meters [53–56]. Generally, these tools can only monitor the fluid changes inside or closely adjacent to a well [52]. For sensing further away from the well, 4D seismic data and steaming potential measurements are applied [57,58]. Such methods are effective to monitor the fluid movement far away from the well in an order of tens to hundreds meters, whereas have difficulties to resolve the near-well region from several to tens of meters [58,59]. However, in some specific reservoir environments, monitoring of that range is required. Some examples, where successful capture of fluid dynamics in near-well regions is able to increase production by smart wells, are thin oil rim reservoirs, steam assisted gravity drainage (SAGD), and bilateral water sink drainage (BWS) produced by horizontal wells.

Thin oil rim reservoirs are relatively thin oil columns (in the order of a few to tens of meters) sandwiched between water and gas or shale. Their production often leads to early water breakthrough in the case of horizontal well production caused by reservoir heterogeneity and wellbore pressure drop [60]. Figure 1.2 presents a typical thin oil rim driven by bottom water.

SAGD is an enhanced oil recovery technology for heavy crude oil recovery. Two horizontal wells are parallelly drilled in the reservoir, one about 4 to 6 meters above the other. The upper well injects steam into the reservoir to lower the viscosity of the heavy crude oil, causing the heated oil to drain into the lower well driven under gravity [62]. The main challenge is to let the steam chamber grow in a controllable way, insuring the steam or condensed water is not produced at the lower well. Figure 1.3 graphically represents an SAGD production model.

A problem for the conventional horizontal well production under bottom water drive is that water invades the well by water coning or cresting. BWS production scheme is proposed by extending two parallel lateral branches from the production well, conducting a synchronal production of oil in the oil-bearing layer and water in the

1

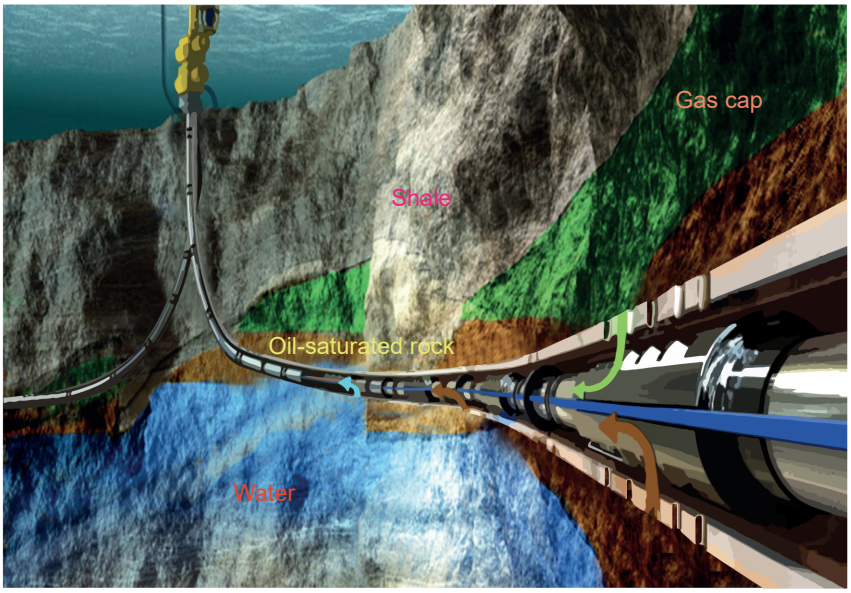

Figure 1.2: Schematic presentation of thin oil rim produced by a horizontal well. The blue, brown and green colors stand for bottom water, oil-saturated rock, and gas cap, respectively [61].

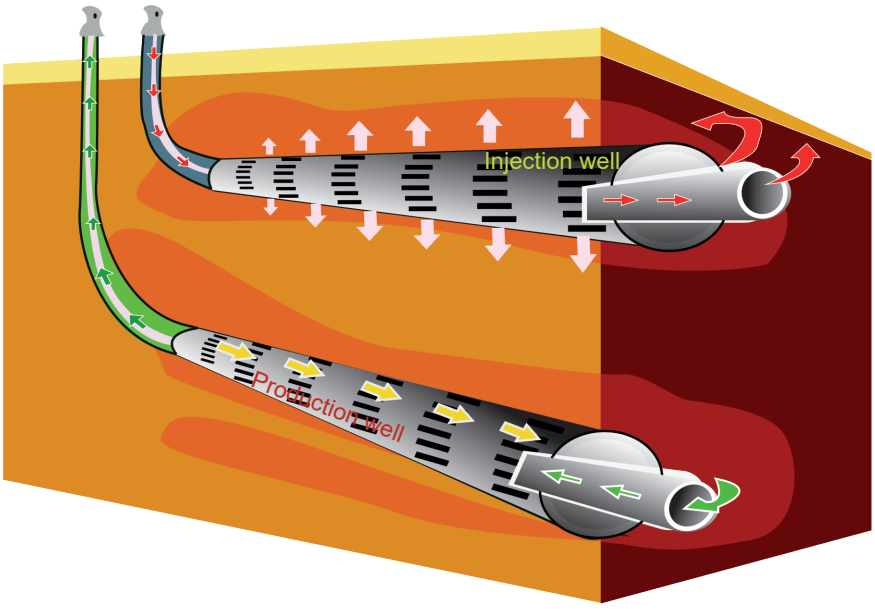

Figure 1.3: Schematic presentation of SADG production in heavy oil [63].

aquifer [64]. Figure 1.4 presents a simple model of BWS production in thin oil rim. By separating oil and water production using two (upper for oil and lower for water) parallel lateral sections of the same well, the pressure drop is greatly relieved and the movement of water front is slowed down, entailing a long period of water-free production [65]. Qin *et al.* designed a BWS production scheme in a heavy oil reservoir with strong bottom water drive [65]. To develop an effective BWS technology, the key issue is to control the respective production rates of the lateral segments. However, the potential problem is that it is difficult to predict the water coning movement. Although an analytical model was developed to calculate the respective production rates for a steady water coning or cresting control [66], it only presents a rough prediction and can not be effectively applied in realistic heterogeneous reservoirs, especially when considering the heel-toe effect that occurs in a horizontal well production. If a real-time monitoring of water coning or cresting would be available, a dynamic production rate control scheme can be implemented in the oil and water branches to maximize recovery.

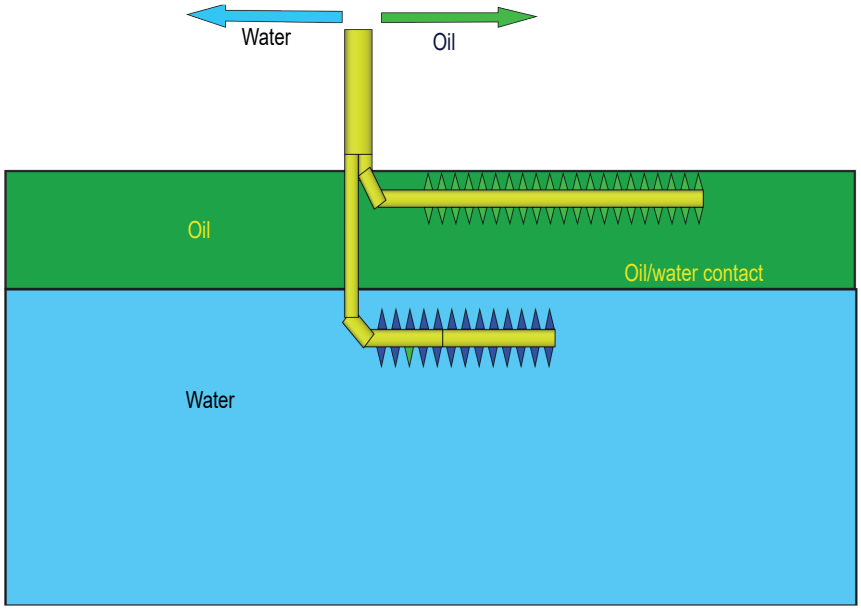

Figure 1.4: Schematic presentation of BWS production [64].

1.2. MOTIVATIONS

GPR is becoming increasingly popular in hydrogeological studies because of the significant permittivity or conductivity contrast between water and other soil and rock components [67,68]. Time-lapse GPR measurements have been extensively used to monitor flowing-related phenomena, e.g., the saturation changes of water or steam in fractures or vadose zones [69–75]. That is because the time-lapse measurements can

remove the waves from the unchanged parts and extract the reflection signals from the flowing parts. This inspires us to conduct a time-lapse borehole radar measurement in deep oil reservoirs to monitor the flowing oil-water contact involved in the above mentioned issues.

In the process of mud invasion, different fractions of phases and chemical components are formed in the near-borehole regions, thereby changing formation conductivity and permittivity distributions. When the electrical properties present distinct differences, boundaries are formed. Over the invasion time, the boundaries advance further away from the borehole wall. In the time scale of logging, the invasion depth of interest is not beyond 1 meter, and fine descriptions of the invasion profile are crucial for logging interpretation. A high-frequency (1 GHz) GPR tool has a spatial resolution of a few centimeters and penetrating range of approximately 1 meter in a high-resistivity reservoir environment [39], which could be a proper tool for the solving invasion-related problems. This is a very high frequency applied to well logging relative to the conventional logging tools, wherefore the EM waves propagation should keep low attenuation and phase distortion. Among the diverse mud types, fresh water-based and oil-based mud types have relatively low conductivity, and thus the EM attenuation and phase distortion of radar waves keeps in a low level in the borehole and the invaded formation. That signifies that the fresh water-based or oil-based mud is the favorable mud types for mud detection by borehole radar. In addition, the high-frequency logging tool is limited in an open-hole logging prior to the casing installation.

In the oil production scenarios mentioned above, the oil-water displacement front evolves within a range of approximately ten meters away from the production well. The electrical property profile is relatively simple compared with the mud invasion cases because there is only phase displacements and no salinity miscibility. A relatively low-frequency (few megahertz) borehole radar would be able to monitor the movement of oil-water contact in the interested range [41]. To map the shape of the advancing water front in a heterogeneous reservoir, an array of radar sensors could be installed outside the casing of a production well. Once the water front is imaged in a real-time manner, a production optimization scheme could be set up.

1.3. RESEARCH OBJECTIVES AND METHODS

The goal of this thesis is to investigate in depth the applicability of borehole radar to help determine necessary parameters for reservoir appraisal and production monitoring, and discuss their potential values in oil industries. Numerical investigations are conducted by linking an EM model to a fluid flow model.

In the applications of borehole radar in open-hole logging, the EM model is designed as a directional borehole radar with it antennas installed in a slot of the drill collar, and the flow model simulates a water-based mud filtrate invading an oil-bearing layer. One of the key issues in this part is to analyse the influences of fluid and rock properties on the electrical characteristics of the invaded formation and the corresponding effects

on the borehole radar responses. Additionally, it is significant to analyse the different components in radar reflection signals, and to extract the characteristic components arising from the invasion front, for which a time-lapse measurement is to be implemented. After obtaining the reflection signals from the invasion front, the invasion depth can be derived by a signal processing algorithm. Finally, the practicability of this method is examined for reservoir assessment by estimating the magnitude of hydraulic permeability (hereinafter referred as permeability) using the obtained invasion depth data at certain invasion times.

In the case of oil production, the EM model is designed as radar antennas permanently installed in the casing of a production well, and the flow model simulates an oil-bearing layer produced by a horizontal well under the derive of a bottom aquifer. By coupling the models, one can observe the real-time radar responses to the water front movement during oil recovery. By employing an array of borehole radars along the production well, an EM imaging scheme is studied for the capability of borehole radar array to reconstruct the water front profile. Finally, the water front imaging results are combined with a smart well feedback control strategy to investigate the economic value of borehole radar monitoring in oil production.

1.4. THESIS ORGANIZATION

The remainder of this thesis is organized as follows.

- **Chapter 2** investigates the logging method of borehole radar in a mud-filled borehole, and analyse the influences of formation and fluid properties on the radar signals.
- **Chapter 3** investigates the method of using borehole radar logging data to derive the mud invasion depth and associating the invasion depth with the permeability estimation.
- **Chapter 4** investigates the method of borehole radar array for imaging water front profile during oil recovery and using the imaging results to conduct a smart well feedback control production strategy.
- **Chapter 5** summarizes and concludes the work of the thesis, and recommends possible directions for future work.

2

EXTRACTING MUD INVASION SIGNALS USING BOREHOLE RADAR REFLECTION MEASUREMENTS

SUMMARY

In the oil drilling process, downhole mud filtrate penetrates the formation pores and alters the fluid distribution in near-borehole zones. Adequate understanding of the invasion status is crucial for logging interpretation and reservoir assessment. In theory, borehole radar logging can be used to extract mud invasion information. By testing a large variety of reservoir properties for realistic field scenarios in numerical models, the effects of rock and fluid properties on the radar signals are investigated. The results suggests that reservoir characteristics and radar tool placement play an important role and determine the reliability and accuracy. The signals reflected from the mud invasion front are sensitive to oil viscosity, porosity, mud salinity, formation water salinity and ionic diffusion coefficient. Time-lapse logging with an interval of six hours or more makes it possible to detect invasion depth between 0.15 m and 1 m away from the well.

The content of this chapter is based on the following paper:

F. Zhou, I. Giannakis, A. Giannopoulos, K. Holliger, and E. Slob, Extracting mud invasion signals from borehole radar measurements, *Geophysics*, under review.

2.1. INTRODUCTION

2

During drilling operations, mud filtrate tends to infiltrate a permeable reservoir under the pressure difference between the borehole and the formation. The invaded fluid displaces the in-situ fluids and alters the fluid compositions in the near-borehole zone. This is the so-called mud invasion, which is frequently encountered in oil drilling and well logging [76]. Mud invasion introduces disturbances into logging signals, which leads to difficulties in correct logging data interpretations or reservoir assessment [77]. Attempts have been made to correct the logging data by evaluating the mud invasion effects. A typical approach is to employ array electrical logging tools (such as array induction logging or array lateral logging) to obtain the apparent electrical resistivities at multiple radial depths, and sequentially invert the radial profiles of the invaded formation [78,79]. Three-parameter or five-parameter inversion algorithms are utilized to solve the invasion depth and the true resistivities of the flushed, virgin or transition zones by simplifying a gradual invasion zone into a piston-like shape [80,81]. Nevertheless, intrinsic non-uniqueness exits, which can lead to considerable errors in the inversion solutions, because such logging tools have low spatial resolution relative to the sophisticated fluid distribution. If some characteristic of mud invasion, for example, invasion depth, is accurately determined, the non-uniqueness of the solution can be eliminated or removed, and the properties of the virgin formation can be inverted accurately. On the other hand, invasion depth has proved to exhibit strong correlations with hydrodynamic characteristics of a reservoir, typically represented by permeability and porosity [50]. This allows for estimating these key petrophysical properties once the invasion depth is accurately measured [47,78]. Furthermore, the invasion depth is linked to predicting the productivity for the reason that the water-based mud invasion has a similar displacement mechanism with water-flooding recovery [82].

We propose to use borehole radar reflection measurements to obtain invasion depth information, considering that borehole radar operates at a much higher frequency and with much larger bandwidth than conventional logging tools. However, the accuracy with which the invasion depth can be obtained from borehole radar data heavily relies on extract extraction of the signals reflected from the invasion front. The challenges primarily originate from the complicated downhole environments and the gradually varying fluid distribution, which have large impacts on the quality of borehole radar signals. These inspire us to develop an elaborated downhole measurement method for borehole radar signal extraction. In the meanwhile, the diversity of reservoir types imposes some limitations or risks on the applications of borehole radar in well logging. This motivates us to analyse the influence of rock and fluid properties on the radar signals.

This chapter investigates how the signal quality of borehole radar is influenced by the logging operation and petrophysical properties. The study is carried out by numerical simulations. We analyse an effective signal extraction method and its limitations. Sensitivity to reservoir properties of radar signal quality is analysed by perturbing a wide variety of rock and fluid properties. The work in this chapter provides a valuable reference for practical applications of borehole radar in oil fields.

2.2. MODELLING

2.2.1. NUMERICAL MODELLING

A numerical model is established to simulate borehole radar logging in a mud-invaded reservoir by a coupled fluid flow and EM propagation modelling. The borehole radar model is established by gprMax, a general-purpose finite-difference time-domain EM simulator [83]. The antennas are modelled as Hertz dipole point-sources placed inside the cavities of a logging string. The transmitting antenna is excited by a Ricker wavelet with a center frequency of 1 GHz, and the working frequency is a compromise between the detection depth and spatial resolution in the investigated environment [39].

The mud invasion process is modelled as an oil and brine system in a sandstone displaced by fresh water under the pressure difference between the downhole mud and the in-situ formation. The convection and diffusion of the water, oil and salt ions alter the compositions and fractions of the pore fluids, thereby changing the bulk conductivity and permittivity of the saturated rock, as described in Appendixes A.1 and A.2. The dynamic growth of the mud cake is coupled with the fluid flow model, because it plays a significant role in the invasion rate, as described in Appendix A.3.

2.2.2. RESERVOIR SCENARIO

A reservoir scenario is simulated by the numerical model established above to investigate how the reservoir properties influence borehole radar signals. The reservoir consists of sandstone with a porosity of 15 % and permeability of 3 md, saturated with 30 % water and 70 % oil, and the salinities of formation water and mud filtrate are respectively 120×10^3 ppm and 1×10^3 ppm, representing a fresh-water mud invading an oil-bearing layer. The diffusion coefficient and dispersion coefficient of salt in the formation water are 6.45×10^{-9} m^2/s and 1.30×10^{-3} m. The viscosities of oil and water are 3.55 cp and 1.27 cp, respectively, standing for a conventional light oil reservoir. The rock surface is assumed to be water-wet, which is characterized by the capillary pressure and relative permeability curves. Table 2.1 presents the properties that define the capillary pressure and relative permeability curves according to equations A.5–A.7 in Appendix A.1. Table 2.2 presents the configuration parameters of the mud cake.

The relative permittivities of oil, water and sandstone are respectively 2, 57.93 and 4.65 at the reservoir temperature of 93.3 °C (200 °F). The frequency dependence of the permittivity of water is negligible at this temperature. Figure 2.1 presents the frequency-dependent permittivity of pure water measured at varying temperature. We can see that at the proposed working frequency and bandwidth, as the increase of the temperature, the relative permittivity of water dramatically drops and the frequency dependence becomes weak. The sandstone rock has a tortuosity factor of 1, cementation exponent of 2, and saturation exponent of 2.

Table 2.1: Capillary pressure and relative permeability properties [48].

Variables	*Values*	*Units*
Connate water saturation	0.15	fraction
Residual oil saturation	0.10	fraction
End-point value of relative permeability of water	0.30	fraction
End-point value of relative permeability of oil	1	fraction
Corey exponent of water	2.00	dimensionless
Corey exponent of oil	2.00	dimensionless
Capillary pressure coefficient	1.87×10^{-2}	Pa·m
Empirical exponent for pore-size distribution	5.00	dimensionless

Table 2.2: Mud cake properties [49].

Variables	*Values*	*Units*
Referenced permeability of mud cake	0.01	md
Referenced porosity of mud cake	0.40	fraction
Pressure difference between borehole and formation	4	MPa
Maximum thickness of mud cake	0.01	m
Volume percent of solid particles in mud	0.50	fraction
Compressibility exponent of mud cake	0.40	fraction
Exponent multiplier of mud cake	0.10	fraction

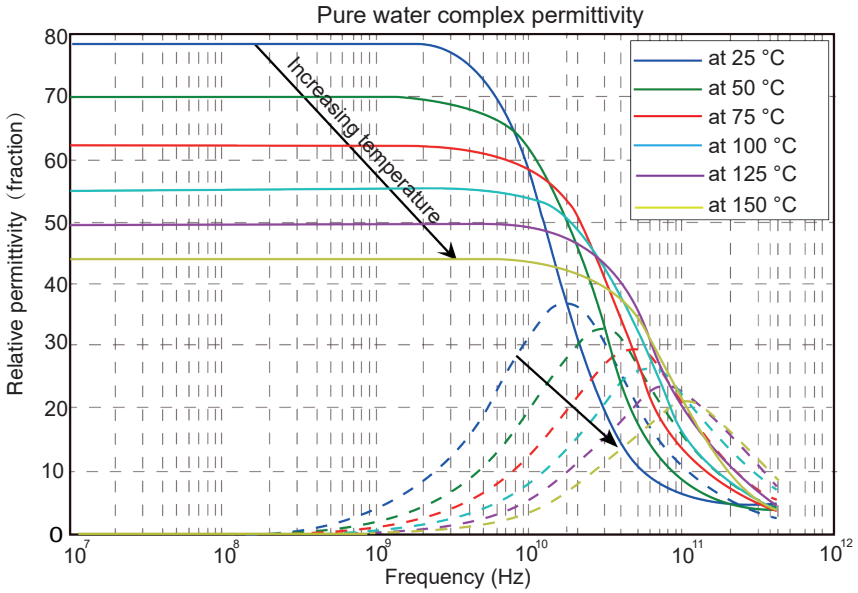

Figure 2.1: Complex relative permittivity of pure water versus EM frequency at varying temperature based on laboratory measurements [84]. The solid curves stand for the real part of the complex permittivity while the dash curves for the imaginary part.

Table 2.3: Geometric parameters and electrical properties of the designed borehole radar logging tool.

Variables	*Values*	*Units*
Logging string radius	0.05	m
First transmitter−receiver spacing	0.20	m
Second transmitter−receiver spacing	0.40	m
Radial depth of cavity	to be optimized	m
Longitudinal length of cavity	to be optimized	m
Relative permittivity of absorbing material	20-9i	dimensionless
Relative magnetic permeability of absorbing material	1.2-12i	dimensionless

2.2.3. ANTENNA PLACEMENT

Regarding the high-frequency EM survey in the downhole environment, two issues should be considered carefully when designing the borehole radar tool. One is to prevent the conductive mud from attenuating the high-frequency EM signals, and the other is to reduce EM interference from the metal components of the logging string as less as possible. To these ends, a backward caliper is hinged with the logging string to push the antennas against the borehole wall, and antennas are installed inside half-cylindrical cavities in the body of the logging tool backed by special EM absorbing material filled to attenuate the reflections from the backward radiated waves. One-transmitter and two-receiver mode is employed to conduct the time-to-depth conversion of radar signals. The basic configurations of the geometric parameters and EM absorbing properties of the logging tool are described in Table 2.3.

The backward radiated waves can not be completely removed, which leads to an apparently long radiated signal. This brings the risk that weak reflected signals are undistinguished from the tailings of EM waves, especially in the early-time signals. We optimise the geometry of the antenna cavities to reduce the effects of the ringings by fixing the EM absorbing material. The employed EM absorbing material in this study is a kind of ferrite with the dielectric loss and magnetic loss considered (see Table 2.3). This consideration is based on the fact that only limited types of EM absorbing materials exist in nature. We change the radial depth and longitudinal length of the antenna cavities, respectively, and observe the waveforms recorded by the two receivers in a homogeneous formation as shown in Figures 2.2 and 2.3. It is fairly noticed that, in this chapter, the amplitudes of the EM waves are illustrated in a logarithmic scale, which is beneficial for the visible comparisons between the strong direct wave and the weak reflected wave. The comparisons reveal that as the radial depth and longitudinal length of the antenna cavities increase, the ringings gradually become weak until invisible, while the direct waveforms almost keep the same amplitudes. The results suggest that the antenna cavity should be made as large as possible as long as the logging string supports. Therefore, we optimise the design of the borehole radar by enlarging the dimensions of antenna cavities, as illustrated in Figure 2.4. This borehole radar model will be used in the remaining simulations of the chapter.

2

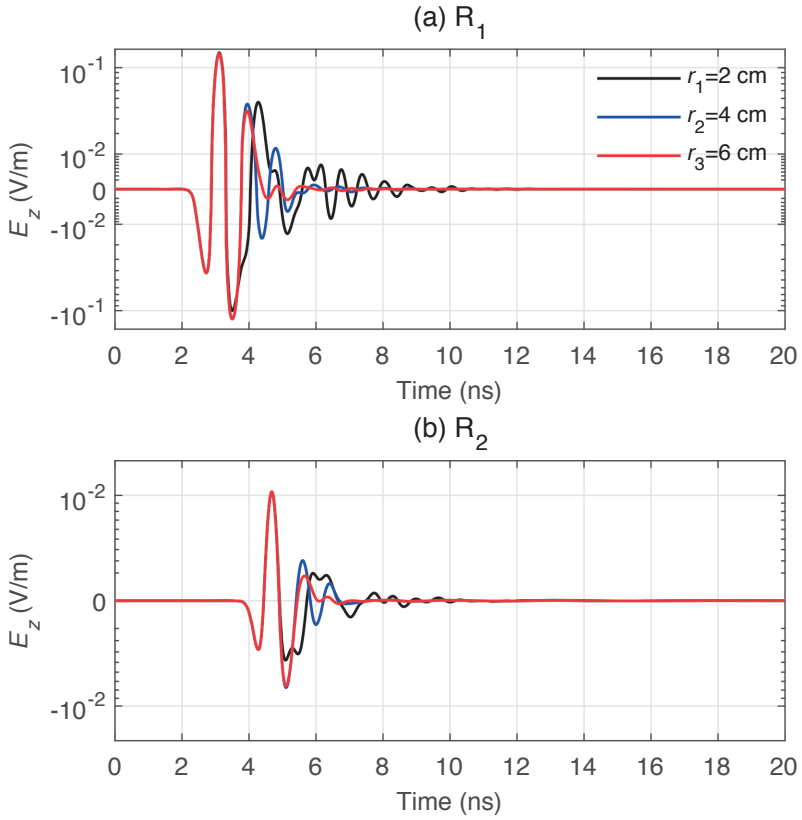

Figure 2.2: Waveforms by the first (a) and second (b) receiving antennas when the radial depths of the cavities are 2 cm (black curves), 4 cm (blue curves), and 6 cm (red curves), respectively. R_1 and R_2 denote the first and second receivers.

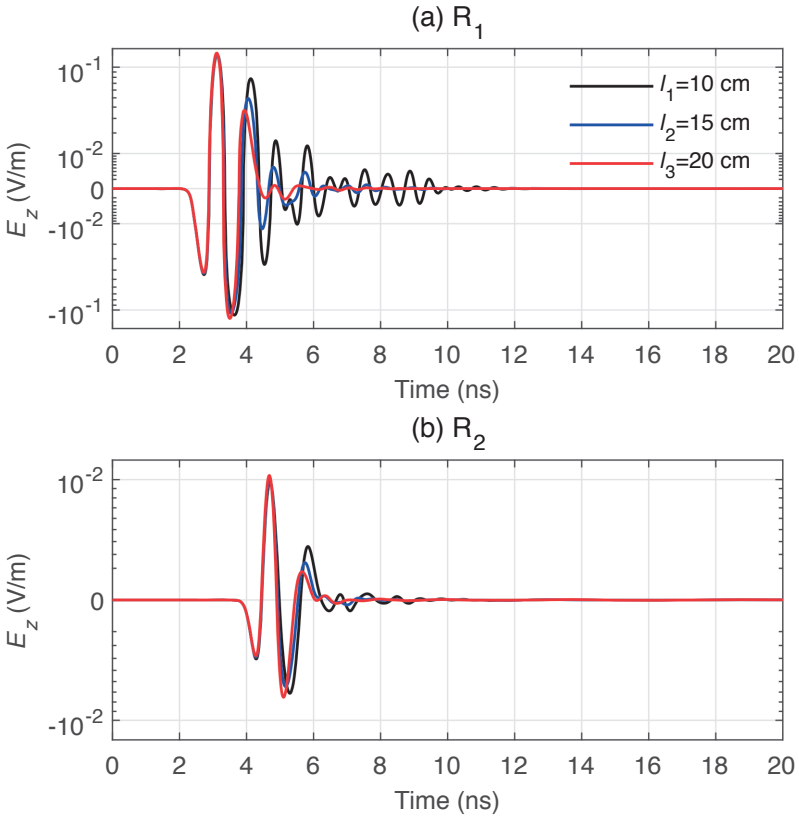

Figure 2.3: Waveforms by the first (a) and second (b) receiving antennas when the longitudinal length of the cavities are 10 cm (black curves), 15 cm (blue curves), and 20 cm (red curves), respectively.

2

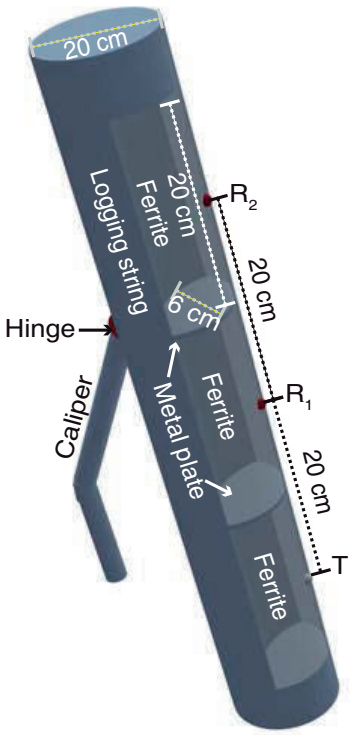

Figure 2.4: Structure and geometric parameters of borehole radar logging tool. T and R denote the transmitting and receiving antennas, respectively.

2.3. SURVEY METHOD

2.3.1. TIME-LAPSE LOGGING

Invasion front, the most prominently changed portion in the invaded formation, presents the greatest contrast of the electrical properties in the fluid distributions, and generates EM wave reflection events that are detectable by the borehole radar. A one-transmitter and two-receiver antenna configuration scheme is employed for time-to-depth conversion of radar signals, as illustrated in Figure 2.4. The surface-penetrating radar survey demonstrates that this measurement mode can determine the target depth effectively [3]. However, in the mud invasion case, the accurate derivation of the invasion depth is based on the correct extraction of the reflection signals from the invasion front, which are heavily influenced by the fluid distribution characteristics apart from the radar system per se. Working in a deep downhole, the borehole radar systems suffer much less from noise than the surface-penetrating radar, and the ringings are greatly alleviated as described above. Therefore, more attention is to be paid to the clutters arising from the radially uneven distributions of the flushed zone, as well as the heterogeneous rock. These factors will lower the signal quality and makes the straightforward signal extraction complicated or even impossible. A solution is to adopt a time-lapse logging to remove the majority of the clutters arising from the heterogeneity of the fluid and rock.

Figure 2.5 shows the radial distributions of fluid properties after the invasion of 72 and 96 hours, respectively. We can see that there is a remarkable conductivity contrast corresponding to the salinity front, which generates the EM reflection events. Over the invasion time, the conductivity contrast moves forward whereas the flushed zone has a slight change. Figure 2.6 shows the EM waves received by the two receiving antennas after 72 and 96 hours, and their time-lapse waveforms, respectively. For the raw logging signals (indicated as black and blue curves in Figure 2.6), we can see some trailings following the strong direct waves, which tend to be mixed with the weak reflected signals. After time-lapse subtraction operations, there are only two events remained explicitly. The earlier event is the time-lapse signals of the direct waves arising from the slight changes of the flushed zones at the two logging times, and the later event is the signals reflected from the invasion front at the first logging time (i.e., 72 hours in this case). The second event is the required signal for invasion depth solution, while the first event is irrelevant with invasion depth but needs to be separated from the second one. It can be seen that the time-lapse operations remove the majority of the undesired wave and extract a relatively clean reflected waves. Therefore, we propose to employ time-lapse manner to obtain high-quality reflected signals. The practical challenge is that an elaborated downhole tool design and acquisition strategy are required to maintain a high-precise relocation for the sequential logging operations [85]. This issue will be specially addressed in the future work.

2

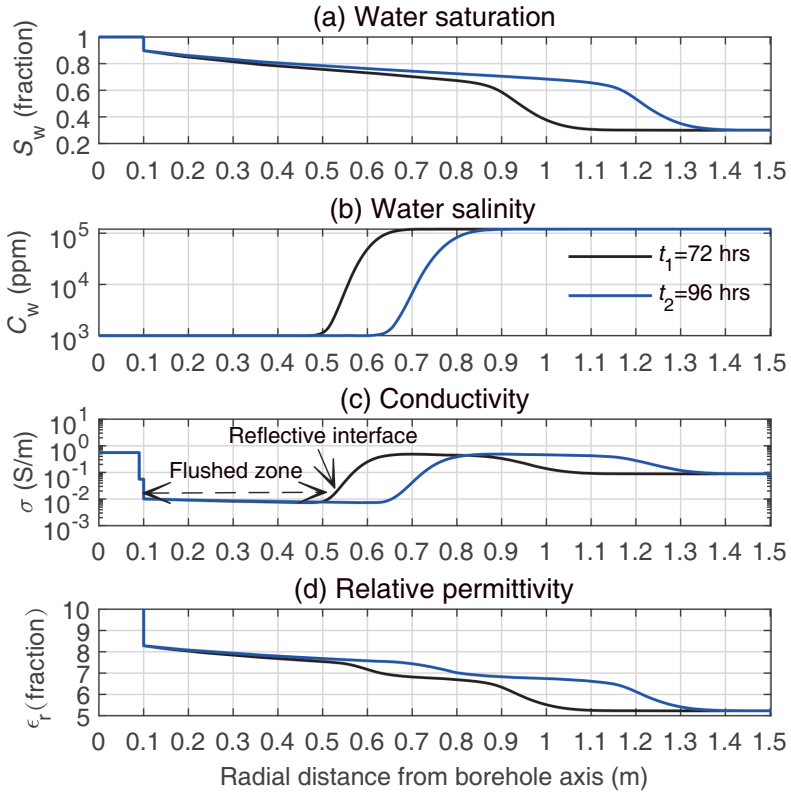

Figure 2.5: Radial distributions of fluid and electrical properties at the invasion of 72 (black curves) and 96 (blue curves) hours.

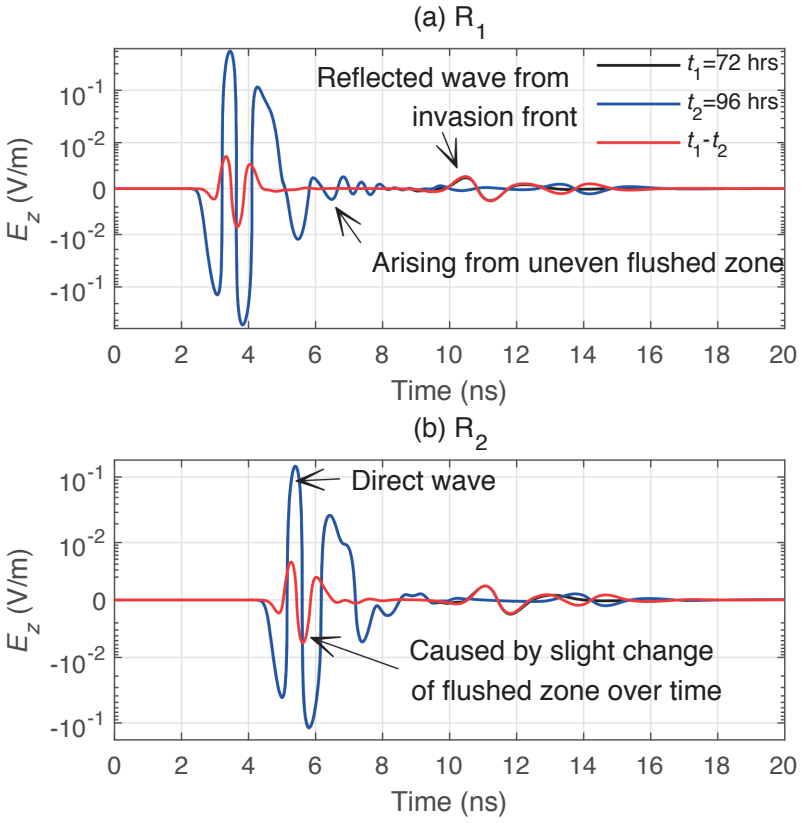

Figure 2.6: Received radar signals by the two receivers at the invasion of 72 (black curves) and 96 (blue curves) hours, and the corresponding time-lapse signals (red curves).

2.3.2. TIME INTERVAL OF TIME-LAPSE LOGGING

Time-lapse logging requires two sequential logging operations to extract the weak reflection signals by subtraction operations. It is worthy of investigating how the lag time between the two logging influences the time-lapse signal extraction. We assume that the first logging is conducted at the invasion of 72 hours, and the second logging occurs after 2 to 24 hours lagging behind the first one, respectively. Figures 2.7 and 2.8 show the radial distributions of fluid properties at different logging times and the corresponding time-lapse radar signals, respectively. By comparisons, we find out that when the logging time intervals are short (less than 4 hours), the time-lapse reflected signals have small amplitudes and shifted phases; whereas when the time intervals are large enough, the time-lapse signals present steady amplitude peaks and unified phases. This is because that only when there is a sufficient distance difference between the sequential invasion fronts can the time-lapse operations extract an intact reflected waveform from the two sets of radar data. We thus suggest that time-lapse logging should keep a certain time interval for proper signal extraction. In the practical field work, one should consider the relationship between the wavelength and the advancing speed of mud invasion in a certain formation to choose a proper logging time interval. A conservative valuation of the logging time interval is to adopt a long rather than a short one. In this chapter, we adopt 24 hours as the time interval in the following simulations.

2.3.3. DETECTION RANGE

As mentioned above, to successfully extract the reflected waves from the time-lapse signals, there must be a signal separation in time domain between the first and second EM events. This, therefore, imposes a limitation on the minimum detection depth because an excessively shallow invasion depth tends to bring about a time-domain waveform overlap of the direct and reflected waves. The investigation finds out that in the current scenario, when the invasion depth is shallower than 0.15 m (Figure 2.9), it is difficult to distinguish the reflected waves from the direct waves in the farther receiver, as shown in Figure 2.10b. If, in any case, a shallow invasion needs to be solved, an alternative solution is to configure a monostatic antenna in the transmitter to receive a separable signal, as indicated in Figure 2.10c. However, this configuration increases the cost and complexity of the downhole systems.

Generally, the interested investigation range of mud invasion is within 1 m. To check the detection capability of weak signals, a key indicator of a GPR system is dynamic range, which reflects the logarithmic ratio of the maximum receivable and minimum detectable signal amplitudes [3]. We simulate the time-lapse signals reflected from the invasion front of 1 m away from the borehole wall, as indicated in Figures 2.11 and 2.12. Assuming that maximum recordable signal (i.e., saturated voltage) is 1 V/m, to obtain the weak reflected signals shown in Figure 2.12, a dynamic range of 96 dB is required. The technology is currently available by using a 16-bit A/D sampling chip [86]. We suggest that the borehole radar with the currently available configuration has the detection capability from 0.15 to 1 m.

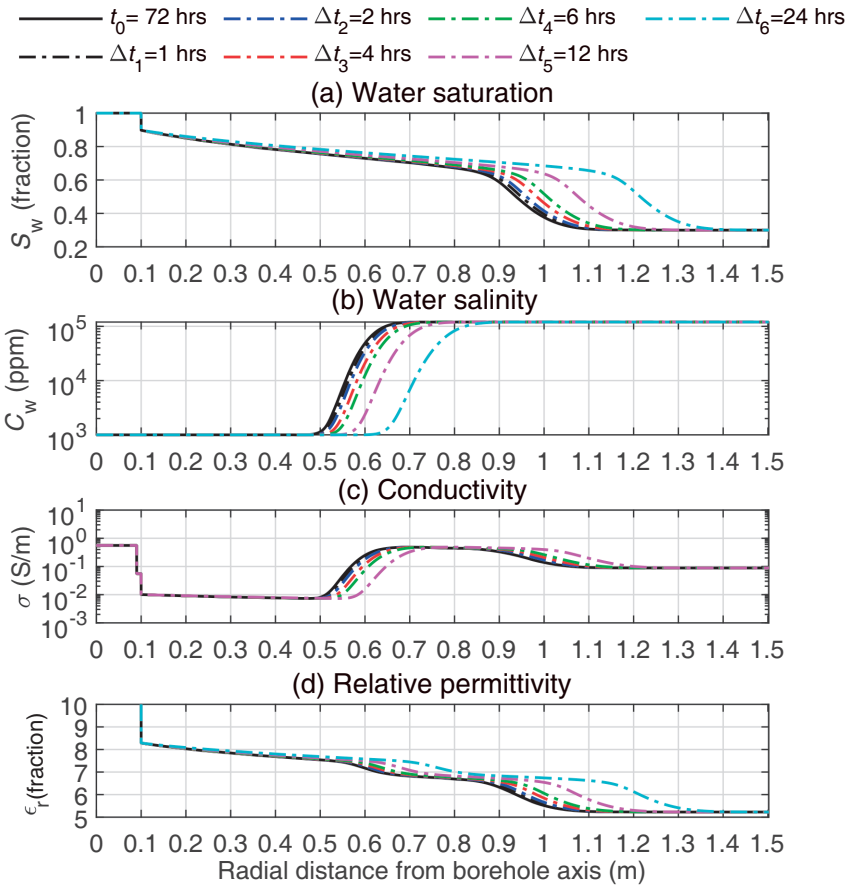

Figure 2.7: Radial distributions of fluid and electrical properties at varying time-lapse logging times. The black solid curve stands for the first logging time after the invasion of 72 hours, and the dash curves denote the times of 1, 2, 4, 6, 12, and 24 hours lagging behind the first logging time, respectively. t_0 denotes the first logging time, and Δt denotes the time lag.

2

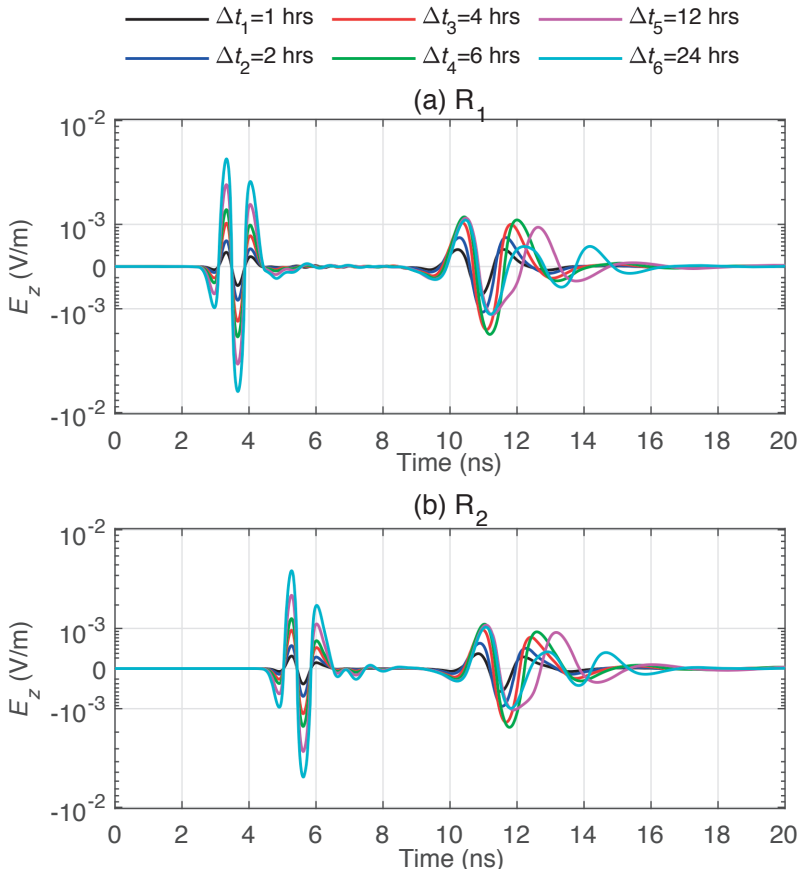

Figure 2.8: Time-lapse radar signals in two receivers for the varying logging lag times, corresponding to the fluid distributions in Figure 2.7. Δt denotes the time lagging behind the first logging.

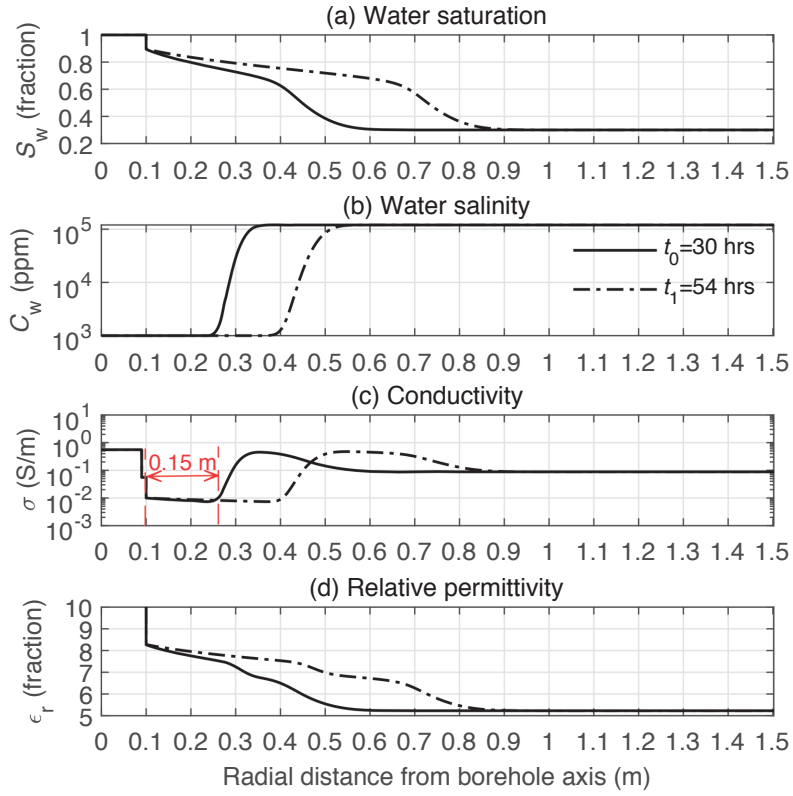

Figure 2.9: The distributions of fluid and electrical properties after the invasion of 30 and 54 hours. The red dash line shows the shortest detection range of the invasion depth.

2

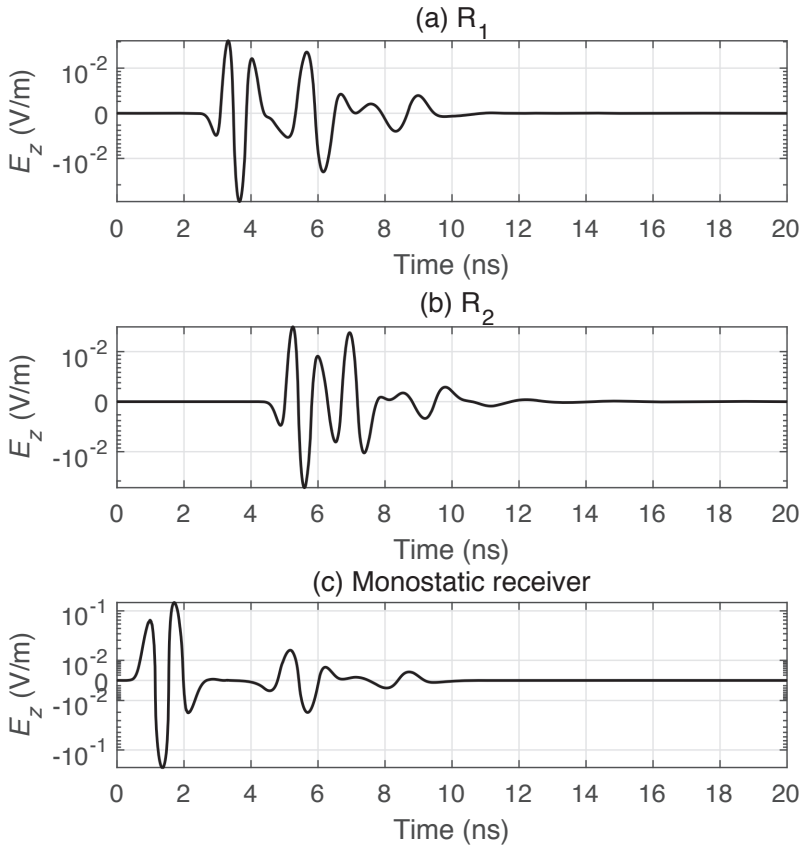

Figure 2.10: Time-lapse radar signals obtained by R_1 (a), R_2(b), and the monostatic (zero offset) antennas configuration (c), corresponding to the fluid distributions in Figure 2.9.

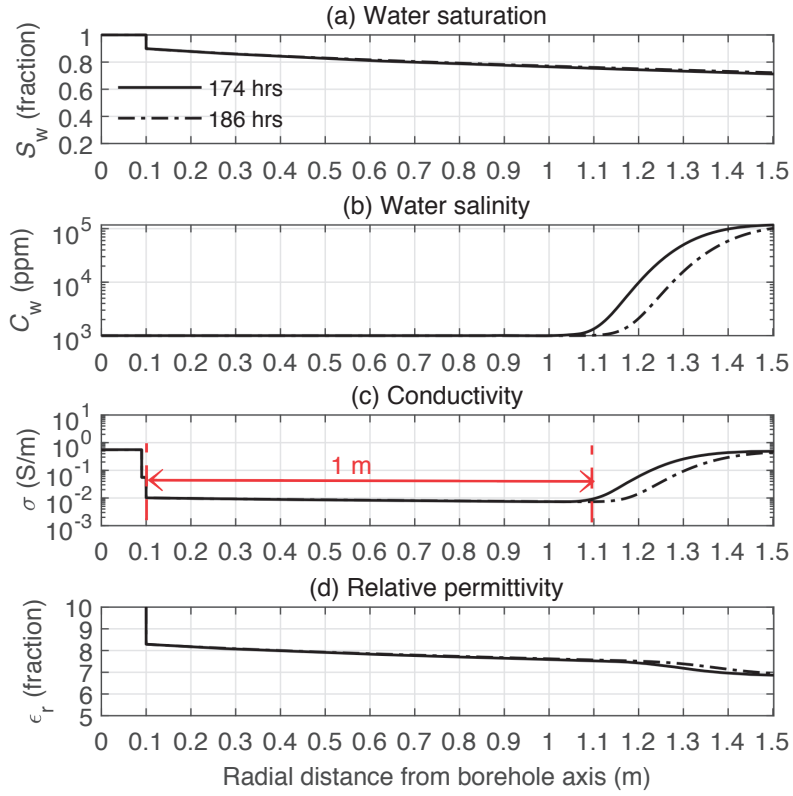

Figure 2.11: The distributions of fluid and electrical properties at the invasion times of 174 and 186 hours. The red line shows the distance of the invasion front from the borehole wall.

2

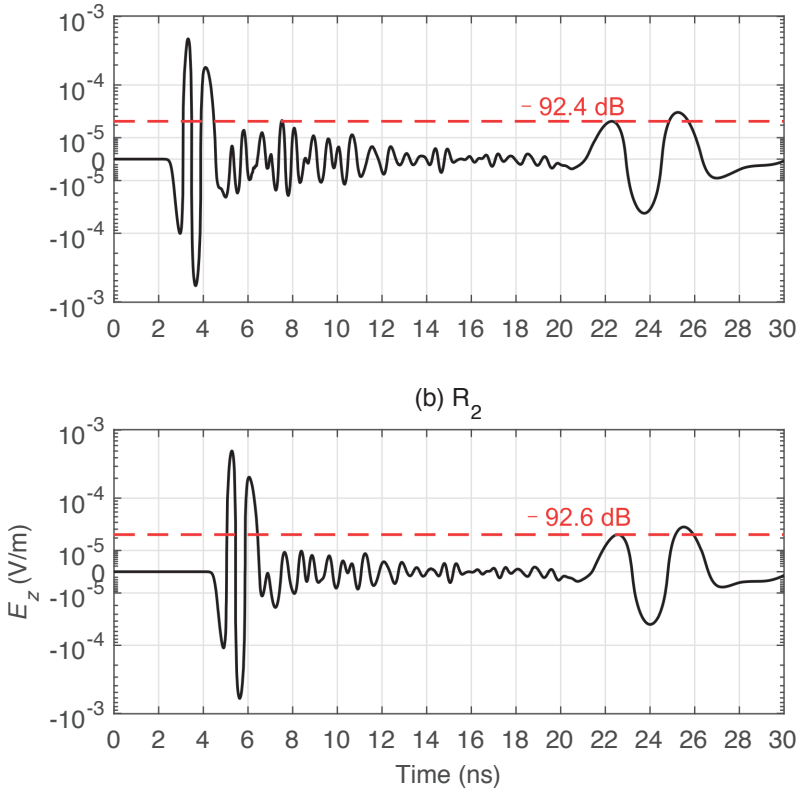

Figure 2.12: Time-lapse radar signals obtained by R_1 (a) and R_2 (b), corresponding to the fluid distributions in Figure 2.11. The red dash lines show the logarithmic expression of the amplitude relative with the maximum receivable amplitude of 1 V/m, implying the required dynamic range for picking up the reflected signals.

2.4. SENSITIVITY ANALYSES

The reservoir scenario described above is taken as a base case for sensitivity analysis study, with which time-lapse borehole radar logging is simulated for mud invasion detection. The first logging is operated when the invasion front penetrates a depth of 0.4 m from the borehole wall, and the second logging happens at 24 hours later than the first. A sequence of simulations are run by exerting independent perturbations on the primary petrophysical properties, including oil viscosity, relative permeability, capillary pressure, porosity, initial water saturation, mud salinity, formation water salinity, and diffusion coefficient. We analyse their respective effects on the distributions of fluid and electrical properties as well as the resulting time-lapse borehole radar signals. The results show that oil viscosity, porosity, mud salinity, formation water salinity and diffusion coefficient have major effects on the time-lapse signal quality, because they are sensitive to either the magnitude contrast or the shape of the electrical properties. The rest of the petrophysical properties, e.g., initial water saturation, relative permeability and capillary pressure, have slight influences on the electrical property contrast in spite of they impose great effects on the saturation profile. Therefore, they have minor influences on the extraction of the reflection radar signals and can be neglected. We present the major properties that influence the EM signals extraction and analyse the mechanism.

2.4.1. EFFECTS OF VISCOSITY

Viscosity provides a measure of a fluid's internal resistance to flow. For various reservoir types, oil viscosity has a dramatically varying range from an order of one tenth up to millions of times of water viscosity [87]. We increase the oil viscosity from 3.55 cp to 35.5 cp and 355 cp, respectively, simulating a light, viscous, and heavy oil reservoir type. The fluid property distributions and time-lapse EM responses are shown in Figures 2.13 and 2.14. We see that the light oil reservoir (base case) presents a quasi piston-like invasion profile and results in considerable reflected waves. Conversely, the viscous and heavy oil reservoirs present dragged invasion zone and give rise to gradually weak but still detectable reflected waveforms. The results imply that the proposed method has a wide applications to various reservoir types, but it is subject to more challenges in heavy oil reservoirs than light oil reservoirs.

2.4.2. EFFECTS OF POROSITY

Porosity has demonstrated a negative correlation with the invasion depth [50]. Besides, it exerts significant influences on the electrical properties of the invaded formation according to equations A.10 and A.12. We run simulations by increasing the formation porosity from 0.15 to 0.25 and 0.35, respectively, representing three types of reservoir characterized with different qualities [48]. A dramatic rise is observed in the bulk conductivity and bulk relative permittivity, as shown in Figure 2.15. Accordingly, from Figure 2.16, we see an obvious amplitude decline and phase delay of the reflected waves in the time-lapse EM signals, which are caused by the increased material loss and decreased wave velocity in the flushed zone. It implies that a lower-porosity reservoir is

2

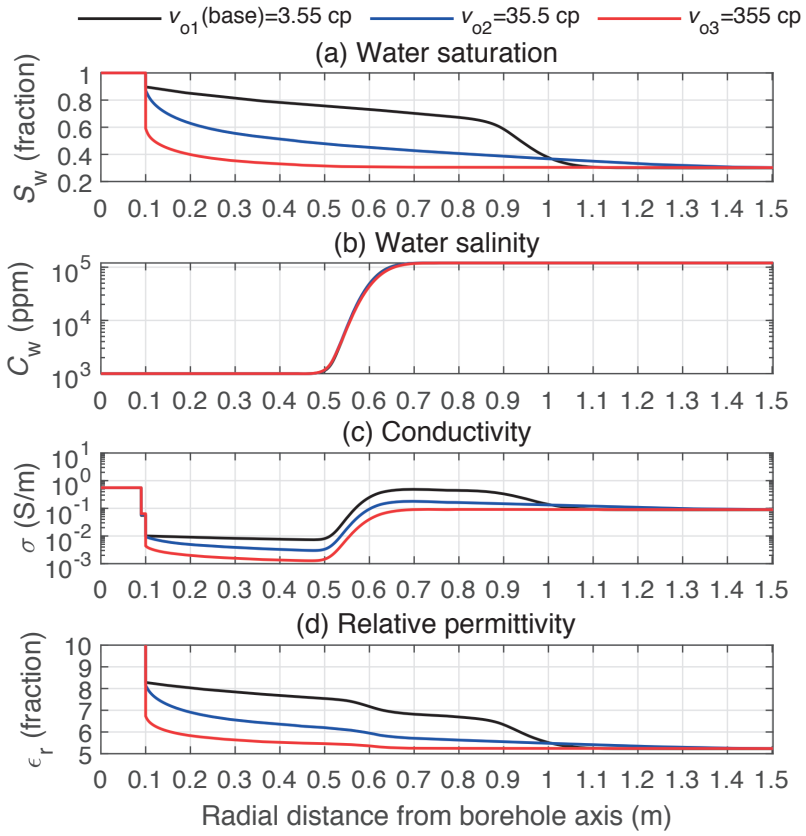

Figure 2.13: Fluid and electrical property distributions when the mud invades the formation 0.4 m far from the borehole wall for the oil viscosities of 3.55 cp, 35.5 cp, and 355 cp, respectively.

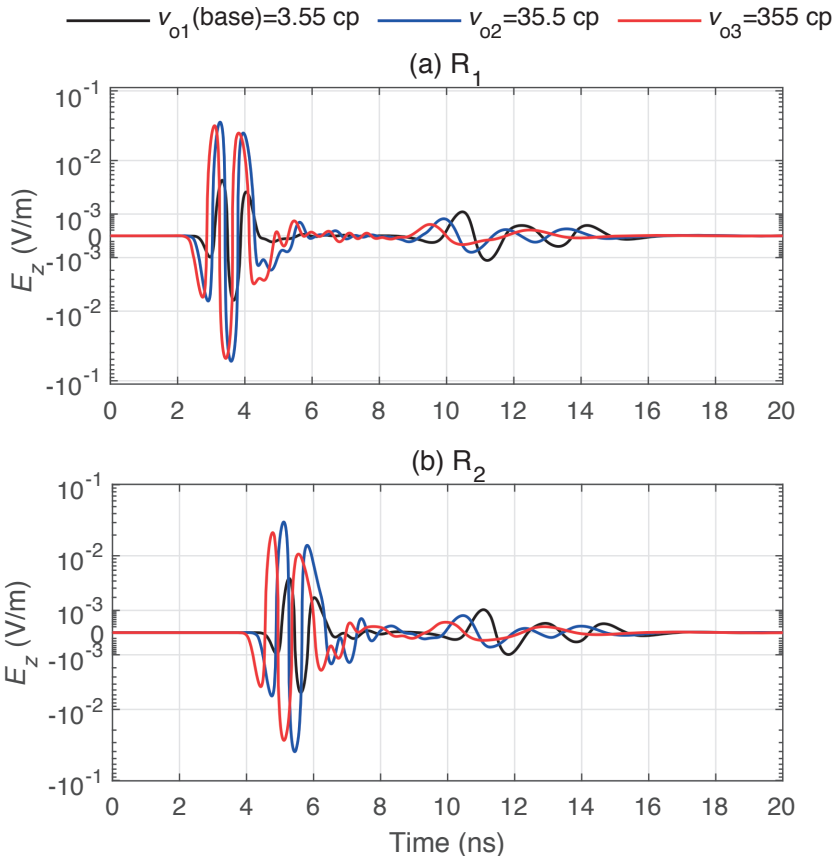

Figure 2.14: Time-lapse radar signals received by R_1 (a) and R_2 (b) corresponding to the simulated fluid distributions for the oil viscosities of 3.55 cp, 35.5 cp, and 355 cp.

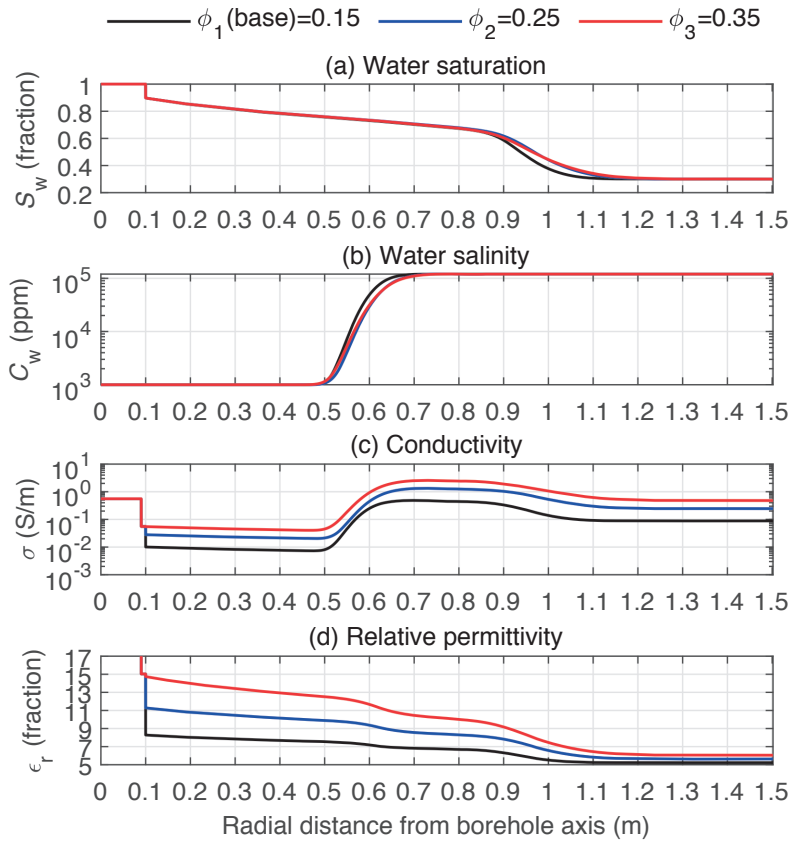

Figure 2.15: Fluid and electrical property distributions when the mud invades the formation 0.4 m far from the borehole wall for the porosity of 0.15, 0.25, and 0.35, respectively.

more beneficial for mud refection signal extraction than a higher one. The conclusion suggests that borehole radar is applied better to low-porosity reservoir.

2.4.3. EFFECTS OF MUD SALINITY

The water salinity in the water-base mud filtrate has a significant effect on the quality of the radar data. Though the logging calliper forces the antennas tightly attached to the borehole wall to decrease the EM attenuation arising from the conductive mud in the borehole (Figure 2.4), the mud filtrate still exerts great influences on the bulk conductivity of the invaded zone. We increase the mud salinity from 1^3 ppm to 5×10^3 ppm and 10×10^3 ppm, varying from fresh water-based mud to the saline water-based mud [47]. We observe a dramatically rising bulk conductivity in the flushed zone, as shown in Figure 2.17. The reflected signals in the time-lapse data decrease until invisible with the increase of the mud salinity (Figure 2.18). There are two reasons to explain the

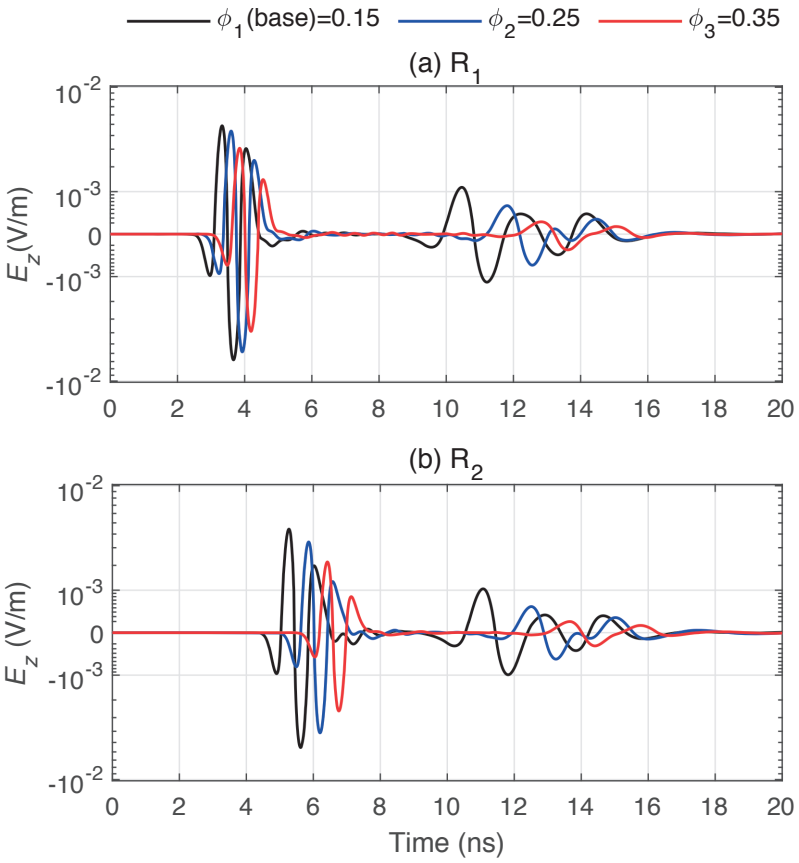

Figure 2.16: Time-lapse radar signals received by R_1 (a) and R_2 (b) corresponding to the simulated fluid distributions for the porosity of 0.15, 0.25, and 0.35, respectively.

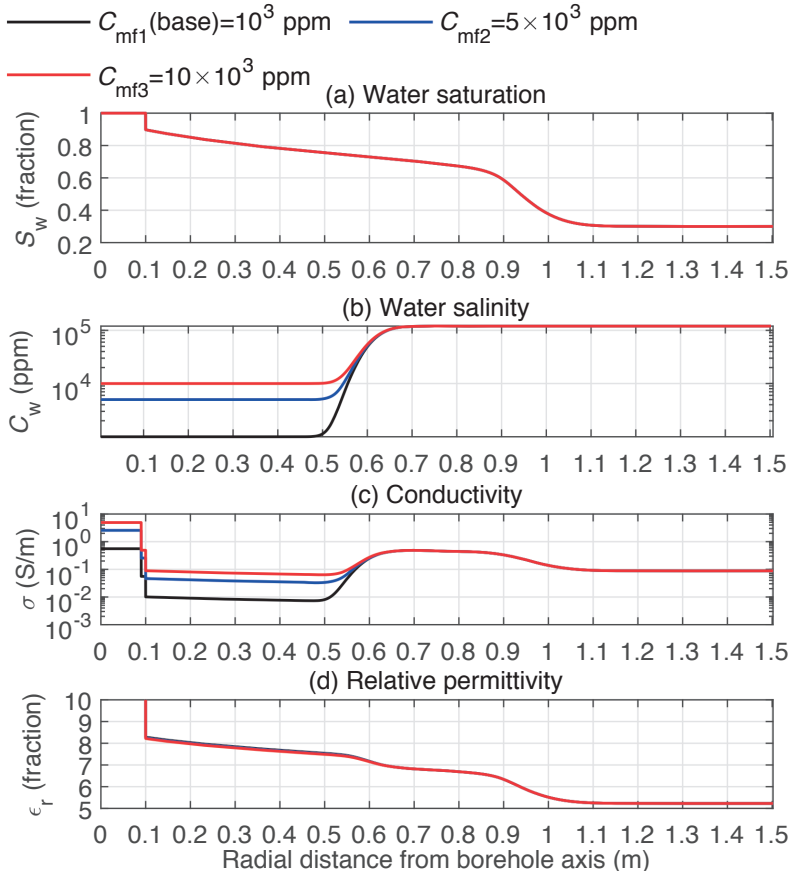

Figure 2.17: Fluid and electrical property distributions when the mud invades the formation 0.4 m far from the borehole wall for the mud salinity of 10^3 ppm, 5×10^3 ppm, and 10×10^3 ppm, respectively.

deteriorated reflected signals: (1) the rising the EM attenuation in the flushed zone, and (2) the declined the EM property contrast in the low-resistivity annual boundary. We recommend that the borehole radar method is applied in a water-base mud with low salinity.

2.4.4. EFFECTS OF FORMATION WATER SALINITY

Under the action of the convection and diffusion, the invaded salt ions displace the in-situ salt ions when the mud filtrate flows into the formation. Therefore, the bulk conductivity of the formation is altered, and a conductivity contrast is formed, which is critical to generate radar wave reflections. We decrease the initial formation water salinity from 12×10^4 ppm to 5×10^4 ppm and 1.2×10^4 ppm, and obtain the distributions of the fluid and electrical properties and the corresponding time-lapse radar responses, as shown in Figures 2.19 and 2.20, respectively. We see that, as the decrease of the initial

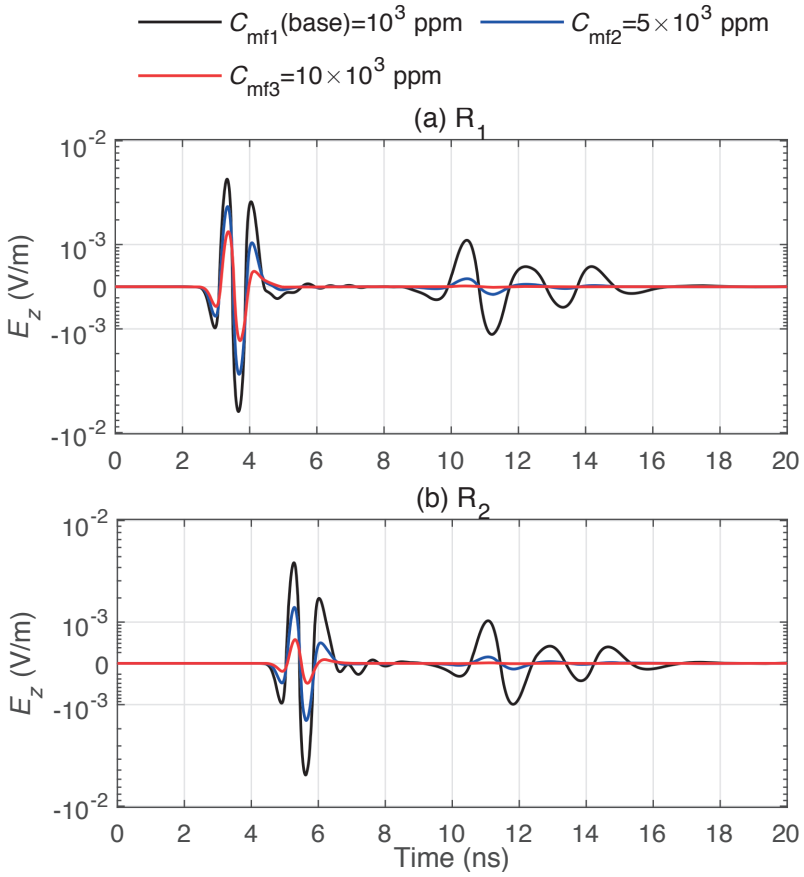

Figure 2.18: Time-lapse radar signals received by R_1 (a) and R_2 (b) corresponding to the simulated fluid distributions for the mud salinity of 10^3 ppm, 5×10^3 ppm, and 10×10^3 ppm, respectively.

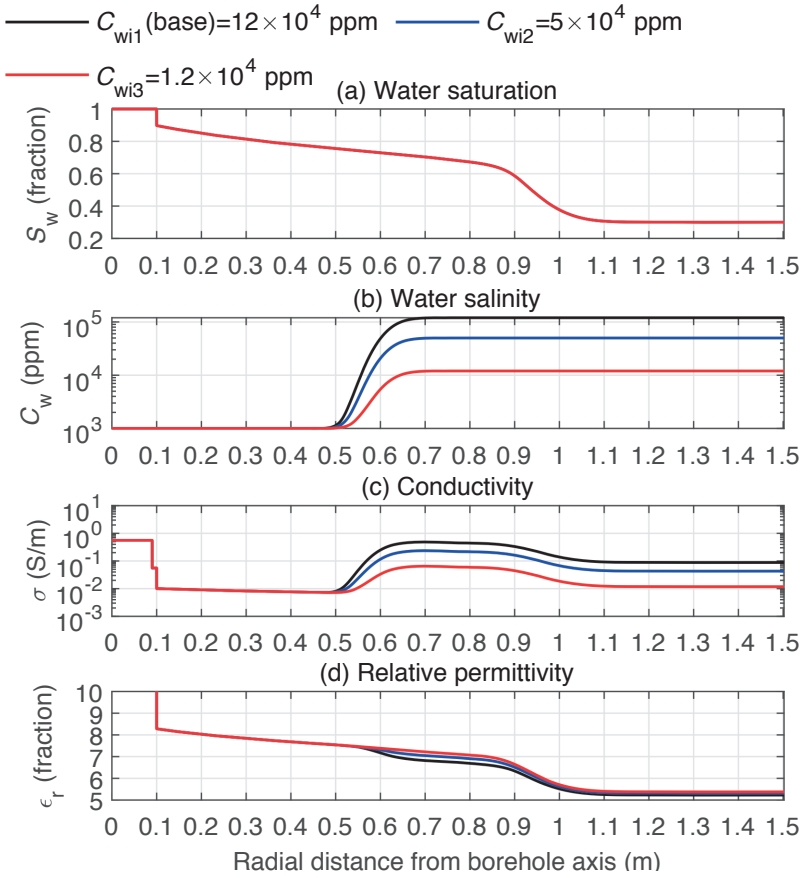

Figure 2.19: Fluid and electrical property distributions when the mud invades the formation 0.4 m far from the borehole wall for the initial formation water salinity of 12×10^4 ppm, 5×10^4 ppm, and 1.2×10^4 ppm, respectively.

formation water salinity, the conductivity contrast decreases, causing a dramatic drop in the magnitude of the reflection signals. The results imply that a high-salinity reservoir is more beneficial for the proposed method than a low-salinity reservoir.

2.4.5. EFFECTS OF DIFFUSION COEFFICIENT

The salt miscibility occurs under salt concentration difference existing in the invaded mud filtrate and the in-situ formation water. Apart from the convective transport of salts with the fluid flowing, the diffusion effects play an important role in the mixing of salt ions, as formulated by equations A.8 and A.9. Ionic diffusion coefficient is a key indicator for diffusion effects, and its magnitude heavily depends on the temperature apart from the texture of the solutes [88]. We increase the diffusion coefficient of the salt ions from 6.45×10^{-9} m^2/s, to 1.94×10^{-8} m^2/s and 3.23×10^{-8} m^2/s, which are the

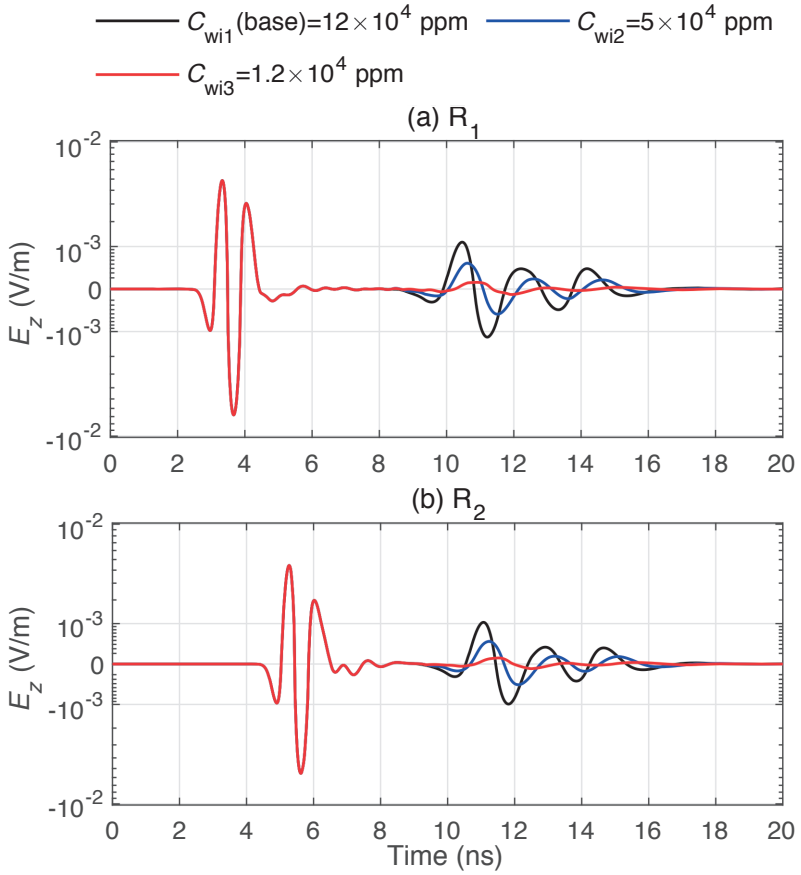

Figure 2.20: Time-lapse radar signals received by R_1 (a) and R_2 (b) corresponding to the simulated fluid distributions for the initial formation water salinity of 12×10^4 ppm, 5×10^4 ppm, and 1.2×10^4 ppm, respectively.

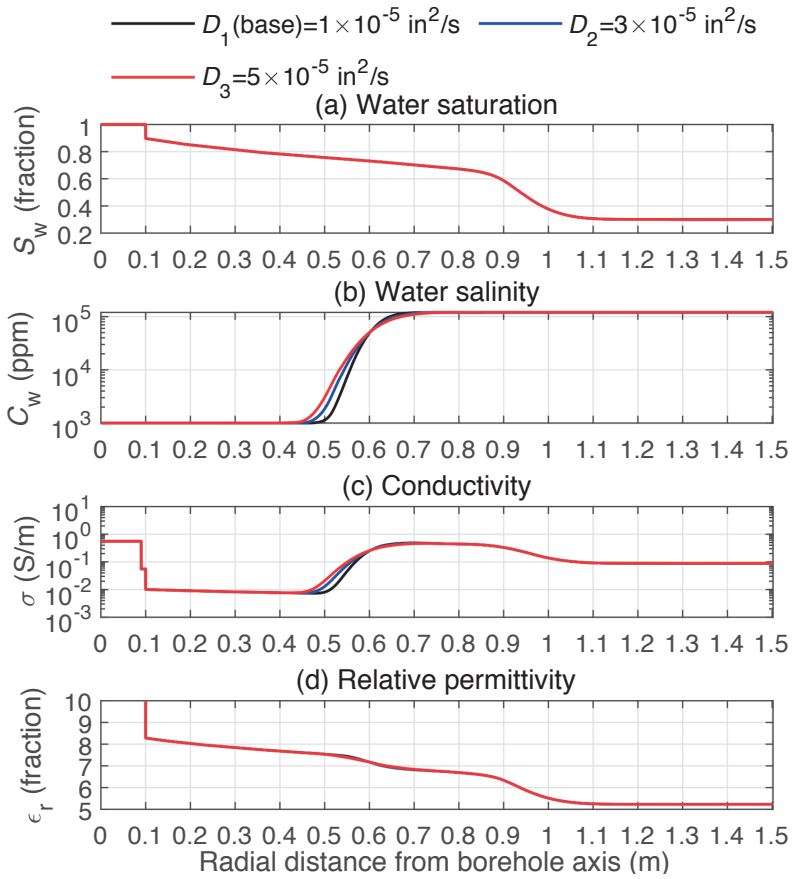

Figure 2.21: Fluid and electrical property distributions when the mud invades the formation 0.4 m far from the borehole wall for the salt diffusion coefficient of 1×10^{-5} in^2/s (6.45×10^{-9} m^2/s), 3×10^{-5} in^2/s (1.94×10^{-8} m^2/s), and 5×10^{-5} in^2/s (3.23×10^{-8} m^2/s), respectively.

reasonable range in a deep reservoir environment [45]. The simulated distributions of fluid and electrical properties indicate that the increased diffusion coefficient lengthens the transition zones of the water salinity and thus the bulk conductivity, as shown in Figure 2.21. The smoother transition front creates a weaker reflected waves, as shown in Figure 2.22. We suggest that the salt diffusion coefficient should be paid attention to when the method is utilized.

2.5. CONCLUSIONS

In this chapter, we carry out numerical simulations with a coupled mud invasion and borehole radar modelling to analyse the influences of the logging scheme and the fluid and rock properties on the extraction of the mud front reflection signals. From the simulations results, we recommend that: (1) in the employed radar frequency and

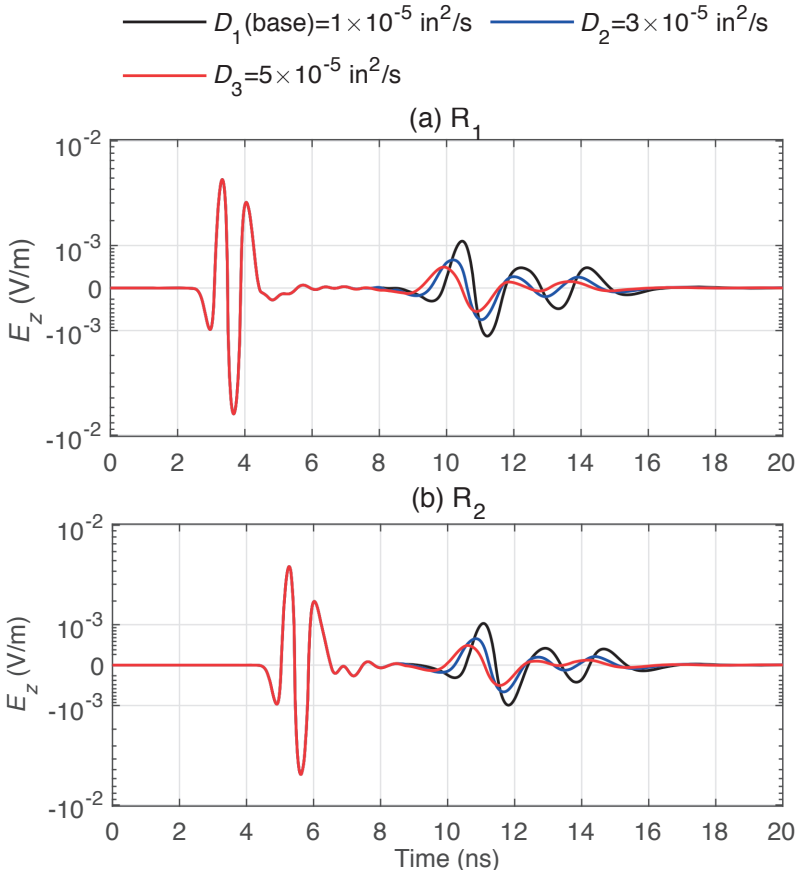

Figure 2.22: Time-lapse radar signals received by R_1 (a) and R_2 (b) corresponding to the simulated fluid distributions for the salt diffusion coefficient of 1×10^{-5} in^2/s (6.45×10^{-9} m^2/s), 3×10^{-5} in^2/s (1.94×10^{-8} m^2/s), and 5×10^{-5} in^2/s (3.23×10^{-8} m^2/s), respectively.

bandwidth, the antennas cavity inside the logging string should be made at a depth of 6 cm and a length of 20 cm at least to diminish the ringing effects and acquire high-quality signals; (2) the proposed time-lapse logging scheme is able to remove the majority of EM clutter from the non-uniform flushed zone and inhomogeneous rock, obtaining relatively clean signals; (3) the time interval of the sequential loggings should be larger than 6 hours to obtain an intact reflected waveform; (4) under the current borehole configurations and reservoir scenario, the detection range is from 0.15 to 1 m; (5) the reflected signals from the mud invasion front are sensitive to the oil viscosity, porosity, mud and formation water salinity, and salt diffusion coefficient, which should be paid much attention to before the method is applied to a certain reservoir. The results in this chapter suggest that borehole radar can be applied in a deep oil well as a novel logging method, and one of its applicabilities is to detect the mud invasion depth. However, reservoir and fluid types should be carefully analysed before conducting the logging operations in any particular oil field.

3

ESTIMATING RESERVOIR PERMEABILITY WITH BOREHOLE RADAR

SUMMARY

In oil drilling, mud filtrate penetrates into porous formations and alters the compositions of the pore fluids. This disturbs the logging signals and brings errors to reservoir evaluation. Logging engineers therefore deem mud invasion undesired, and attempt to eliminate its adverse effects. However, the mud-contaminated formation carries valuable information, notably about its hydraulic properties. Typically, the invasion depth critically depends on the formation porosity and permeability. Therefore, if adequately characterized, mud invasion effects could be utilized for reservoir evaluation. Borehole radar has the desired resolution and depth range and can be developed for this purpose. By coupling fluid flow and radar reflection experiments, it is found that estimating invasion depth and permeability is feasible. Time-lapse radar measurements are used to determine invasion depth. Drilling, coring and logging data are required to establish a quantitative interpretation chart to convert invasion depth to permeability. The numerical tests show that the method provides permeability estimates in a good agreement with the actual formation permeability. This method has potential for determining permeability estimates from the mud invasion effects.

The content of this chapter is based on the following paper:

F. Zhou, I. Giannakis, A. Giannopoulos, K. Holliger, and E. Slob, Estimating reservoir permeability with borehole radar, *Geophysics*, vol. 85, no. 4, pp. H51–H60, 2020.

3.1. INTRODUCTION

Porosity, permeability, and water saturation are essential petrophysical properties in hydrocarbon reservoir evaluation. Water saturation and porosity can be reliably inferred by conventional well logging data, whereas permeability information is notoriously difficult to be directly estimated downhole [89]. Permeability has complex relations with other petrophysical properties and is generally associated with grain size, pore size, specific surface area, pore throat size, and porosity connectivity [90]. Core analysis is deemed the most direct and reliable way to determine permeability. However, it is costly and is therefore generally limited to a few stratigraphic locations [91]. In addition to uncertainties and/or biases in sampling, core samples are measured in a laboratory environment, which is not guaranteed to be equivalent with the in-situ [92]. Furthermore, core measurements are carried out at a scale that is not representative of the fluid flow in a representative elementary volume (REV) of the reservoir [93].

Some empirical models have been established to estimate permeability from porosity through statistical correlations, typically based on the Kozeny-Carman equation [94–98]. The validity of these methods is based on the premise of a close correlation between permeability and porosity. However, for some pertinent reservoir types, for example, those with low porosity and low permeability, it is generally acknowledged that the correlation between the porosity and permeability tends to be poor to non-existent. The reason for this is that the geometry and the specific surface area of the pores have more significant effects on the permeability than the pore size itself does [92]. Field-based core analysis shows that, in low-porosity reservoirs, the permeability may fluctuate by orders of magnitude even if the porosity is quasi-constant [99]. Moreover, in consolidated sandstone, fractured, and karstic reservoirs, there are rarely consistent correlations between the porosity and permeability [100]. Similarly, permeability estimation based on the analysis of Stonely waves and Nuclear Magnetic Resonance (NMR) logging is generally invalid in low-porosity reservoirs [101,102].

In the course of drilling, mud filtrate penetrates into the porous formation, and alters the compositions of the pore fluids. This brings about disturbances in well logging signals and affects the accurate evaluation of reservoir properties. Logging engineers try to eliminate mud invasion effects and to accordingly correct the logging data. Nevertheless, the mud-contaminated parts of the formation could contain valuable information. A parametric sensitivity analysis revealed that for a given formation interval, the invasion depth has strong correlations with the permeability and porosity [50]. This inspires us to find a new approach to estimate the hydraulic properties of a reservoir based on the mud invasion effects. The feasibility of this approach relies on two principal considerations: (1) mud invasion effects, especially the invasion depth, can be characterized adequately by well logging; and (2) a quantitative relationship should be established to link the invasion effects with the formation properties. A few numerical and field trials have attempted to estimate the reservoir permeability by inverting the radial electrical resistivity profiles, inferred from array induction logging, of an invaded reservoir [47,78,81]. The estimated results provided consistent order-of-magnitude-type with the coring permeability, but the errors are considerable. This is because array

induction logging has a too low radial spatial resolution to precisely solve the invasion depth. Conventional logging methods, whether electrical or acoustic, have no capability of finely describing the complicated invasion status due to their limited resolution and/or sensitivity. To alleviate this problem, the use of high-frequency borehole radar for detecting mud invasion depth is investigated in this paper. Once the invasion depth is accurately identified by borehole radar measurements, we can then correlate it with the reservoir permeability.

Borehole radar has been widely applied in shallow subsurface mining, cavity imaging, fracture characterization, and hydrogeophysical exploration [20,22,103–105]. Chen *et al.* firstly proposed to apply borehole radar to well logging [38]. A borehole radar logging prototype has been developed with the original intention to image fractures in hydrocarbon reservoirs [106–108]. Their borehole radar systems operate at frequencies of few hundred megahertz, which correspond to wavelengths ranging from several decimeters to 1 meter and penetrating depth of a few meters for regular reservoir types. Oloumi *et al.* conducted laboratory experiments to investigate the feasibility of characterizing the oil well perforation and corrosion with the near-field responses of a high-frequency (up to 6 GHz) radar antenna [42,109]. A so-called "dielectric logging" tool and its serial products have been introduced into the well logging, which consist of multi-spacing and multi-frequency (from 20 MHz to 1 GHz) coils to characterize the near-borehole region [84]. However, the narrow-band signals and short offsets limit the accuracy and integrity of the acquired information. For the mud invasion detection purposes, a penetrating depth of tens of centimeters and radial resolution of a few centimeters are required. Heigl *et al.* simulated high-frequency radar wave propagation and reflection in oil- and water-based mud invasion cases [39]. They suggested that a directional borehole wide-band radar with a center frequency of 1 GHz is able to detect observable signals reflected from mud invasion front, even under the relatively conservative limitations on radar system performance. Although they used a simplified geological model in their preliminary study, we believe that their suggested radar frequency is applicable for realistic reservoir environments.

To our knowledge, such radar logging tools do not exist for the purpose of mud invasion detection. In this chapter, we present a numerical study that investigates the feasibility of detecting mud invasion and estimating permeability using borehole radar. The proposed method couples a hydraulic model with a solution of the electromagnetic equations in an effort to realistically replicate the radar responses on a mud-disturbed reservoir. We simulate a scenario of freshwater mud invading a low-permeability oil reservoir with open-hole radar logging to explore the feasibility of the proposed method.

3.2. NUMERICAL MODELLING

3.2.1. MUD INVASION MODELLING AND RESERVOIR SCENARIO

Mud invasion is a complicated flow and transport process, specific to drilling mud types and reservoir conditions. Generally, logging engineers divide the invaded formation

into the flushed, transition, and virgin (or undisturbed) zones according to how much mobile in-situ fluids are displaced by mud filtrate [48]. To acquire detectable radar reflections from the invasion front, several key factors should be considered. First, the flushed zone should have a relatively low conductivity to ensure low attenuation and low phase distortion for radar wave propagation. Second, there must be an adequate contrast of electrical properties between the flushed and virgin zones, and the transition zone should be thin and exhibit a steep gradient relative to the dominant wavelength, such that sufficiently strong radar reflection events are generated.

Drilling mud types are usually categorized into freshwater mud, saltwater mud and oil-based mud [110]. Salt water mud brings about a highly conductive flushed zone, which would compromise the performance of borehole radar by severely reducing its penetration depth. Oil-based mud is favorable for radar wave propagation because of the associated low conductivity of the invaded zones. It does, however, tend to create a gradual oil-water transition zone primarily due to the non-wettability and the low flow coefficient of the oleic phase [48]. The resulting gradual transition zone is unfavorable for generating radar wave reflections in our borehole radar applications. Besides, oil-based mud is not as popular as water-based mud due to its high costs and environmental unfriendliness [110]. Therefore, we prefer to consider freshwater mud for the purpose of this study.

Reservoirs frequently consist of one sand body sandwiched between gas- and brine-saturated sections [111]. In a completely water-saturated layer, the invaded water-based mud filtrate is miscible with the in-situ aqueous phase and, hence, it is difficult to explicitly define an invasion boundary. Therefore, we restrict the current investigations to an oil-bearing layer because of the immiscibility of aqueous and oleic phases. A heavy oil reservoir is not recommended for the proposed borehole radar applications due to the fact that the high viscosity of the oleic phase creates a gradual and long transition zone, which is not favorable for radar wave propagation and reflection [112]. For these considerations, the current investigation is carried out in a scenario of freshwater mud invading a light-oil layer.

The physical process of mud invasion is usually described as a multiphase and multicomponent flow problem [113]. We adopt the two-phase (water and oil) isothermal Darcy flow equations and convection-diffusion equation to solve for the pressure, water saturation, and water salinity in the near-borehole region over invasion time [114–116]. The complete equations and formulas can be found in Appendixes A.1. The equation sets are discretized in a cylindrical coordinate system, and pressure, saturation, and salinity are sequentially solved for with the implicit, explicit, and implicit treatments, respectively. We understand that the characteristics of the shape of fluid distribution are critical to investigate the radar wave propagation, transmission, and reflection. Therefore, our model incorporates as many parameters as possible, such as capillary pressure, rock and fluid compressibility, and ionic diffusion effect, in order to simulate realistic fluid transition profiles. Localized grid refinement is employed in the near-borehole region.

The drilling mud generally contains solid particles to sustain a slightly high downhole pressure with respect to the reservoir. In the course of the mud invasion, the solid particles gradually deposit on the borehole wall and build up a so-called mud cake [43]. The temporal evolution of mud cake thickness, permeability, and porosity depends on the pressure drop across the mud cake in addition to the textures of the mud itself. Correspondingly, the time-varying mud cake properties influence the inflow rate and, thus, the invasion depth at a given time. Essentially, the flow coefficients of fluids in the mud cake and the formation tend to control the invasion rate under a certain pressure difference [48]. To emulate this process, a set of mud cake growth formulas (see Appendix A.3), which was derived based on laboratory experiments [43], are coupled with the above flow model. We developed a 2D MATLAB®[1] program for the mud invasion simulations, which has shown to agree well with the published results [48,81].

We simulate a scenario of fresh water mud invading a light oil layer. The governing parameters and material properties are listed in Table 3.1. The considered porosity, permeability, and water saturation curves, which vary with depth, are synthesized based on core data from a well in the Honghe Oilfield, Ordos Basin, China. The results shown in Figure 3.1 are obtained after applying a five-point moving average filter to reduce erratic noise. This oil field is a typical tight oil sandstone reservoir, which presents an ideal test scenario for our study: first, the considered reservoir section is characterized by low porosity and low permeability, which means that the permeability can not be accurately estimated through the correlations with porosity; second, the selected layer contains a high percentage of oil, which would form a distinct oil-water front in the course of the invasion process.

3.2.2. BOREHOLE RADAR CONFIGURATION AND MODELLING

Compared with surface ground-penetrating radar measurements, borehole radar logging works in a complex environment, which, in turn, imposes constraints on the antenna configurations [1]. To carry out the downhole measurements, the radar antennas are mounted in an arc-shaped cavity of the logging string. To decrease the interference arising from the metal components and increase the radar directionality, a certain special material is filled in the cavity. There are two optional schemes for the filling material. One is to choose a material with high dielectric permittivity, thus, shortening the wavelength of the backscattered waves to decrease the destructive interference [41]; the other is to use a type of absorbing material to attenuate the backscattered waves [107]. We adopt the latter scheme by filling absorbing material into the cavity. The filling material should have certain dielectric permittivity loss or magnetic permeability loss to convert the backscattered energy into heat. Ferrite is an often used material for this purpose, especially in borehole radars, because it has large mechanical strength as well as high dielectric and magnetic losses in the working frequency band of GPR [117]. We set the material properties of borehole radar in our model as shown in Table 3.2, simulating a sintered nickel zinc ferrite material [118].

[1] Trademark of The MathWorks, inc.

Table 3.1: Drilling, fluid, and reservoir properties [45,48,78].

Variables	*Values*	*Units*
Wellbore radius	0.10	m
Mud hydrostatic pressure	27580	kPa
Mud cake maximum thickness	0.005	m
Mud filtrate salinity	1×10^3	ppm
Mud density	1130	kg/m^3
Mud cake reference permeability	0.05	md
Mud cake reference porosity	0.25	fraction
Mud solid fraction	0.06	fraction
Mud cake compressibility exponent	0.4	fraction
Mud cake exponent multiplier	0.1	fraction
Formation pressure	25166	kPa
Formation water salinity	160×10^3	ppm
Formation temperature	93.3	°C
Water density	1001	kg/m^3
Oil density	816	kg/m^3
Water viscosity	1.274×10^{-3}	Pa·s
Oil viscosity	0.355×10^{-3}	Pa·s
Rock compressibility	7.252×10^{-10}	1/kPa
Water compressibility	3.698×10^{-7}	1/kPa
Oil compressibility	2.762×10^{-6}	1/kPa
Connate water saturation	0.15	fraction
Residual oil saturation	0.10	fraction
Endpoint relative permeability of water	0.3	fraction
Endpoint relative permeability of oil	1	fraction
Empirical exponent of water relative permeability	2	dimensionless
Empirical exponent for oil relative permeability	2	dimensionless
Capillary pressure coefficient	1.87×10^{-2}	Pa·m
Empirical exponent for pore-size distribution	20	dimensionless
Diffusion coefficient of salt	6.45×10^{-9}	m^2/s
Dispersion coefficient of salt	1.3×10^{-3}	m
Vertical to horizontal ratio of formation permeability	0.10	fraction

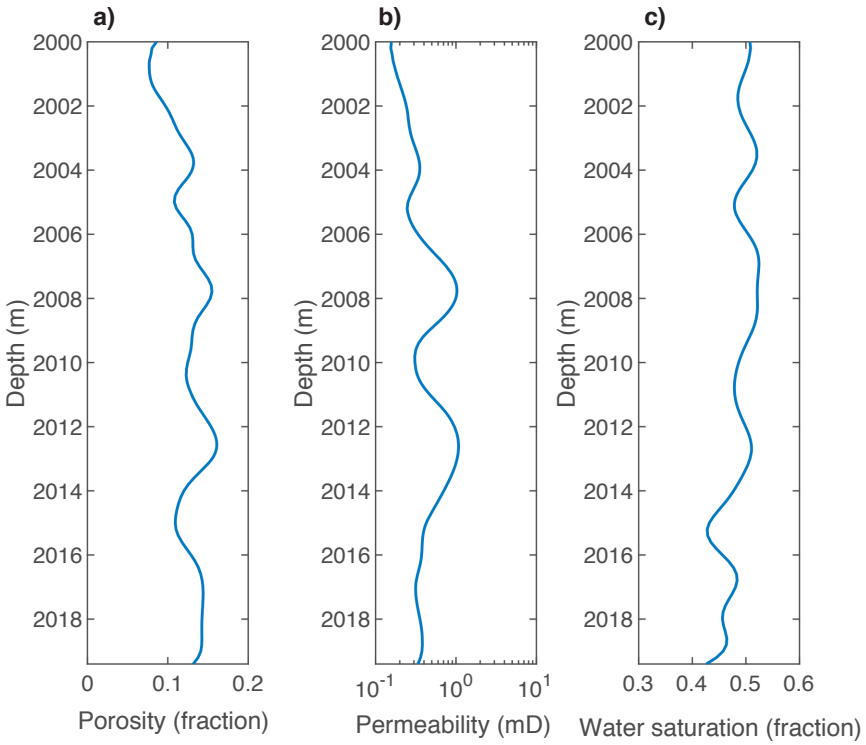

Figure 3.1: Porosity, permeability, and water saturation curves based on the coring data from a well in the Honghe Oilfield, Ordos, China. The data have been smoothed using a five-point moving average filter.

The absorbing effect in the considered radar frequency range is not optimal but still adequately effective. The downhole transreceiver configuration is designed as a one-transmitting and two-receiving mode that resembles the common depth point measurement on the surface, which facilitates a time-to-depth conversion for invasion depth estimation. A Ricker wavelet with a center frequency of 1 GHz is applied to the transmitting antenna. This frequency range satisfies the penetration depth and spatial resolution required in a high-resistivity reservoir [39]. A backward caliper arm in the logging string can push the antennas against the borehole wall to eliminate attenuation and scattering loss caused by the conductive mud. Similar caliper arm configurations have been used in density logging, micro-resistivity logging and dielectric logging tools, where it is required to directionally inject energy into the formation in an open hole [84,119].

We use gprMax, a general purpose finite-difference time-domain (FDTD) GPR simulator [83], to build up a borehole radar model for a mud-filled downhole environment. The antennas are modeled as Hertzian dipoles with the polarization direction parallel to the borehole. This configuration is used as an approximation to the wire dipole antennas designed by [120]. We choose the electrical field component parallel to the borehole as the received signals. The FDTD grid has a uniform spatial step with 2 mm on the side, and the time step is chosen based on the CFL limit [121]. Perfectly matched layers are imposed in the domain boundaries to simulate an infinite propagation space [122,123].

The porosity, water saturation and salinity are initially extracted from the mud invasion simulations. Subsequently, the aforementioned properties are converted to bulk permittivity and conductivity, and then are implemented into the radar model. To that end, two sets of formulas, i.e., Archie's law and the complex refractive index model (CRIM) as described in Appendix A.2, are used to calculate the electrical properties of the mixed materials, by which the radar and flow models can be coupled in the associated simulations. Archie's law is a good approximation to calculate the bulk electrical conductivity in our scenario of a resistive sandstone-type reservoir. CRIM is a widely used dielectric mixing formula, and it is still valid in reservoir environments when the frequency is relatively high (> 100 MHz) and interfacial polarization does not occur [84]. Under the deep reservoir environments, the relative permittivity of water, which is 81 under ambient conditions, should be modified. Donadille *et al.* carry out laboratory measurements of water permittivity under the condition of high temperature, high pressure and high salinity, and revealed that temperature has a major impact on water permittivity, and salinity has a moderate impact on it, whereas pressure effects is negligible [124]. We include the salinity and temperature effects on the water permittivity in our CRIM model through a polynomial interpolation of the laboratory data measured by Donadille *et al.* [124], as depicted in Figure 3.2. Considerable differences relative to the surface GPR measurements are that water relative permittivity drops to approximately 58 at the temperature of 100 °C, and its magnitude decreases with the increase of the water salinity. Besides, water permittivity becomes frequency independent in our applied radar frequency range because the relaxation frequency shifts to approximately 50 GHz as the temperature rises to 100 °C, implying that the dipole losses of water is negligible [84].

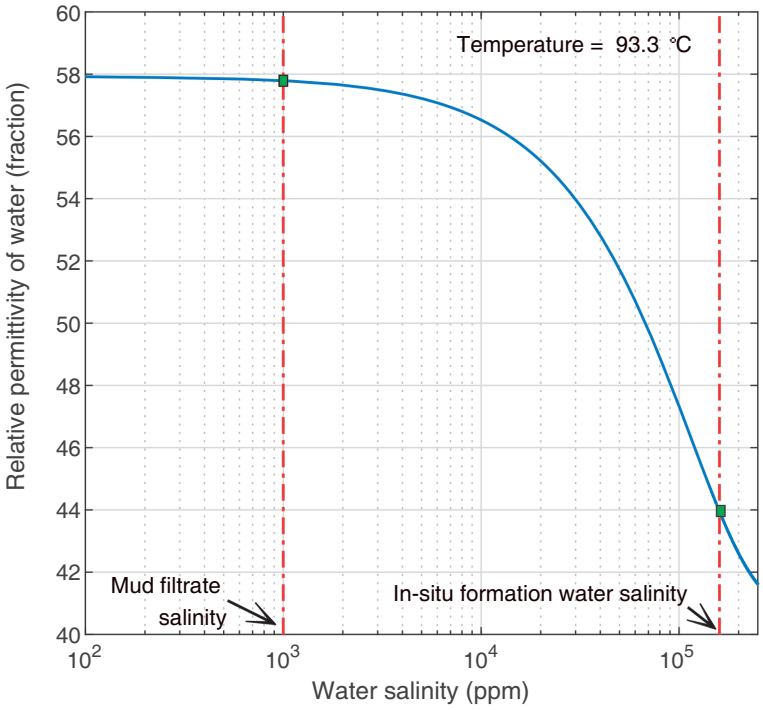

Figure 3.2: Relative permittivity of water as a function of salinity at the temperature of the simulated reservoir for the frequency of 1 GHz.

The downhole antenna configurations and the coupled fluid flow model are illustrated in Figure 3.3. The geometric parameters of the borehole radar and the material properties of the borehole and the reservoir are presented in Table 3.2. Through the coupling of the flow and radar models, a real-time borehole radar response of invasion process can be simulated.

3.2.3. FLUID DISTRIBUTION AND RADAR RESPONSES

The spatial distributions of the fluid and electrical properties during the invasion process are derived from the mud invasion simulations. Figure 3.4 shows the 2D fluid and electrical property distributions after 36 hours of invasion, and Figure 3.5 compares the radial fluid and electrical property curves after 36 and 60 hours. We can see that the invaded reservoir presents a relatively flat flushed zone and a sharp transition zone, which is favorable for radar wave propagation and reflection. Recall that we simulate a light oil reservoir scenario, where a low oil-water viscosity ratio takes primary responsibility for the piston-like invasion profile. We also see that the evolution of water

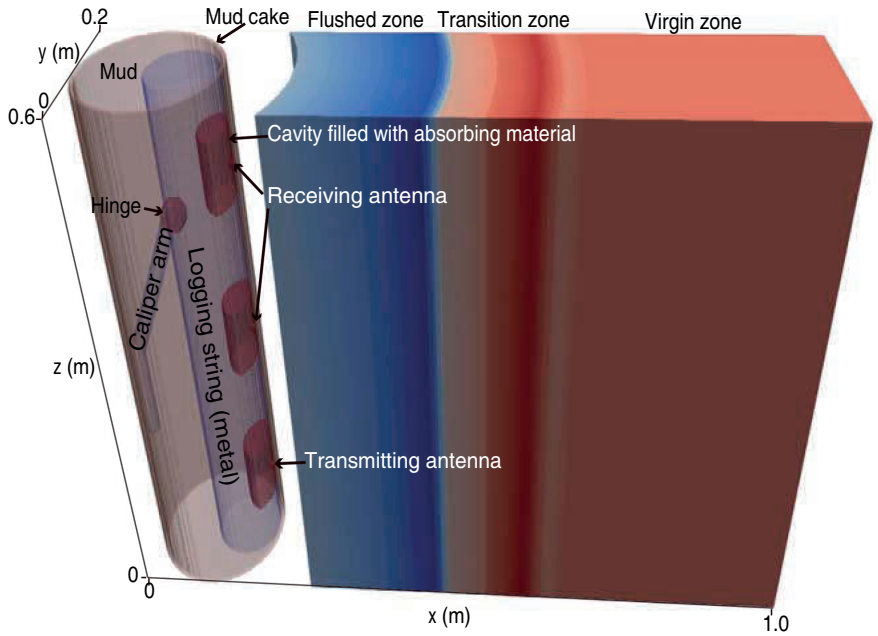

Figure 3.3: Schematic presentation of borehole radar model configuration and fluid distribution. Colors denote the materials with different electrical properties.

Table 3.2: Geometric parameters and electrical properties for borehole radar and reservoir models.

Variables	*Values*	*Units*
Logging string radius	0.05	m
First transmitter−receiver spacing	0.20	m
Second transmitter−receiver spacing	0.40	m
Radial depth of cavity	0.04	m
Longitudinal length of cavity	0.08	m
Real part of relative permittivity of absorbing material	20	dimensionless
Imaginary part of relative permittivity of absorbing material	9	dimensionless
Real part of magnetic permeability of absorbing material	1.20	dimensionless
Imaginary part of magnetic permeability of absorbing material	12	dimensionless
Tortuosity factor	1.00	dimensionless
Cementation exponent	2.00	dimensionless
Saturation exponent	2.00	dimensionless
Relative permittivity of oil	2.00	dimensionless
Relative permittivity of dry sandstone	4.65	dimensionless
Relative permittivity of water for 1 GHz at 93.3 °C	57.93	dimensionless

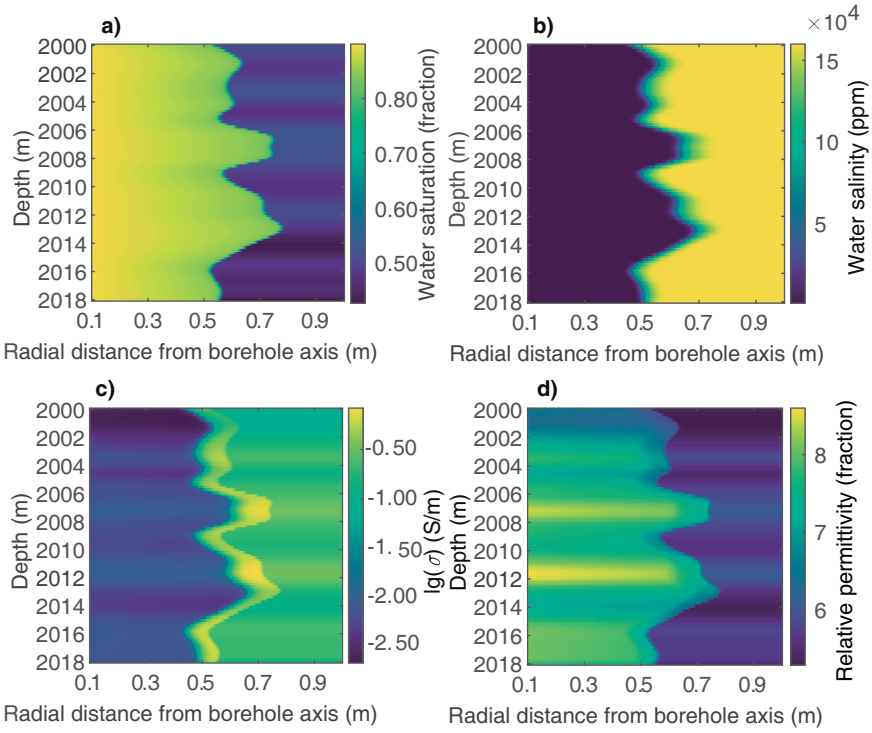

Figure 3.4: 2D distributions of water saturation (a), water salinity (b), bulk conductivity (c), and bulk relative permittivity (d) after 36 hours of invasion. Note that the x-axis starts from the borehole wall.

salinity lags behind the water saturation. This phenomenon is caused by the diffusion and dispersion of the different saline concentrations between the in-situ formation water and the invading mud water. The lag effect is thought to be responsible for the so-called low-resistivity annulus (i.e., the high-conductivity annulus in Figure 3.5) [48]. We observe that the evolution of the conductivity over time is consistent with that of the water salinity, while the permittivity with the water saturation. Note that an abnormal drop in the relative permittivity curve is caused by the impact of the salinity on the water permittivity. From the character of electrical property profiles, we expect that the significant radar wave reflection events are largely governed by the discontinuity of the conductivity distribution rather than by that of the permittivity.

Comparing the shapes of the invasion profiles at different times, we find that the electrical properties of the flushed zone change much less over invasion time than those of the transition zone. Therefore, we propose to perform time-lapse logging measurements to extract the reflected signals from the transition zone. Time-lapse logging has proven to be effective for extracting information with regard to changes in the rock physical properties especially when applied to fluid flow monitoring [125]. Miorali *et al.* used time-lapse borehole radar measurements to extract the reflected signals from

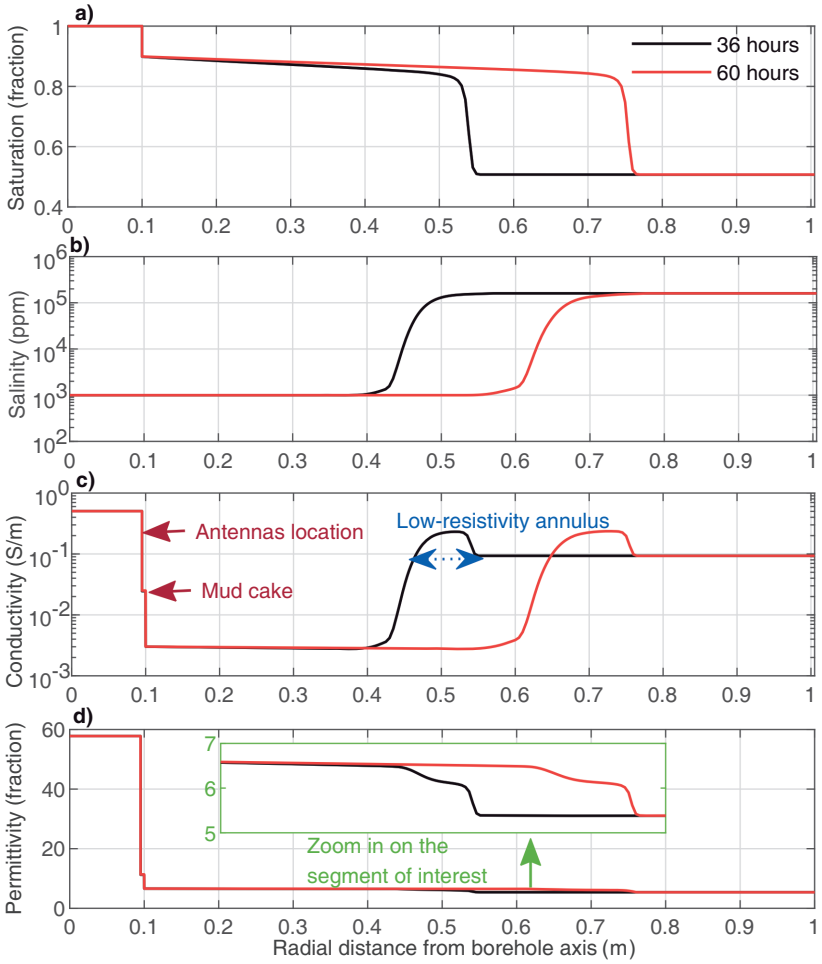

Figure 3.5: Radial distributions of water saturation (a), water salinity (b), bulk conductivity (c), and bulk relative permittivity (d) after 36 (black curves) and 60 hours (red curves) of invasion, respectively. The 1D curves are extracted from the simulated data at a depth of 2000 m. The radial ranges of 0–0.95 m and 0.95–1 m denote the borehole and mud cake parts, respectively.

the water-oil contact [40]. In our case, time-lapse logging is expected to filter out the majority of the direct wave as well as the clutter arising from the heterogeneous rock properties. We implement time-lapse operations between times of 36 and 60 hours (the time interval issue has been discussed in Chapter 2), and record the time-lapse radar signals at two receivers as shown in Figure 3.6. There are three events observed in each radar profile. The first one close to the wellbore is caused by the changes in the near-borehole fluid content and the mud cake properties. These changes are minimal. However, because they are closely adjacent to the antennas, strong time-lapse signals are generated. The other two reflection events come from the invasion transition zone at 36 and 60 hours, respectively. The choice of the logging times is based on the consideration that it should allow for separating different events. In practice, to acquire high-quality time-lapse signals, it is crucial to keep a relatively small shift of the locations of antennas in the radial and azimuthal directions for each sequential logging operation.

3.3. PERMEABILITY ESTIMATION

3.3.1. ESTIMATION OF INVASION DEPTH

We configure the receiving radar antennas with two different offsets in the logging string (Figure 3.3), which allows for time-to-depth conversion. The depth and wave velocity are simultaneously determined using the equations

$$\begin{cases} 2\sqrt{(l_1/2)^2 + {d_x}^2} = v_x(t_1 - \tau), \\ 2\sqrt{(l_2/2)^2 + {d_x}^2} = v_x(t_2 - \tau), \end{cases} \tag{3.1}$$

where l_1 and l_2 are the known offsets of the transmitting and receiving antennas, respectively, t_1 and t_2 denote the picked travel times of the reflected waves in the two receivers, τ is half of the time period of the source wavelength in the transmitter, and v_x and d_x are respectively the average wave velocity and the invasion depth, which are to be solved in the equations. The spacings l_1 and l_2 between the transmitting and receiving antennas are defined in Table 3.2 and designed to be comparable with the invasion depth range. The travel times t_1 and t_2 of the reflected signals are picked up from the peaks of the waves of the second event (Figure 3.6). It is important to note that the travel times of the reflected signals should be calibrated by the period of the half wavelength (τ), because the real starting time of the source wavelet is difficult to pick with confidence. To estimate the period of the half-wavelength, we extract the time of the peaks of the direct waves in the radar data from the two receivers prior to the time-lapse difference operations and then solve for τ by setting d=0 in equation 3.1.

Figure 3.7 compares the invasion depth estimated from the radar data and the conductivity distribution simulated from fluid flow model. It can be seen that the estimated invasion depth is located at the starting point of the high conductivity annulus, which verifies that the reflection events occur at the discontinuity of the conductivity as predicted above. The agreement implies that the proposed mud invasion characterization approach is capable of estimating the invasion depth effectively and accurately.

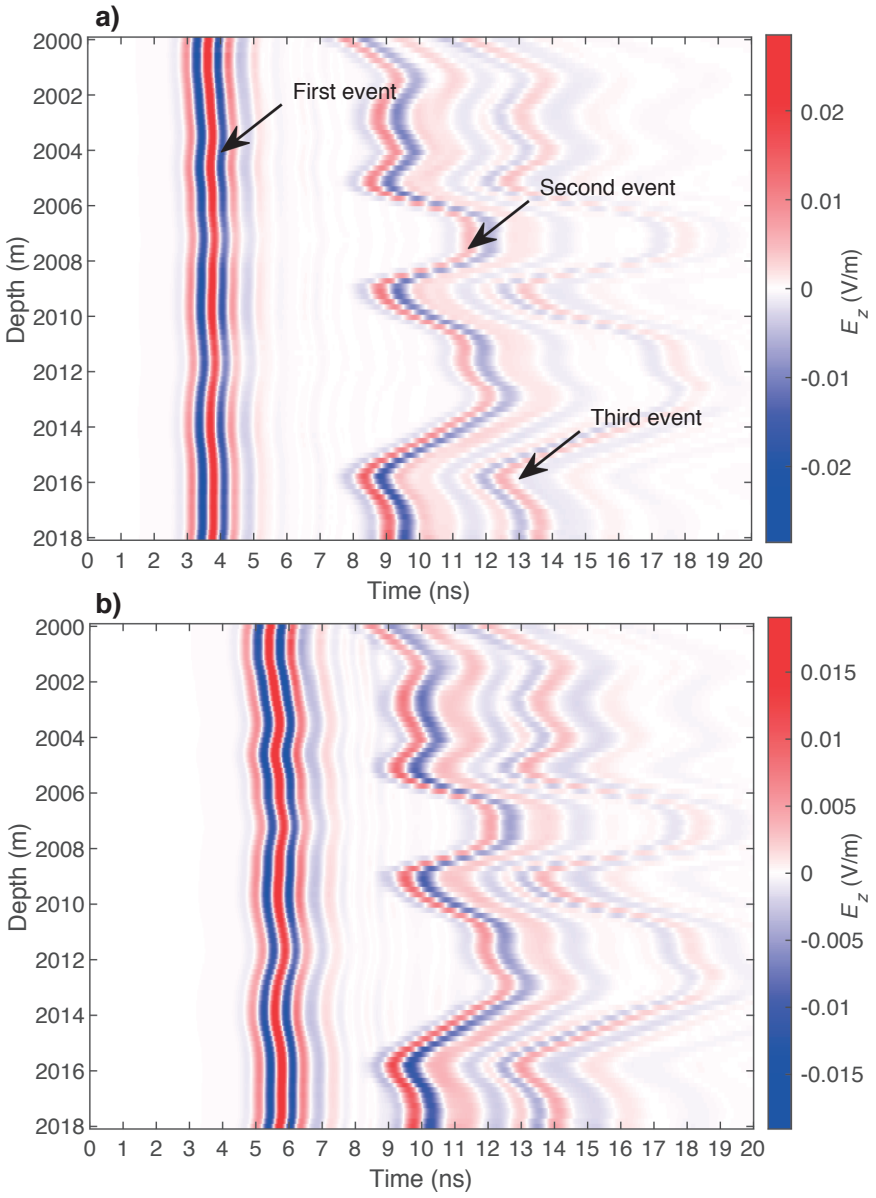

Figure 3.6: Time-lapse radar profiles acquired by the first (a) and second (b) receiving antennas with the measurements after 36 and 60 hours of invasion, respectively.

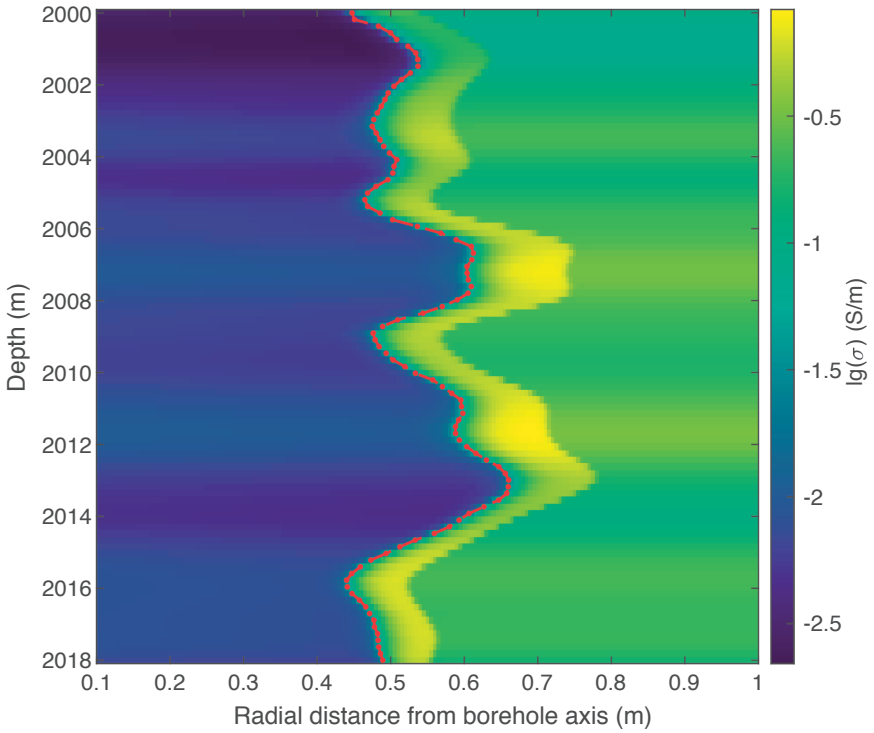

Figure 3.7: Radar-estimated invasion depth versus the simulated conductivity distribution after 36 hours of invasion. The red dotted line presents the invasion depth estimated by borehole radar data, and the varying colors denote the electrical conductivity on a logarithmic scale.

3.3.2. ESTIMATING PERMEABILITY

Generally, the properties related to fluids, such as viscosity, compressibility, relative permeability curves, and capillary pressure features, in a given reservoir interval are constant, whereas the permeability, porosity, and initial water saturation vary with reservoir depth [47]. The reservoir permeability and mud cake permeability both affect the inflow rate of the mud filtrate [48]. Therefore, a high formation permeability normally causes a large invasion rate and thus a large invasion volume at a certain invasion time. Formation porosity per se does not influence the invasion rate if its correlation with the permeability is ignored. Under this assumption, a lower porosity leads to a larger invasion depth for a given invasion volume because the smaller pores require a larger invasion depth to contain the same volume of fluids. Initial water saturation has no straightforward correlation with the invasion rate. However, the water saturation determines the capillary pressure and relative permeabilities [115], which implicitly

relates the initial water saturation with the invasion rate. A systematic analysis of the parametric sensitivity revealed the following relationships of the invasion depth and the reservoir properties [50,81]. First, there exists a strong correlation between the invasion depth and the permeability in low-permeability reservoirs. However, the correlation becomes poor when the reservoir permeability is large. This is because a high reservoir permeability leads to a large pressure drop across the mud cake, which increases the mud cake permeability due to the mud cake compressibility and makes it dominant in the invasion rate [43]. Second, porosity has a negative correlation with the invasion depth because a high porosity means a short length to contain the same filtrate volume, and the invasion depth is more sensitive to a low porosity reservoir than a high one. Third, initial water saturation has a minor influence on the invasion depth, but a high initial water saturation tends to form an indistinctive contrast between the flushed and virgin zones. Correlation analysis implied that one can estimate reservoir permeability with the obtained invasion depth once the porosity and water saturation, as well as the drilling and coring data, are available.

A 4D interpretation chart can be used for estimating the reservoir permeability, for which a sequence of mud invasion simulations are required to map varying porosity, permeability, and initial water saturation values to their corresponding invasion depths. The interpretation chart assumes that the properties of mud cake, fluids and formation are available as prior knowledge. In practical field applications, the mud and mud cake parameters are determined by the drilling fluid configuration scheme. Core sample analysis can acquire the fluid and rock properties, e.g., capillary pressure, relative permeabilities, viscosities, and rock-electric properties. Conventional logging can obtain the initial water saturation, pressure, porosity, and temperature of the reservoir. When the borehole radar solves the invasion depth, permeability can be estimated through the interpretation chart. Figure 3.8 illustrates the corresponding work flow.

Figure 3.9 presents the 4D interpretation chart based on our reservoir scenario after 36 hours of mud invasion, and Figure 3.10 extracts 1D curves from Figure 3.9 showing how the permeability, porosity, and initial water saturation independently influence the invasion depth. We observe that: (1) the initial water saturation has unnoticeable effects on the invasion depth; (2) the porosity has a negative correlation with the invasion depth; and (3) the permeability has a high correlation with the invasion depth and the correlation dramatically drops when the permeability increases to a few milliDarcys. The observed phenomena coincide with our previous parametric sensitivity analyses of mud invasion [50], and suggest that the proposed method is limited in low-porosity and low-permeability reservoirs.

With the invasion depth acquired through borehole radar logging (Figure 3.11), we estimate the permeability based on the calibrated data in Figure 3.9. The corresponding results are presented in Figure 3.11b. Compared with the preset permeability curves, the estimated permeability curve shows a good agreement. The discrepancies are mainly caused by the decimal precision limit of 0.01 that we impose on the initial water saturation and porosity as the variables imported into the interpretation chart, imitating

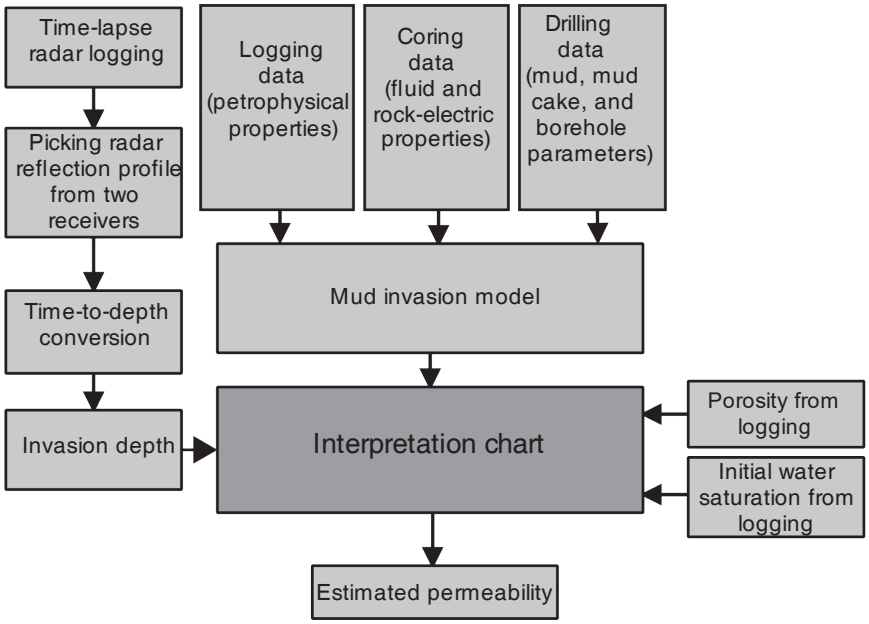

Figure 3.8: Flow chart illustrating the estimation of permeability based on borehole radar measurements.

3

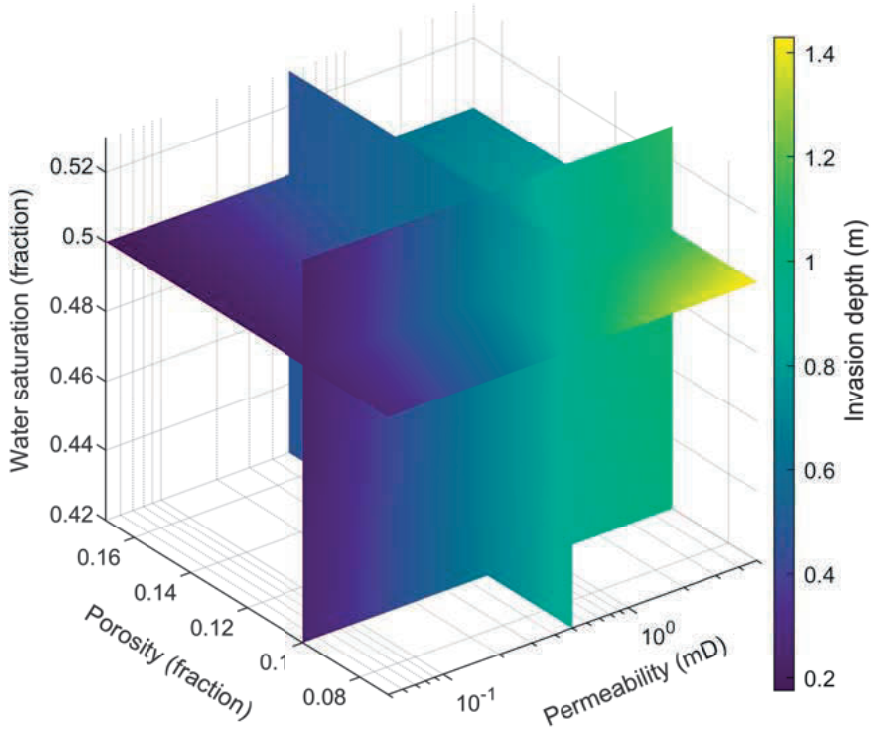

Figure 3.9: 4D interpretation chart presented by slices associating invasion depth (calculated from the borehole axis) with porosity, permeability, and initial water saturation after 36 hours of invasion for the reservoir scenario defined in Table 3.1. The data has been processed by linear interpolation.

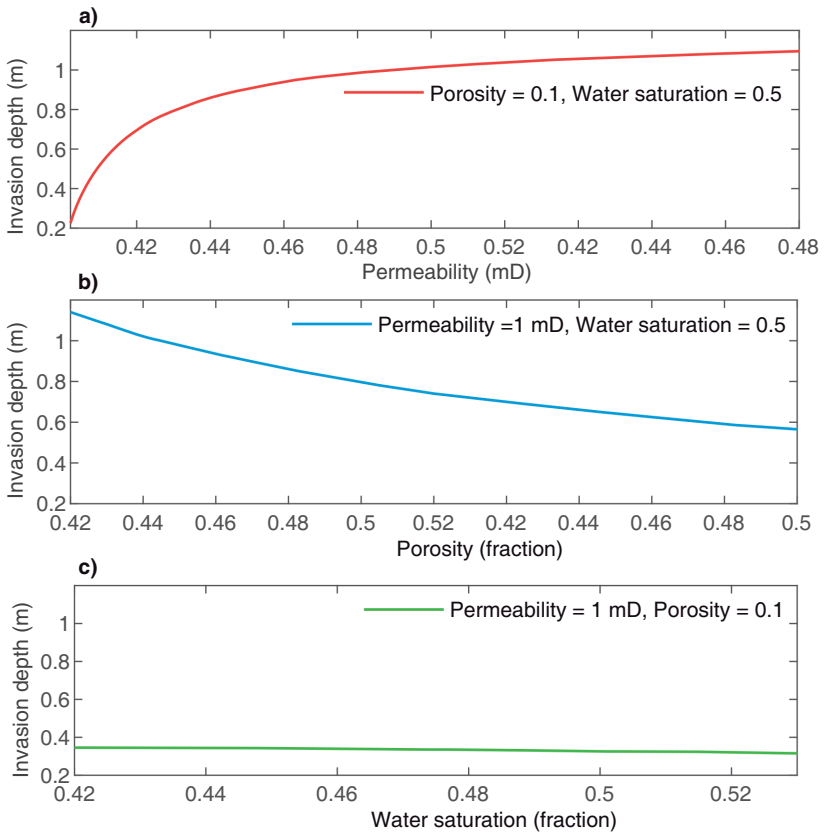

Figure 3.10: 1D curves extracted from Figure 3.9 associating invasion depth with permeability (a), porosity (b), and initial water saturation (c).

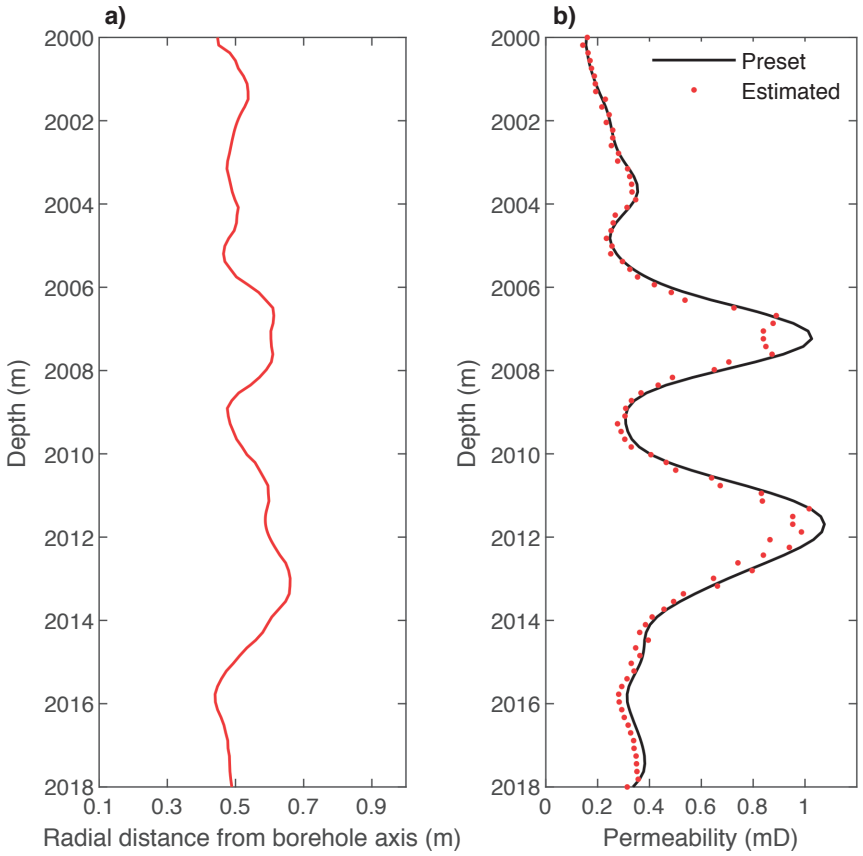

Figure 3.11: Invasion depth acquired through borehole radar (a) and the comparison between the estimated and preset permeability curves (b).

the imperfect data measurements of the conventional logging in practice. Besides, it can been seen that the absolute errors in the high permeability segments (i.e., the two peaks) are higher than those in the low permeability ones, which proves that the proposed method is better suited to lower permeability intervals.

The simulation results imply that, in principle, the permeability can be estimated based on the mud invasion depth inferred from borehole radar measurements. However, an accurate permeability estimation heavily relies on the comprehensive collection and precise analysis of drilling, coring, and logging data. In practical borehole radar logging, the instrument operations and signal processing methods affect the accuracy and precision of the proposed method. An ideal application environment of borehole radar is a low-porosity and low-permeability hydrocarbon reservoir drilled using freshwater mud and followed by open-hole logging. Future work will include sensitivity analyses to the error sources and the recommendations on how to make this approach more viable

for practical applications.

3.4. CONCLUSIONS

This chapter proposes a new methodology of estimating reservoir permeability via the mud invasion depth detected by borehole radar. The measurement configuration consists of two receivers and one transmitter operating at 1 GHz center frequency. Time-lapse measurements are employed to effectively extract the reflected signals from the invasion front. The permeability is estimated based on interpretation charts that relate the invasion depth with the petrophysical properties of the reservoir. A numerical study is presented, which couples fluid flow and radar modelling to accurately simulate the investigated scenario consisting of a low-porosity and low-permeability reservoir drilled using fresh water-based mud. The results indicate that borehole radar has potential for the estimation of the reservoir permeability. The work in this chapter demonstrates a potential application of GPR in oil well logging as an effective solution for permeability estimation problem.

4

RESERVOIR MONITORING USING BOREHOLE RADARS TO IMPROVE OIL RECOVERY: SUGGESTIONS FROM 3D EM AND FLUID MODELLING

SUMMARY

The recently developed smart well technology allows for sectionalized production control by means of downhole inflow control valves and monitoring devices. We consider borehole radar as permanently installed downhole sensors to monitor fluid evolution in reservoirs, and it provides possibility to support a proactive control for smart well production. To investigate the potential of borehole radar on monitoring reservoirs, a three-dimensional numerical model is established by coupling electromagnetic propagation and multiphase flow modelling in a bottom-water drive reservoir environment. Simulation results indicate that time-lapse downhole radar measurements can capture the evolution of water and oil distributions in the proximity (order of meters) of a production well, and reservoir imaging with an array of downhole radars successfully reconstructs the profile of flowing water front. With the information of reservoir dynamics, a proactive control procedure with smart well production is conducted. This method delays the time of water breakthrough, and extends the period of water-free recovery. To assess potential benefits that borehole radar brings to hydrocarbon recovery, three production strategies are simulated in a thin oil rim reservoir scenario, i.e., a conventional well production, a reactive production, and a combined production supported by borehole radar monitoring. Relative to the reactive strategy, the combined strategy reduces cumulative water production by 66.89%, 1.75%, and 0.45%, while

increases cumulative oil production by 4.76%, 0.57%, and 0.31%, in the production periods of 1 year, 5 years, and 10 years, respectively. The quantitative comparisons reflect that the combined production strategy has capability of accelerating oil production and suppressing water production, especially in the early stage of production. We suggest that borehole radar is a promising reservoir monitoring technology, and it has potential to improve oil recovery efficiency.

The content of this chapter is based on the following paper:

F. Zhou, M. Miorali, E. Slob, and X. Hu, Reservoir monitoring using borehole radars to improve oil recovery: Suggestions from 3D electromagnetic and fluid modeling, *Geophysics*, vol. 83, no. 2, pp. WB19–WB32, 2018.

4.1. INTRODUCTION

Ground-penetrating radar, usually working in the frequency range from tens of megahertz to several gigahertz, has been widely applied in mapping near surface geologic structures [126]. High-frequency EM waves are sensitive to water content due to the great contrast of permittivity between water and other soil or rock components. Therefore, GPR can been applied in groundwater assessment. Especially, a time-lapse GPR measurement method is widely used to monitor the migration of water or steam in shallow (tens of meters) fractures or vadose zones [67,69,70]. To overcome the limited detection depth of surface GPR, borehole radar is utilized by deploying antennas under the surface [75,127]. Cross-hole, single-hole and vertical radar profiling measurements have been conducted for fracture and cavity detection, metal ore exploration, and underground water assessments [21,22,128–130]. Some novel types of GPR antennas have been designed to suit for downhole materials and structure. A typical example is the polarimetric borehole radar that can estimate target orientation and fracture roughness [104,131,132]. In their applications, borehole radars are deployed at a depth of tens to hundreds of meters under the ground. Even deeper applications of GPR technology, for example, hydrocarbon reservoirs at a depth of up to thousands of meters, have been proposed [38,39]. Recently, laboratory experiments were conducted to emulate EM response of a wideband radar on the perforations and impairments of an oil well [42], and a borehole radar prototype system has been developed for oil well logging usage [108].

Current studies for GPR applications in oil fields have mainly focused on hydrocarbon exploration activities, where radar antennas are designed in a logging string or drill collar for wireline logging or logging while drilling (LWD), respectively [39,133,134]. However, in our view, another potential application of GPR in oil fields resides in hydrocarbon development activities. In this application, downhole GPR is thought to have capability of monitoring the movement of water and oil, and it can help to improve oil recovery efficiency when combined with a so-called smart well.

Smart well (or intelligent well) is an advanced well equipped with downhole sensors and inflow control valves (ICVs) to monitor and control hydrocarbon production [135]. The well is separated into several relatively independent segments or completions by packers between the casing and tubing. ICVs segmentally control the inflow of liquids from the casing to the tubing. The valves can be choked in a one-off, discretely variable, or infinitely variable mode. Downhole electrical cables or hydraulic conduits provide remote control to the valves from the surface [136]. Permanent downhole sensors continuously or semi-continuously monitor production status inside or outside the well, and the reservoir information is delivered to the surface control center through downhole communication systems [137]. Smart wellbore facilities have been developed, and early applications have demonstrated great attractions to the oil industries [138]. A simple structure of a typical smart wellbore is schematically presented in Figure 4.1. Combined with a suitable monitoring and control strategy, smart well is capable of improving reservoir management and increasing recovery efficiency [139].

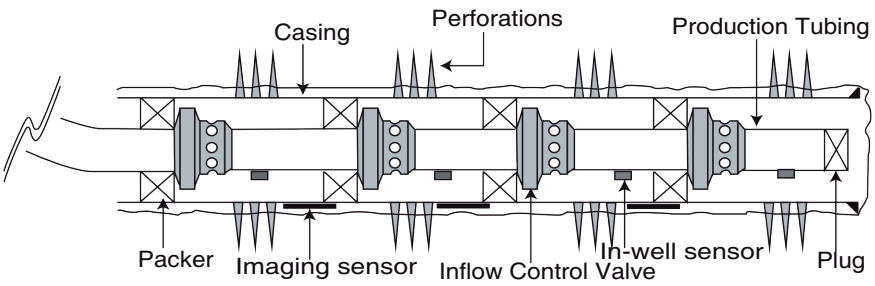

Figure 4.1: Schematic representation of a conceptual smart wellbore in horizontal well production. Downhole cables are not presented [140].

4

However, a practical smart well optimization strategy is limited by poor knowledge of reservoir fluid behaviors. The task of smart well sensing technology is to acquire information from reservoirs or wells. With adequate reservoir dynamic information, data-driving feedback control strategies are realizable [141]. Generally, the downhole monitoring can be categorized into in-well sensing and reservoir imaging. In-well senors are currently technologically mature, and have been installed in realistic smart wells [139]. Examples of successfully applied in-well monitoring techniques include pressure gauges, temperature sensors, and multiphase flow meters based on fiber optics [54–56]. These tools can only monitor fluid changes inside or closely adjacent to the well. For sensing far away from the well, reservoir imaging technology, whether on ground or downhole, are imperative. Surface 4D seismic has been used to characterize the distributions of remaining oil through the differences of data surveyed over time [142]. However, because of the long intervals (normally at a few years) of data acquirements, the measurement backgrounds are usually changed, wherefore time-lapse data processing is difficult to produce the results with high accuracy, high resolution, and high signal-to-noise ratio [59]. Permanently installed downhole geophones are expected to be able to indirectly locate the displacement front, but data interpretation is difficult because of the natural insensitivity of elastic waves on fluid components [143]. To date, no downhole seismic has been permanently installed in a smart well system in spite of its successful applications to downhole fracturing monitoring [144]. 4D gravity can infer density changes of fluids associated with hydrocarbon production, whereby it is viable in monitoring gas-water rather than oil-water displacement [145]. Nowadays, a downhole gravity tool exists only in a wireline logging mode, but a gravity monitoring tool permanently installed in the downhole is still unavailable [146]. Recent theoretical and experimental studies found that considerable signals of streaming potential, which respond to approaching water, are detectable in a production well, and the investigation distance ranges from tens of meters up to a few hundred meters [147]. However, the measured magnitude is limited by production rate, formation water salinity, and the coupling coefficient between fluids and electric potential, among which the latter two are poorly understood [148]. These reservoir imaging techniques, even though some of them are under development, suit only for a large-scale (tens to hundreds of meters) water flooding monitoring with a low-resolution requirement. In

addition, the responded signals are difficult to directly image displacement front, and data interpretation is cumbersome and uncertain. So far, a proper tool does not exist to precisely resolve the near-well region from several to tens of meters. However, the monitoring of this region is strongly required in some specific production environments. Two examples are thin oil rims produced by horizontal wells and heavy oil reservoirs produced through steam-assisted gravity drainage (SAGD). Thin oil rim reservoirs are relatively thin oil columns (in an order of a few to tens of meters), sandwiched between water and gas or shale. In the case of horizontal well production, they often encounter early water breakthrough caused by reservoir heterogeneity and wellbore pressure drop [60]. SAGD is an enhanced oil recovery technology for heavy crude oil production. Two horizontal wells are parallelly drilled through the oil-bearing layer, with the upper for steam injection and the lower for heated oil collection [62]. The main challenge is to let the steam chamber grow in a controllable way to reduce the production of steam or condensate water. In both recovery environments, an investigation depth of several meters away from the well can support production optimization by means of smart wells.

From a more general perspective, realistic reservoirs have heterogeneous permeability, or contain fractures or channels, presenting an uneven displacement front when flooded or derived. The nonuniform displacement causes premature breakthrough of undesired fluids (e.g., water, gas, or steam), and thus reduces oil production, especially in the case of horizontal well production. If downhole imaging techniques are capable of capturing fluid changes in the reservoirs, then they can support an effective production control with smart well [149].

The objectives of production optimizations are to maximize oil production, minimize undesired fluid production, or gain an optimal net present value [149]. The production controls with ICVs can be either reactive or proactive (or termed “defensive”). Reactive control adjusts the settings of ICVs after the unwanted fluids invade the well, whereas proactive control responds to flow changes measured or predicted at a distance away from the well. Downhole multiphase flow meters are commercially available, which allows for in-well water cut measurements for reactive control. Early investigations showed that a proportional reactive control, employing continuously variable ICV settings for segmental inflow adjustment, can yield a neutral or positive economic return compared with the uncontrolled conventional well, flow-fixed segmented well, and ON/OFF reactive control productions [52]. Proactive control is hopeful to yield more benefits for its early warning to water invasion, while the applicability strongly depends on reservoir imaging technology. Currently on-going reservoir imaging techniques, as mentioned before, fail to monitor the near-well region (a few to tens of meters from wells). Our previous work evaluated the feasibility of GPR detecting water front based on EM propagation theory, and suggested that in a relatively low-conductivity reservoir (σ <0.02 S/m), a detection range of 10 m is obtainable [40,41]. Based on these, we propose that borehole radar might be an effective downhole monitoring tool to support a proactive control in a thin oil reservoir production.

This chapter investigates the capability of borehole radars for imaging reservoirs, and then quantifies its contributions to oil production. Firstly, an integrated three-dimensional numerical model is established by coupling multiphase flow and EM propagation modelling. The model imitates a bottom-water drive reservoir produced by a horizontal well where radar antennas are installed. A box-scale simulation is implemented to investigate the capability of borehole radar detecting water front in the way of time-lapse measurements. Secondly, to examine the effectiveness of borehole radar imaging, a reservoir-scale simulation is conducted in a thin oil rim scenario. An array of borehole radars is assumed to be distributed in a horizontal well, and the traces of received signals are gathered to image the advancing water front profile. Then, the imaging results are used to implement a proactive control procedure of smart well. Finally, to assess the potential benefits that borehole radars bring to oil production, three different production strategies are simulated and compared. A conventional well production, with no monitoring and control devices, is simulated as a reference case. The second production strategy adopts a proportional reactive control, which gradually adjusts ICVs after water breakthrough, and this control strategy is thought of as the optimum smart well production strategy in the currently technologically available level [52]. The third production strategy combines proactive control with proportional reactive control, and it can adjust ICVs before and after water breakthrough. In this production strategy, in addition to multiphase flow meters, the well is equipped with reservoir monitoring tools, which can be supported by our borehole radars.

4.2. WATER FRONT MONITORING USING BOREHOLE RADAR

4.2.1. FLOW MODELLING

Multiphase flow is simulated using an in-house reservoir simulator—MoReS (Modular Reservoir Simulator) [150]. The flow model (labeled as Model 1) is a box-shaped oil-bearing reservoir sandwiched between a shale and an active aquifer, with a dimensions of 100 m×200 m×42.5 m. The heterogeneous porosity and permeability are similar to the scenario in MoReS–Atlas examples [151]. A horizontal well, with the surface production rate of 275 m^3/d, is located below the shale. The principal properties of fluids and rock are listed in Table 4.1, and capillary pressure is considered.

The reservoir model is discretized by nonuniform grids. The region in the proximity of the wellbore, 60 m×20 m×10 m, is discretized with a cell size of 0.5 m×0.5 m×0.1 m. The fine gridding scheme allows to simulate a realistic oil-water transition zone. The permeability and porosity in this region are zoomed out, as shown in Figure 4.2. Coarse gridding is applied outside this region with cell sizes of exponential growth for saving computing time and computer memory.

4.2.2. RADAR MODELLING

We used GprMax, a ground penetrating radar data simulator based on finite-difference time-domain (FDTD) method, to simulate EM waves propagating and scattering in the

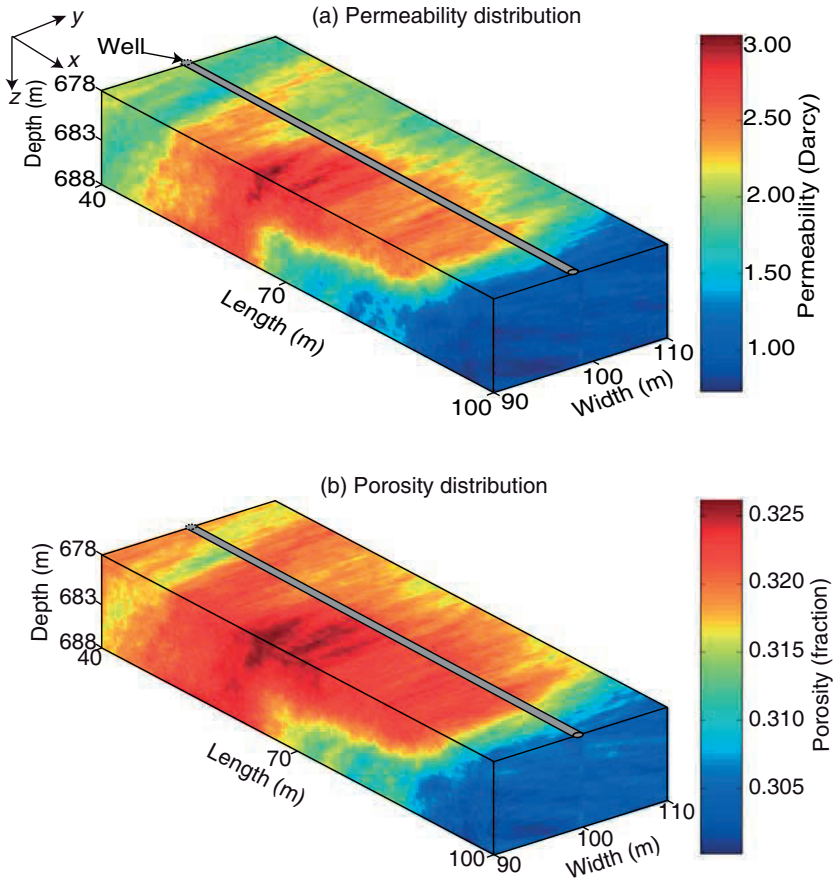

Figure 4.2: Horizontal permeability (Figure 4.2a) and porosity (Figure 4.2b) in the fine gridding region (The ratio of the vertical and horizontal permeabilities is 0.6).

Table 4.1: Properties of fluids and rock for Model 1

Reservoir and well parameters		
Variables	Values	Units
Initial pressure at reference depth	10000	kPa
Rock compressibility	2.00e-9	$(kPa)^{-1}$
Water compressibility	4.35e-7	$(kPa)^{-1}$
Oil compressibility	2.28e-7	$(kPa)^{-1}$
Water density	999.50	kg/m^3
Oil density	888.40	kg/m^3
Water viscosity	5.00e-4	Pa·s
Oil viscosity	3.40e-4	Pa·s
Connate water saturation	0.25	fraction
Residual oil saturation	0.25	fraction
Water end-point relative permeability	0.80	fraction
Oil end-point relative permeability	0.80	fraction
Water Corey exponent	2	dimensionless
Oil Corey exponent	2	dimensionless

reservoir [152]. The main properties affecting EM wave propagation are conductivity and permittivity of the mixed media. The oil-bearing layer consists of rock matrix, crude oil, and a small portion of connate water, among which the connate water is the primary contribution to EM propagation attenuation. As analysed by Chen *et al.*, reservoir conductivity is the primary constraint for borehole radar usage [38]. Studies also found that, in a relatively high-resistivity reservoir (e.g., conductivity in an order of 10^{-2} S/m or less), when the frequency is above 100 MHz, attenuation and phase distortion become independent on frequency, and dispersion is negligible while attenuation is tolerable [41]. Such a reservoir condition is readily satisfied in realistic oil fields, and thus it is a natural regime for a true radar measurement. In the meantime, radar frequency is not suggested to exceed a few GHz in order to avoid dielectric relaxation caused by water molecular polarization [124]. In the limited frequency bands, lower operation frequency tends to achieve larger detection range. Investigations showed that for a reservoir with a conductivity of 0.02 S/m, water front reflection in the range of 10 m is detectable by a commercial GPR system with the center frequency of 100 MHz [40]. We therefore adopt a center frequency of 100 MHz in our radar monitoring simulations, and the oil-bearing reservoir has a conductivity smaller than 0.02 S/m. Under these constraints, the materials in the reservoirs are treated as lossy and isotropic, and the constitutive parameters are frequency independent.

The comprehensive electric conductivity and permittivity are governed by the relative contents of each component in the saturated rock and their respective electric properties. Assuming the rock matrix consists of sandstone, the reservoir bulk conductivity can be calculated by Archie's law. The bulk permittivity of the saturated rock is primarily dominated by the content of water for its permittivity is much greater than that of rock

Table 4.2: EM properties of the components in the reservoir and well

EM properties		
Variables	Values	Units
Rock relative permittivity	7	fraction
Water relative permittivity	80	fraction
Oil relative permittivity	3	fraction
Water conductivity	1	S/m
Cementation exponent	2	dimensionless
Saturation exponent	2	dimensionless
Relative permittivity of filling material	30	dimensionless
Conductivity of filling material	1e-4	S/m

and oil. The bulk permittivity can be calculated with the complex refractive index model (CRIM), which is frequently used for geological materials in the radar frequency. The formulas can be found in Appendix A.2. The electric properties of the components used in the EM modelling are presented in Table 4.2. Note that in this chapter, we neglect the temperature effects on the electrical properties of components contained in reservoirs.

By means of the formulas mentioned above, the multiphase flow model can be coupled with the EM model, allowing to observe the correlations between the radar responses and the water front advancing. Figure 4.3 diagrammatically presents the coupling procedure. Through a sequence of joint simulations at a prescribed time interval, time-lapse EM signals can be extracted by the subtraction between two consecutive EM responses. The time-lapse borehole radar measurement is similar to the 4D seismic survey on the ground [142], but downhole measurements are able to acquire high-resolution data. The time-lapse waveforms carry only the signals reflected from the changed portions of the reservoir caused by fluid flowing. The signals from the unchanged portions, including direct and reflected waves from the heterogeneous rock, are removed by the subtraction operation.

Although the method is theoretically feasible, significant challenge retaining in field operations is how to install radar antennas in the complicated downhole environments. To transmit and receive EM waves towards and from the formation, the radar antennas should be installed outside of the casing and be located as close to the formation as possible. From practical considerations, we propose to reshape the casing by attaching an additional metal bulge outside it and place the antennas inside the groove of the bulge, as depicted in Figure 4.4. The redesigned wellbore does not impair the mechanical strength of the casing, while increases the contact of the antennas with the formation. Antennas are restricted in a wire dipole type due to the limited space available in the cross plane of the groove. However, another general problem is that the emitted EM signals are destructively interfered by the metal body. A solution is to fill a kind of highly dielectric material inside the groove to isolate antennas from metal component. As discussed in the previous chapters, a specific insulating filler with a certain thickness can relieve the unfavorable interference from the metal components. Ferrite is one of

4

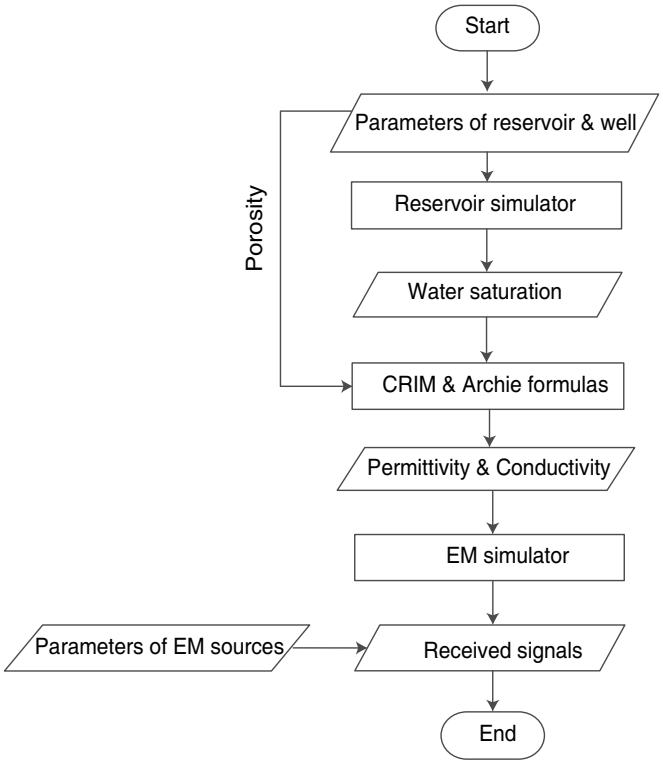

Figure 4.3: Flowchart of coupling multiphase fluid flow and EM propagation models.

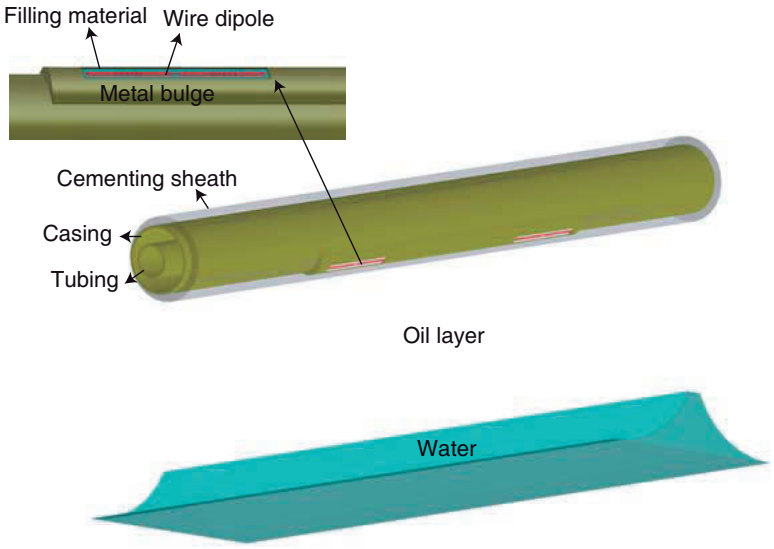

Figure 4.4: Schematic representation of the well configured by radar sensors in a water driving reservoir.

the proper filling materials for our borehole radar applications, because it has similar electric properties as insulating materials as well as high mechanical strength like metal. The metal back cavity of the groove can act as a half shield around the antenna, allowing for directional energy transmitting as well as directional signal collecting, as discussed above. Some other technical issues, such as downhole power supply and data transmission, are not discussed here, since permanent downhole gauges and optical fiber monitoring systems have been successfully applied in smart wells [135]. Radar transceiver modules are also possible to be installed in the limited downhole space with the development of micro-electromechanical systems [153]. Based on the clarification, we believe that it will be technically achievable for borehole radars installed in a smart well.

In the EM simulations, the well casing is deemed a perfect conductor, and the electric properties of the insulated filler and the formation components are presented in Table 4.2. The radar transmitter is treated as a Hertzian dipole source, fed by a first derivative of Gaussian pulse with a center frequency of 100 MHz. The antennas are bistatic, and the transmitter and receiver are separated by 1 m along the well. EM polarization is in the longitudinal direction of the well. The EM simulation domain is discretized by a cell size of 0.025 m$\times$0.025 m$\times$ 0.025 m to satisfy $\Delta l \leq \lambda/10$, where Δl denotes the cell size and λ the minimum wave length in the propagation media. Perfectly matched layer

(PML) boundary conditions are exerted to model an open propagation space in a finite simulation domain.

4.2.3. EM RESPONSES

The reservoir model described above was simulated to demonstrate the dynamics of fluids in the production process, and then the EM model was run to observe the time-lapse radar responses on the movement of fluids. To decrease the computational cost of 3D EM simulations, a box volume of fluid distributions, with the dimensions of 5 m×5 m×10 m, are extracted at the prescribed simulation time. The investigated region is located below the borehole radars, presenting fairly realistic oil-water transition zones due to the fine meshing.

Figure 4.5 shows the evolution of water saturation in the extracted box volume after 150 days, 165 days, 180 days, and 195 days of production, respectively. The corresponding one-dimensional water saturation curves were extracted below the center of the EM source and receiver, as shown in Figure 4.6. It is clearly observed a gradually varying oil-water transition zone, and the leading edge of water displacement is 8.7 m, 6.8 m, 4.7 m, and 2 m away from the well, respectively. In the received signal components, the electric field component that is parallel to the well (i.e., E_x) has the largest response on the water front, thus we only recorded time-lapse E_x components, as shown in Figure 4.7. The waveforms show a gradually strengthened refection event, and the first arrival is respectively at 158.8 ns, 123.2 ns, 81.7 ns, and 31.9 ns, corresponding to the approaching water front (Figures 4.6 and 4.7). Note that other wave components, such as direct waves, residual metal interference, and background clutter arising from inhomogeneous rock pores, carry no useful signals in this application, and they have been mostly filtered by time-lapse operations. The contrast between water saturation profiles and time-lapse EM waveforms indicates that, with every passing 15 days, water front moves forward 1.9 m, 2.1m, and 2.7 m, respectively, and meanwhile the arrival time of reflected waves respectively shortens 35.6 ns, 41.5 ns, and 49.8 ns, presenting a proportional change (Figures 4.6 and 4.7). The positive correlation of both events makes it possible to quantitatively estimate the position or movement speed of water front in different production regions.

For quantitative characterizations of oil-water distributions, it is required to estimate the velocity of EM wave propagating in reservoirs, thereby converting the travel time of radar recordings into distance or depth. There are various approaches for EM wave velocity estimation in GPR measurements, while we propose to estimate EM wave velocity through formation dielectric permittivity for our application cases. A direct way to acquire the reservoir permittivity is to measure coring samples with a coaxial-line sample holder [154]. In addition, an indirect but cheap approach for formation permittivity acquirement is to use a so-called dielectric dispersion logging tool. This kind of wireline EM logging employs multi-spacing, multi-frequency, and cross-polarization antenna arrays to measure attenuation and phase shift of EM wave in different radial depths [84]. Successful field tests have been reported that the tool can simultaneously

inverse the permittivity and conductivity of the virgin formation [155]. Once the prior information of formation permittivity is acquired with the mentioned methods, the wave velocity can be calculated, and thus the water front distance can be converted from the two-way travel time of reflected signals.

4.3. PRODUCTION CONTROLS COMBINED WITH BOREHOLE RADARS

4.3.1. RESERVOIR IMAGING WITH RADAR ARRAY

This section investigates the capability of borehole radar array for reservoir imaging, and develops a valve control method combined with radar imaging results. To assess the practical superiority of borehole radar monitoring reservoir, a production strategy, supported by our borehole radar, is quantitatively compared with a proportional reactive control strategy and an uncontrolled conventional well production.

A conceptual reservoir model (labeled as Model 2) is used in this section. It is a typical reservoir scenario produced by a horizontal well under the drive of strong bottom water pressure, as depicted in Figure 4.8. It is a simplified representation of a thin oil reservoir in Indiana, USA [156], and has been frequently used in smart well production studies [52,157–159]. The model is 1828.8 m long, 944.88 m wide, and 30.48 m thick. The reservoir top is located at a depth of 1828.8 m, and the initial oil-water contact is at a depth of 1859.28 m. The reservoir contains water and oil, while gas is neglected. A horizontal well is located 10.67 m below the top shale layer for oil production. The well is segmented by two individual completions with a perforation length of 365.76 m for each. The primary parameters of reservoir and well are presented in Table 4.3. Capillary pressure is neglected, whereas wellbore friction is considered.

The model is characterized by a high-permeability channel across a low-permeability reservoir. The heterogeneous media will cause uneven water front movement, therefore giving rise to early water breakthrough. As analyzed before, the formation water content primarily controls the radar attenuation and thus the radar detection range [40]. In this scenario, the well is located in the oil-bearing layer where the oil saturation is considerably high (Figure 4.8 and Table 4.3), and therefore the distributions of water content have little variations with position relative to the distributions of permeability and porosity. In view of these analyses, it can be safe to assume a uniform monitoring range (approximately 10 m) for the radar sensors in different well positions.

The reservoir simulations deploy a nonuniform meshing scheme similar to the previous model. The finely gridded portion below the first completion simulates a realistic oil-water transition zone, which is the region of our interest for GPR simulations. In the simulations of array radars, the antenna configurations, boundary condition setting, and gridding scheme are the same to the previous EM model. Multiple radar antennas are distributed along the wellbore with an adjacent space of 28 m (Figure 4.9a). A cluster of GPR traces (i.e., one-dimensional time-lapse EM waveforms obtained by

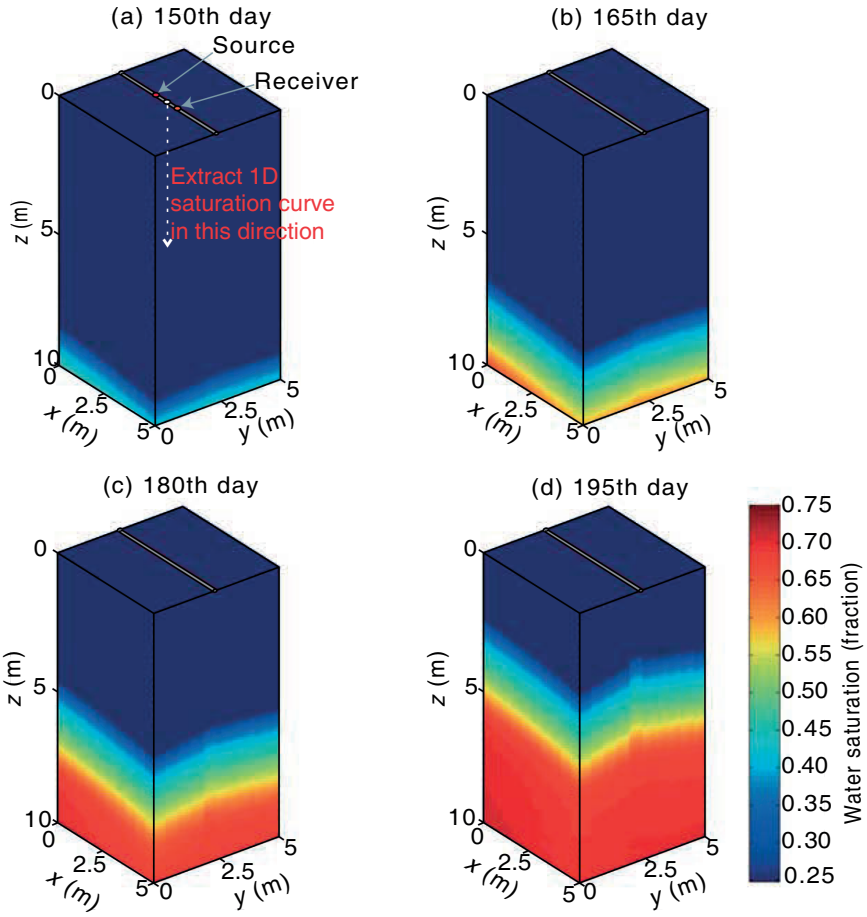

Figure 4.5: Snapshots of water saturation distributions in the extracted box volume on the 150th day (Figure 4.5a), 165th day (Figure 4.5b), 180th day (Figure 4.5c), and 195th day (Figure 4.5d) of production, respectively. The red part represents the invading water and the blue part the oil in-place.

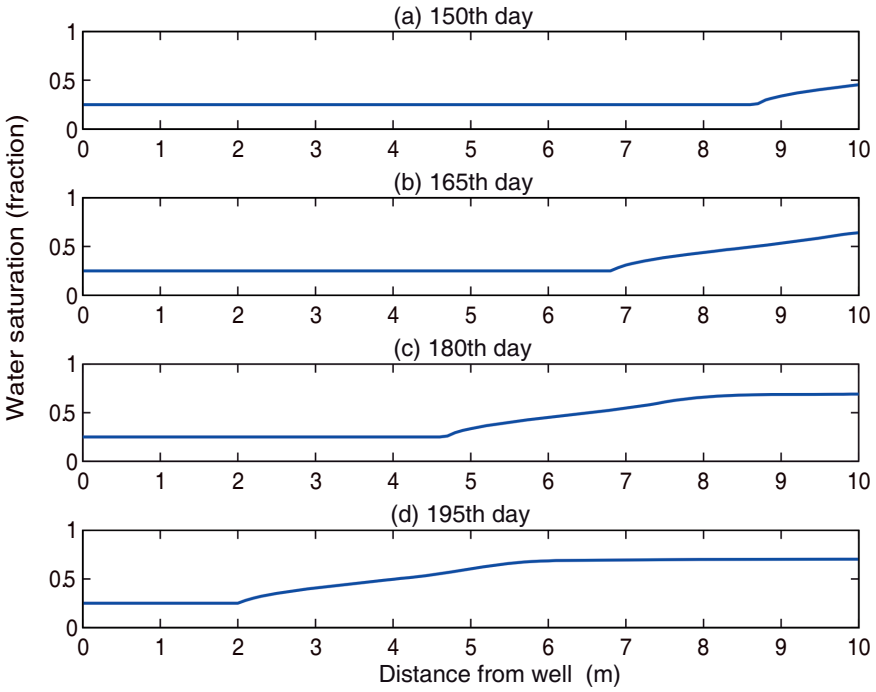

Figure 4.6: 1D water saturation curves extracted from the saturated volume in Figure 4.5. The curves demonstrate the water front moving towards the well after 150 days (Figure 4.6a), 165 days (Figure 4.6b), 180 days (Figure 4.6c), and 195 days (Figure 4.6d) of production, respectively.

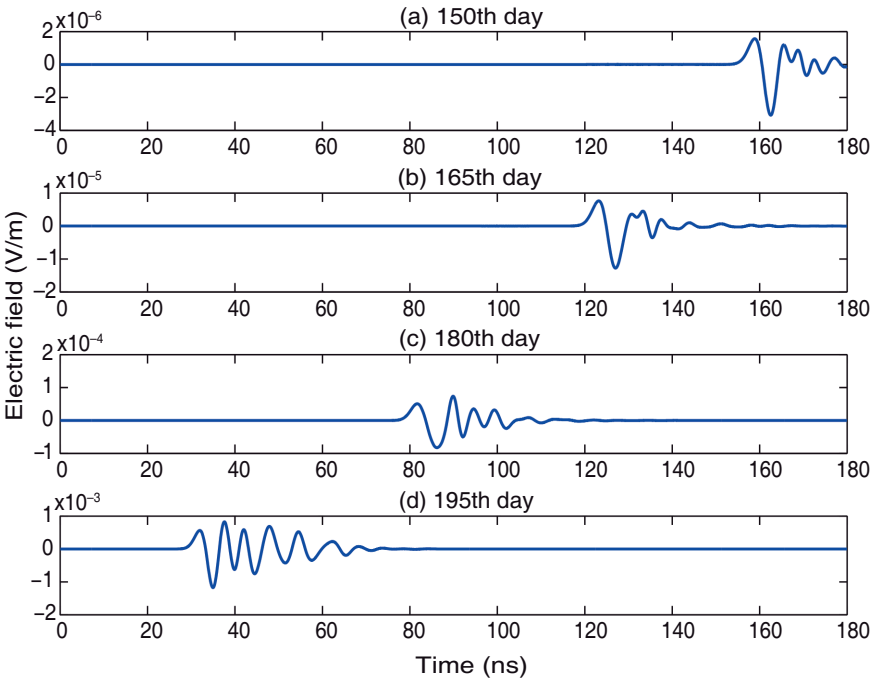

Figure 4.7: EM responses of 3D time-lapse GPR simulations on the 150th, 165th, 180th, and 195th day of oil production, respectively corresponding to the water front movement shown in Figure 4.6.

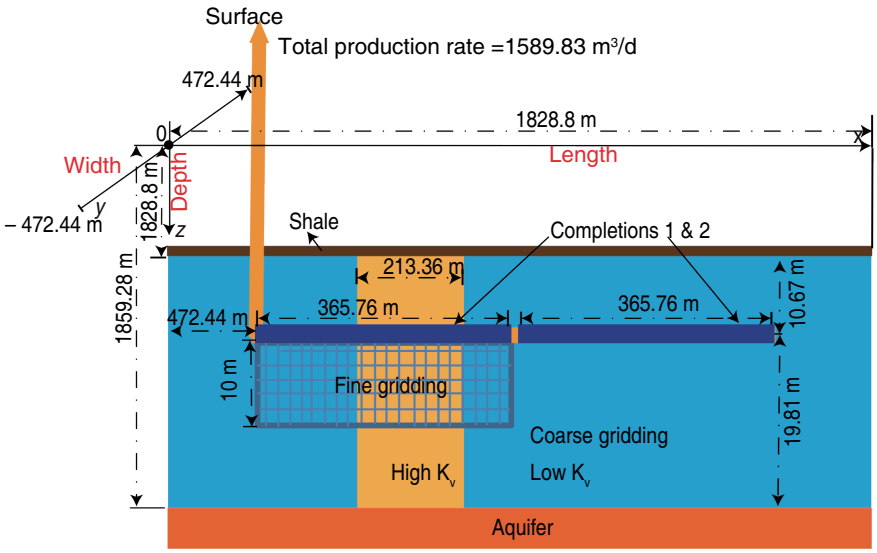

Figure 4.8: Parallel representation of the reservoir and well configurations of Model 2 [157].

Table 4.3: Reservoir and well properties for Model 2

Reservoir and well parameters		
Variables	Values	Units
Initial pressure at reference depth	24800	kPa
Horizontal permeability	0.50	Darcy
Vertical permeability (low)	0.01	Darcy
Vertical permeability (high)	0.50	Darcy
Porosity	0.25	fraction
Oil compressibility	2.10e-6	$(kPa)^{-1}$
Water compressibility	4.35e-7	$(kPa)^{-1}$
Water density	1000	kg/m^3
Oil density	800	kg/m^3
Water viscosity	5.00e-4	Pa·s
Oil viscosity	3.40e-4	Pa·s
Connate water saturation	0.25	fraction
Residual oil saturation	0.25	fraction
Water end-point relative permeability	0.80	fraction
Oil end-point relative permeability	0.80	fraction
Water Corey exponent	2.00	dimensionless
Oil Corey exponent	2.00	dimensionless
Aquifer strength	103.74e3	m^3/kPa
Aquifer compressibility	7.25e-7	$(kPa)^{-1}$
Aquifer characteristic time	10	year
Well radius	0.14	m
Surface Liquid rate	1589.83	m^3/d

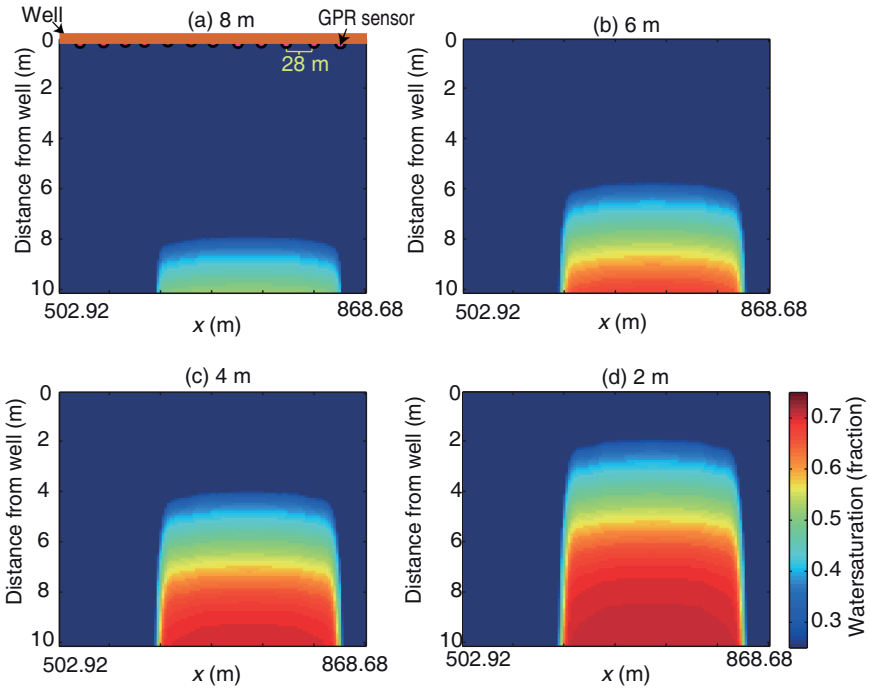

Figure 4.9: Snapshots of water saturations in the region of interest and GPR sensors (red dots) distributed along the well.

every individual receiver) are merged into a two-dimensional image. Note that densely allocated sensors present a high spatial resolution for reservoir imaging, but the number of distributed sensors should be financially weighted specific to field applications. In addition, a small separation distance between the sensors is possible to arouse an interference from the adjacent transmitters, but the time-lapse measurement can remove the undesired waves from the received signals. Figure 4.9 shows the snapshots of water saturation distributions in the region of interest when water front is 8 m, 6 m, 4 m, and 2 m away from the well, corresponding to time-lapse radar images presented in Figure 4.10. The contrasts between Figures 4.9 and 4.10 reveal that the temporal envelopes of the radar images agree well with the spatial distributions of the water front, and therefore the water front profiles are approximately reconstructed by the borehole radar array.

4.3.2. PRODUCTION STRATEGIES

Three production strategies, i.e., uncontrolled, reactive, and combined production strategies, are simulated. The simulations are confined in a production period of 10 years, which is the production lifetime of this reservoir scenario. The wellhead production rate is fixed at 1589.83 m^3/d. We assume no limitation on inflow capacity of each individual completion. The assumption excludes the constraint of minimum well

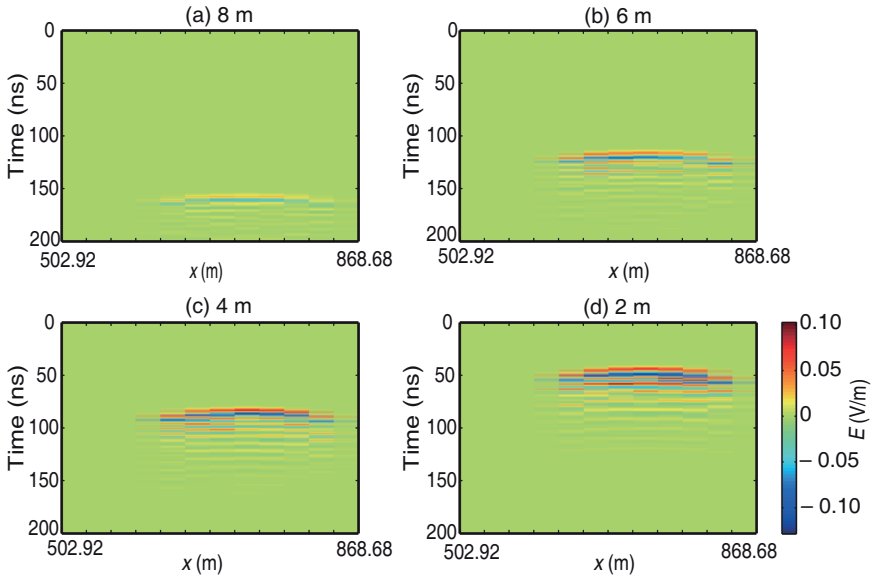

Figure 4.10: EM imaging results of time-lapse radar array measurements when water front is 8 m (Figure 4.9a), 6 m (Figure 4.9b), 4 m (Figure 4.9c), and 2 m (Figure 4.9d) away from the well.

bottom pressure, and allows for a broad range of ICV regulations.

In the production case of no monitoring and control, the inflow rate in the first completion is greater than the second one. Therefore, early breakthrough inevitably occurs, and oil production is hampered. The phenomenon is primarily caused by the high-permeability streak, as indicated in Figure 4.8. Additionally, higher pressure drawdown at the heel (the left of the well in Figure 4.8) than the toe (the right of the well in Figure 4.8), arising from wellbore friction, speeds up the influx of fluids into the first completion, which is called heel-toe effect [60].

Before water breakthrough, the reactive production has the same segment inflow rates as the uncontrolled one. After water breakthrough, we use an empirical algorithm of proportional reactive control to relieve water invading, as described by [160]:

$$\Pi_k = \mathrm{MIN}\left[\left(\frac{1-WCT_k}{1-WCT_{\min}}\right)^{\alpha}, 1\right], \tag{4.1}$$

where Π_k is the ICV choking coefficient for a given completion k, which is linked with the inflow rate of the corresponding completion, varying from 0, when ICV is fully closed, to 1, when ICV is fully open; WCT_k stands for the water cut reading inside a given completion k; $WCT_{\min}$ is the lowest water cut reading among the completions; α is a constant factor specific to a production case, which reflects the nonlinear correlations between the ICV choking speed and the difference of water cut readings among every completion. A strong nonlinearity signifies that the ICVs can be rapidly choked to maintain a rela-

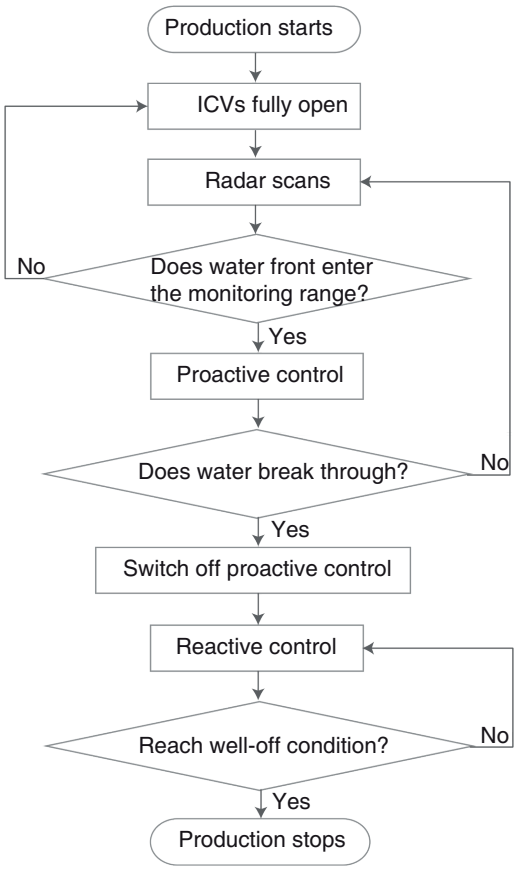

Figure 4.11: Flow diagram of the combined production strategy.

tively small difference of water cut readings among the segments. α is defined as 10 here.

In the third production strategy, we add the proactive control to the proportional reactive control, expecting to bring their advantages together for more benefits. In addition to multiphase flow meters, the well requires to be equipped with reservoir monitoring tools, which can be supported by our borehole radar imaging technology. The overall work flow of production and control is clarified in Figure 4.11. In the initial period of production, both ICVs are fully open; after water approaches the detection range of borehole radars, proactive control is activated, and a feedback control is conducted by linking ICV choking with radar imaging data; after water breaks through the well, proactive control is terminated, and proportional reactive control is initiated until the well is shut.

In the stage of proactive control, we set the period of monitoring and control as 7 days. Every 7 days, radar array implements a set of scanning to capture the profile of fluid flow,

and then a control decision is made for ICV choking or maintaining. A simple proactive control algorithm is proposed in this study, as described by:

$$\Pi_k^t = \begin{cases} \beta {\Pi_k}^{t-1}, & (\text{if } |D_k - D_{\max}| > D_{\text{th}}) \\ \Pi_k^{t-1}, & (\text{if } |D_k - D_{\max}| < D_{\text{th}}) \\ 1, & (\text{if } |D_k - D_{\max}| = 0) \end{cases} \tag{4.2}$$

where Π_k^t and Π_k^{t-1} represent the choking coefficients of the kth completion in the current and previous periods of monitoring and control, respectively; β is the discount factor, reflecting the choking extent of ICVs relative to the previous period, and is set as 0.5 in this study; D_k denotes the distance between the kth completion and its corresponding leading displacement edge, and it can be obtained by searching the minimum travel time of reflected waves in the corresponding radar trace gather; $D_{\max}$ is the maximum value among all the D_ks, which corresponds to the slowest flow zone; and D_{th} is the threshold that links the distance difference of water front to the proactive action, reflecting the tolerance extent of proactive controls to the unevenness of water front profile, and it is set as 1 m in this case. For a dual-completion smart well production, the procedure of proactive control by this formula is described as follows: (1) after water invades the monitoring range (i.e., 10 m away from the well), proactive control is started; (2) if the water front in one completion zone moves above 1 m ahead of that in the other, the corresponding ICV is choked back at a discount factor of 0.5 to reduce its ICV inflow, and meanwhile the other completion keeps its ICV fully open; (3) if the distance difference of the water front in the two zones is within 1 m, both completions maintain their ICVs unchanged until the next period. The basic principle of the proactive control algorithm is to slow down the production in the faster flowing zone while speed up the production in the slower one, in order to gradually flatten the water front profile. Although we adopt a well with two completions in this scenario, the algorithm is also expected to suit for multi-segment smart well systems.

Figure 4.12 records the wellhead production rates of oil and water by the three production strategies. For the conventional and reactive production strategies, there is a water-free production period of 84 days. Afterwards, water breaks through the well, and the wellhead oil production rate is decreased while water production rate is increased. However, after water breakthrough, the reactive production strategy still maintains higher oil production rate and lower water production rate than the conventional well production for a long period. The combined production strategy delays water breakthrough time for 213 days relative to the reactive production, thereby keeping a water-free production period of approximately 10 months. After the combined production encounters water breakthrough, it holds similar oil and water production rates as the reactive production because of the subsequent reactive behavior.

Figures 4.13 and 4.14 respectively show the inflow rates and water front distances of each completion by the combined production strategy. After water approaches the monitoring range, the proactive control decreases the flow rate of Completion 1 until it is close to zero, while the flow rate of Completion 2 increases due to the constant

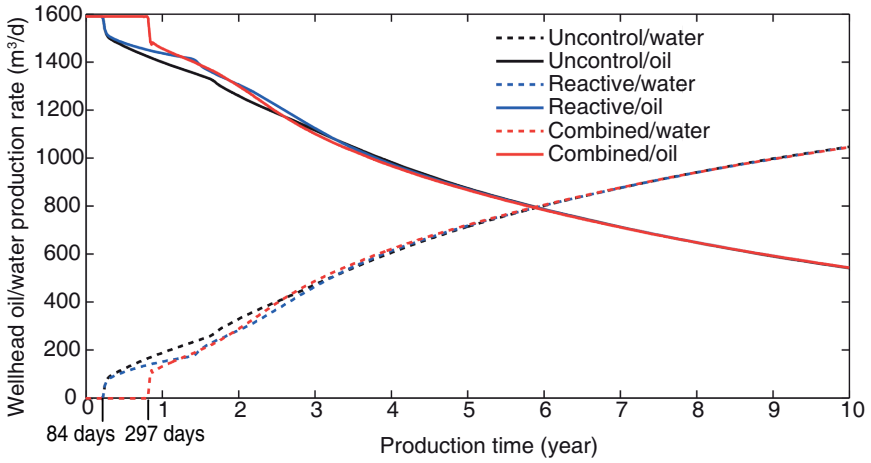

Figure 4.12: Wellhead production rates of water and oil for the three production strategies.

wellhead liquid rate (Figure 4.13). In this stage, water front movement in Completion 1 zone is slowed down until it is caught up with by the moving water front in Completion 2 zone (Figure 4.14). The effects of the proactive control can be summarized as follows: (1) balancing inflow rates of each completion and flattening water front profile, (2) delaying water breakthrough, (3) improving sweep efficiency. Figure 4.15 presents the snapshots of saturation distributions after 270 days of production by the reactive and combined production strategies, respectively. We can see that, after water breakthrough has occurred in the reactive production strategy, water is still far away from the well in the combined production strategy. The obvious delay of water breakthrough is attributed to proactive control behaviors.

Table 4.4 sums up the cumulative productions of water and oil by the three production strategies and their relative improvement percentages. Data are recorded and compared in the production periods of 1 year, 5 years, and 10 years, respectively, implying a short-term, mid-term, and long-term optimization effects. Compared with the conventional well production, the reactive production strategy and the combined production strategy both improve cumulative oil production and decrease cumulative water production in every production period. Relative to the reactive production strategy, the combined production strategy further decreases cumulative water production by 66.89%, 1.75%, and 0.45%, and increases cumulative oil production by 4.76%, 0.57%, and 0.31%, respectively in the production periods of 1 year, 5 years, and 10 years. The quantitative comparisons reveal that, the combined production strategy is superior to the reactive production in accelerating oil production and suppressing water production, and its advantages are more remarkable in the early stage of production because proactive control delays water breakthrough with the help of borehole radar monitoring.

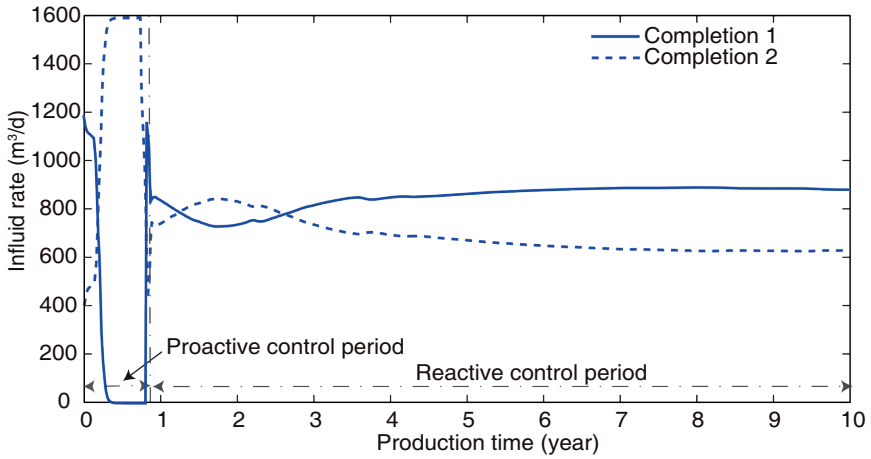

Figure 4.13: Liquid inflow rates of each completion for the combined production strategy.

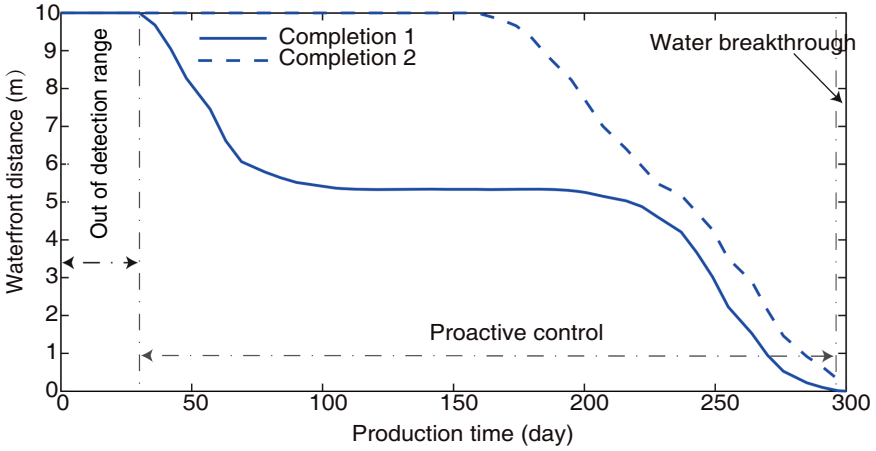

Figure 4.14: Water front distance from the well in each completion zone before water breakthrough.

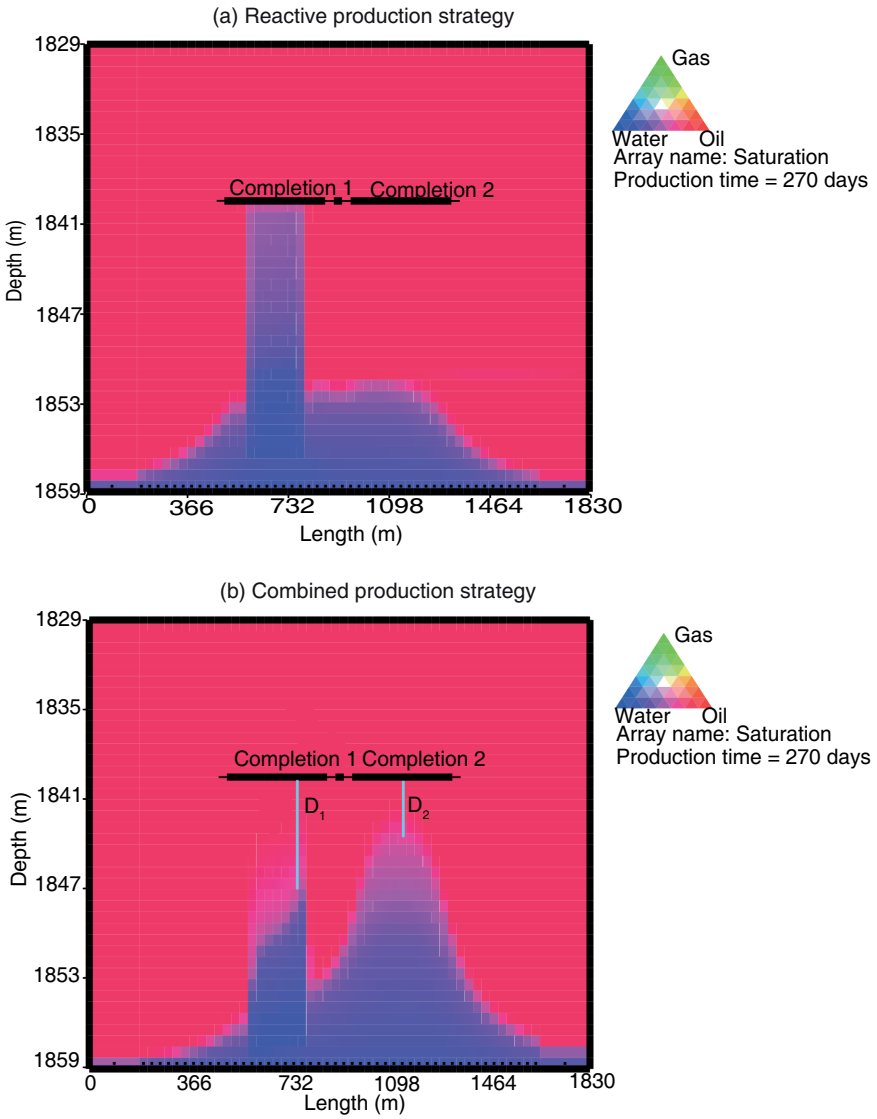

Figure 4.15: Snapshots of saturation distributions after 270 days of production for the reactive (Figures 4.15a) and combined (Figures 4.15b) production strategies simulated by MoRes. D_1 and D_2 represent the distances of displacement front away from Completion 1 and Completion 2, respectively.

Table 4.4: Cumulative production data and relative improvements for the three production strategies

Production data			
Data recorded	**Uncontrolled**	**Reactive**	**Combined**
Production for 1 year			
Cumulative water production	3.8563×10^4 m^3	3.3200×10^4 m^3	7.4025×10^3 m^3
Decrease of water production	–	13.91%	80.80%
Cumulative oil production	5.4178×10^5 m^3	5.4714×10^5 m^3	5.7294×10^5 m^3
Increase of oil production	–	0.99%	5.75%
Production for 5 years			
Cumulative water production	7.1852×10^5 m^3	6.8901×10^5 m^3	6.7645×10^5 m^3
Decrease of water production	–	4.11%	5.86%
Cumulative oil production	2.1849×10^6 m^3	2.2145×10^6 m^3	2.2269×10^6 m^3
Increase of oil production	–	1.35%	1.92%
Production for 10 years			
Cumulative water production	2.3639×10^6 m^3	2.3340×10^6 m^3	2.3234×10^6 m^3
Decrease of water production	–	1.26%	1.71%
Cumulative oil production	3.4429×10^6 m^3	3.4728×10^6 m^3	3.4835×10^6 m^3
Increase of oil production	–	0.87%	1.18%

4.4. CONCLUSIONS

In this chapter, we establish an integrated three-dimensional numerical model coupling EM propagation and multiphase fluid flow, and investigate the potentials of borehole radar for reservoir monitoring in a smart well production environment. A box-scale simulation indicates that the reflected signals extracted from a time-lapse borehole radar measurement has a good correspondence with the evolution of the oil-water displacement front. Therefore, we conclude that borehole radar has a capability of detecting the changes of water and oil distributions in the near-well region of a production well. EM imaging simulations show that borehole radar array data can be used to reconstruct the profile of water front in a bottom-water drive reservoir. We propose that a borehole radar array can be an effective downhole imaging tool to capture the comprehensive information of fluid dynamics in a produced reservoir.

Based on imaging data fed back from radar array, a proactive control approach is conducted to regulate completion inflow rates in a smart well production environment. The control scheme successfully delays water breakthrough time, and extends water-free production period. To demonstrate the practical advantages of borehole radar for oil industries, we simulate three production strategies in a thin oil reservoir produced by a horizontal well. The comparisons of production data in different production stages imply that the production strategy combining the reactive and proactive controls, which is supported by our borehole radar monitoring, can accelerate oil production and suppress water production, and that the superiority resides in short-term rather than long-term optimizations. The increase of cumulative oil will make more profits, whereas the decrease of cumulative water can save costs of water handling. Especially,

the noticeable improvement in the early production stage can accelerate the return of investment, showing economic attractiveness for the oil industry.

We suggest that borehole radar is a promising downhole sensor for reservoir monitoring, and it has potential to improve recovery efficiency if combined with a proper production control strategy. The ideal application environments are thin oil reservoirs produced with the bottom-water drive. Further studies should be carried out on the selection of the reservoir types where borehole radar monitoring can make effects, and more advanced smart well control algorithms are to be developed to gain more benefits. For field applications, antenna design and hardware manufacture are vital.

5

CONCLUSIONS

This chapter summarizes our contributions and draws conclusions. It also highlights possible future research directions. The summary and conclusions are presented in Section 5.1, after which future work is discussed in Section 5.2.

5.1. SUMMARY

This thesis investigates the potential applications of GPR in deep oil wells in the phases of exploration and production. The study is carried out in a numerical way with a coupled EM and fluid flow modelling.

In oil exploration, GPR is applied in well logging for reservoir estimation purpose. GPR antennas are designed in a wireline logging tool to detect the invaded mud front in the near-borehole regions. To measure the mud-contaminated regions in the range of few decimeters to approximately 1 meter away from the borehole wall and in the spatial resolution of a few centimeters, a Ricker wavelet with the center frequency of 1 GHz is employed for the antenna excitation. The radar antennas are designed to be installed in a backward cavity of a logging string to conduct downhole directional measurements. The antenna cavities are suggested to be made as large as possible to diminish the ringing effects and acquire high-quality signals. The waves reflected from the invasion front can be extracted from the received signals by a time-lapse logging because it can remove the majority of EM clutters from the non-uniform flushed zone and inhomogeneous rock and obtain relatively clean signals. The logging time intervals of the time-lapse measurements are recommended to be at least 6 hours to achieve an intact reflected waves. Systematic analyses of parametric sensitivity study how the fluids and formation properties influence the shape of the invasion profile and thereby influence the extraction of the signals reflected from the invasion front. The analyses reveal that the reflection signals from the mud invasion front are sensitive to oil viscosity, porosity, mud and formation water salinity, and salt diffusion coefficient, and they should be paid much attention to before the novel logging method is applied to a certain reservoir. Obtaining reflection signals of the invasion front, a radar configuration mode with one source and two receivers is proposed to derive the mud invasion depth from the travel times of the reflected waves. The simulations suggest that the borehole radar can be applied to well logging to detect mud invasion and estimate the invasion depth. Through the obtained mud invasion information using borehole radar, a new reservoir assessment method is proposed to estimate reservoir permeability. The method is based on the previous study that the mud invasion depth is greatly influenced by the formation petrophysical properties. The ideal reservoir scenarios are fresh water-based mud invading low-porosity and low-permeability oil-bearing layers. A four-dimensional interpretation chart is established to relate the invasion depth with initial water saturation, porosity and permeability. The results show a good agreement between the preset and estimated permeability curve. The study suggests that borehole radar has potentials of solving permeability estimation problem.

In oil production, GPR is proposed to be applied in production monitoring. Currently, the investigated application environment is a thin oil rim reservoir produced with a horizontal well under bottom water drive. In this kind of application environments, a monitoring range of 10 meters is required, for which a GPR with a center frequency of 100 MHz is recommended. The antennas are assumed to be installed along the casing of a production well to transmit and receive EM waves towards and from the reservoirs. A box-scale simulation reveals that time-lapse measurements can detect the water front

reflection signals within the range of 10 m, and the evolution of the travel times of the reflected waves corresponds well with the advancement of the water-oil displacement. A reservoir-scale model simulates that an array of radar sensors, permanently installed in the production well, monitors water front movement. The results show that the array borehole radars can be used to successfully reconstruct the water front profile in a heterogeneous reservoir. The study suggests that borehole radar can be an effective downhole monitoring tool to provide the dynamic fluid flow information in a produced reservoir. To assess the economic attraction to the oil industry, a comparative study is conducted to quantitatively assess the added values of smart well production combined with the borehole radar imaging data. The proposed feedback control algorithm, which is supported by borehole radar monitoring, successfully delays water breakthrough. It accelerates oil production and suppresses water production. The cumulative oil production is increased while the cumulative water production is decreased, and the superiority resides in the early stage of the production life, which is beneficial for the recycle of the investment.

The two scenarios demonstrate the potential applications of GPR in deep oil reservoirs. The thesis not only demonstrates the capability of borehole radar for specific solutions, but also proposes effective application methodologies in an industrial setting, therefore exhibiting promising prospects of borehole radar applications in the oil industry. The inspired recommendations greatly extend the application fields of GPR, and we expect that the oil industry will be the next hot spots of GPR applications.

5.2. FUTURE WORK

In this section, we discuss the future work. Here, we list a number of possible recommendations to extend the work of this thesis into new directions.

Even though theoretical studies demonstrate that borehole radar has great potentials in deep hydrocarbon reservoir applications, challenges to realize these potentials remain mainly in the technological feasibility. A sophisticated design of borehole radar antennas and the accessorial parts that work in the special downhole environments should be addressed, which involves the disciplines of electrical engineering, mechanical engineering, and drilling engineering. Although there has been a borehole radar logging prototype developed [108], no such kinds of tools are developed for the application scenarios in this thesis.

Following the study examples in this thesis, more application scenarios are to be explored to extend the values of borehole radars in oil exploration and production fields.

Quantitatively estimating the permeability magnitude varying with depth, an inspiration is to quantify the anisotropy of the permeability in a reservoir. Permeability anisotropy plays significant roles in oil recovery schemes. Relative to the permeability magnitude, anisotropy is more difficult to estimate through porosity information. However, in the case that a thin oil rim reservoir is drilled with a horizontal trajectory,

the invaded mud tends to present an ellipse-like annulus centered by the borehole. This is caused by the permeability anisotropy because normally the vertical permeability is much smaller than the horizonal one. The asymmetric degree of the shape of the invasion front must have close correlations with the tensor of the permeability. Once a directional borehole radar can image the shape of the mud invasion across the wellbore, it is possible to infer or invert the permeability anisotropy. The current configurations of borehole radar logging in this thesis are ready to be converted for this application. Nevertheless, the challenges could reside in the inversion algorithm, which is complicated by the mud cake effects.

Hydraulic fracturing is a technique to inject high pressure into a wellbore to create cracks in the deep formations for an easy recovery in shale gas or tight oil/gas reservoirs [161]. To monitor the fracture network and assess the fracturing effects, borehole radar can play a part and even could be the tool with the highest spatial resolution compared with any other geophysical method. It is worthy of studying the usage of borehole radar in fracturing assessments. In this application, direct wave instead of reflection wave should be extracted.

In the oil recovery phase, the current focus is the unconventional oil production, among which heavy oil reservoirs have a large proportion [162]. This attracts our attentions to the SAGD and BWS productions using borehole radar monitoring. In analogy with the borehole radar monitoring in the thin oil rim productions, SAGD and BWS monitoring have the similar requirements of monitoring range. However, their fluid properties have large differences with the conventional oil reservoirs, which means the effects of petrophysical properties on radar responses should be specially investigated. In addition, well control strategies in the two production scenarios should be studied and the added values should be quantitatively compared with the conventional well production.

Appendices

A

MATHEMATICAL EXPRESSIONS OF MUD INVASION

A.1. MULTIPHASE AND MULTICOMPONENT FORMULAS

The mud invasion process can be described by multiphase and multicomponent flow issues. The two-phase flow equations of oil and water describe the pressure and saturation changes over the time based on the isothermal Darcy flow theory [114]:

$$\nabla \cdot [\frac{\rho_w k k_{rw}}{\mu_w}(\nabla P_w - \rho_w \mathbf{g} \nabla h)] = \frac{\partial(\phi \rho_w S_w)}{\partial t}, \tag{A.1}$$

$$\nabla \cdot [\frac{\rho_o k k_{ro}}{\mu_o}(\nabla P_o - \rho_o \mathbf{g} \nabla h)] = \frac{\partial(\phi \rho_o S_o)}{\partial t}, \tag{A.2}$$

$$P_c(S_w) = P_o - P_w, \tag{A.3}$$

$$S_o = 1 - S_w, \tag{A.4}$$

where ρ_w and ρ_o are the densities of water and oil (kg/m^3), respectively, k is the reservoir permeability (m^2), k_{rw} and k_{ro} are the relative permeabilities of water and oil (dimensionless), respectively, $\mathbf{g}$ is the gravity acceleration vector (m/s^2), h is the depth (m), μ_o and μ_w are the viscosities of water and oil (Pa·s), respectively, P_w and P_o are the pressures of water and oil (Pa), respectively, ϕ is the porosity (fraction), S_w and S_o are the saturations of water and oil (fraction), t is the invasion time (s), and P_c is the capillary pressure (Pa).

The relative permeabilities and capillary pressure are the functions of water saturation,

A

and can be described with the analytical expressions as below [163]:

$$k_{rw} = k^0_{rw}(\frac{S_w - S_{wc}}{1 - S_{wc} - S_{or}})^{e_w}, \tag{A.5}$$

$$k_{ro} = k^0_{ro}(1 - \frac{S_w - S_{wc}}{1 - S_{wc} - S_{or}})^{e_o}, \tag{A.6}$$

$$P_c = P^0_c\sqrt{\frac{\phi}{k}}(1 - \frac{S_w - S_{wc}}{1 - S_{wc} - S_{or}})^{e_p}, \tag{A.7}$$

where k^0_{rw} and k^0_{ro} are respectively the end-point relative permeabilities of water and oil phases (dimensionless), S_{wc} and S_{or} are respectively the connate water and irreducible oil saturations (fraction), e_w and e_o are respectively the empirical exponents for water and oil (dimensionless), P^0_c is the coefficient of the capillary pressure (Pa·cm), and e_p is the pore-size distribution empirical exponent (dimensionless).

The multicomponent flow issue describes the miscibility of the water with different salt concentrations, and can be expressed by the convection-diffusion equation [116]:

$$\nabla\cdot[\frac{\rho_w k k_{rw} C_w}{\mu_w}(\nabla P_w - \rho_w \mathbf{g}\nabla h)] + \nabla\cdot(\rho_w \phi S_w K_D \nabla C_w) = \frac{\partial(\phi\rho_w S_w C_w)}{\partial t}, \tag{A.8}$$

where C_w is the water salinity (ppm), and K_D is the dispersion coefficient that includes the effects of molecular diffusion and hydrodynamic dispersion (m^2/s), which is expressed by

$$K_D = D + \frac{\alpha_L}{\phi S_w}\frac{k k_{rw}}{\mu_w}\nabla P_w, \tag{A.9}$$

where D is the molecular diffusion coefficient (m^2/s), and α_L is the dispersivity (m). The first term in the left part of equation A.8 stands for the salinity changed by the convective transport of water, and the second term represents the salinity variation due to the salt concentration difference.

With finite-difference time-domain method, the equations above are discretized in a cylindrical coordinate systems, and the radial distributions of the fluid pressure, saturation, and salinity over invasion time are obtained.

A.2. ROCK ELECTRICAL FORMULAS

To convert the fluid properties to the electrical properties, some empirical formulas for the electrical mixture of geo-materials are used.

Archie's law is a good approximation to calculate the bulk electrical conductivity in the presentation of saturated sandstone [164]:

$$\sigma = \frac{\sigma_w \phi^m S_w^n}{\alpha}, \tag{A.10}$$

where σ and σ_w denote the bulk conductivity of the saturated rock and formation water conductivity (S/m), respectively; m, n and α are the cementation, saturation exponents and tortuosity factor (dimensionless), respectively, which are empirical constants measured on core samples. The formation water conductivity σ_w is calculated as a function of temperature and salinity, as described by [165]:

$$\sigma_w = [(0.0123 + \frac{3647.5}{C_w^{0.995}})\frac{82}{1.8T+39}]^{-1}, \tag{A.11}$$

where C_w and T denote the formation salinity (ppm) and temperature (^oC).

The bulk permittivity is calculated with the permittivities of the dry rock matrix, water, and oil and their respective volume fractions through the complex refractive index model (CRIM) [166]:

$$\sqrt{\varepsilon} = \sqrt{\varepsilon_m}(1-\phi) + \sqrt{\varepsilon_o}(\phi - \phi S_w) + \sqrt{\varepsilon_w}\phi S_w, \tag{A.12}$$

where ε, ε_m, ε_o, and ε_w denotes the bulk permittivity (dimensionless) of the saturated rock, dry rock matrix permittivity, oil permittivity and water permittivity, respectively. Water permittivity is modified in the deep reservoir conditions because it is prominently influenced by the temperature and salinity. A polynomial interpolation function, based on the laboratory measurement data [124], links the salinity variation with the relative permittivity of water at the temperature of 93.2 °C, as expressed by

$$\varepsilon_w = 57.93 - 4.417\times10^{-16}C_w^3 + 4.266\times10^{-10}C_w^2 - 1.443\times10^{-4}C_w, \tag{A.13}$$

A.3. FORMULAS OF MUD CAKE GROWTH

The changes of the permeability and porosity of the mud cake over the invasion time are influenced by the pressure drop across the mud cake, as described by [43]

$$k_{mc}(t) = \frac{k_{mc0}}{P_{mc}^{\nu}(t)}, \tag{A.14}$$

$$\phi_{mc}(t) = \frac{\phi_{mc0}}{P_{mc}^{\delta\cdot\nu}(t)}, \tag{A.15}$$

where k_{mc} and ϕ_{mc} are the mud cake permeability and porosity, respectively; P_{mc} is the pressure drop across the mud cake; k_{mc0} and ϕ_{mc0} are the referenced permeability and porosity of the mud cake, respectively, defined by the measurement under the pressure difference of 6.9 kPa; and ν and δ are dimensionless compressibility exponent and multiplier reflecting the relationship between the permeability and porosity of the compressed mud cake, which are measured in the laboratory.

The instantaneous invasion rate of mud filtrate is given by [43]

$$q_{mc}(t) = \frac{2\pi h\left[P_m - P_{w,N}(t)\right]}{\sum_{i=2}^{N-1}\frac{\ln(r_{i+1})-\ln(r_i)}{\left(\frac{kk_{ro}}{u_o}\right)_i\left(\frac{P_{c,i}(t)-P_{c,i+1}(t)}{P_{w,i}(t)-P_{w,i+1}(t)}\right)+\left(\frac{kk_{ro}}{\mu_o}+\frac{kk_{rw}}{\mu_w}\right)_i} + \frac{\mu_{mc}}{k_{mc}(t)}\ln\left(\frac{r_w}{r_{mc}(t)}\right)}, \tag{A.16}$$

A

where q_{mc} is the instantaneous invasion rate (m^3/s), h is the objective layer thickness (m), P_m is the downhole mud pressure (Pa), μ_{mc} is the mud filtrate viscosity (Pa·s), r_w is the radius of the wellbore (m), r_{mc} is the inner radius of the mud cake annulus (m), and the remaining variables and their units are the same to those defined in Append A.1. Note that the subscript i implies the serial number of the grids after the flow model is discretized, where i=1 denotes the grid of the mud cake, and i=N stands for the grid of radial outer boundary of the modelled domain. The first and second terms in the denominator of equation A.16 denote the flow resistivities of the formation and the mud cake, respectively.

The growth of the mud cake thickness over time (i.e., the decreasing r_{mc} in equation A.16 can be expressed by [43]

$$\frac{dr_{mc}(t)}{dt} = -\frac{f_s}{(1-f_s)[1-\phi_{mc}(t)]} \cdot \frac{q_{mc}(t)}{2\pi\Delta h \cdot r_{mc}(t)}, \tag{A.17}$$

where f_s is the percentage by volume (fraction) of the solid particles contained in the mud.

REFERENCES

[1] E. Slob, M. Sato, and G. Olhoeft, Surface and borehole ground-penetrating-radar developments, *Geophysics*, vol. 75, no. 5, pp. 75A103–75A120, 2010.

[2] D. Daniels, Ed. *Ground Penetrating Radar*, 2nd ed., London, UK: Institution of Engineering and Technology, 2004.

[3] H. Jol, Ed. *Ground Penetrating Radar: Theory and Applications*, Amsterdam, The Netherlands: Elsevier Science, 2009.

[4] D. McCann, P. Jackson, and P. Fenning, Comparison of the seismic and ground probing radar methods in geological surveying, *Communications, Radar and Signal Processing, IEE Proceedings F*, vol. 135, no. 4, pp. 380–391, 1988.

[5] M. Ercoli, C. Pauselli, A. Frigeri, E. Forte, and C. Federico, Geophysical paleoseismology through high resolution GPR data: A case of shallow faulting imaging in Central Italy, *Journal of Applied Geophysics*, vol. 90, pp. 27–40, 2013.

[6] S. Malagodi, L. Orlando, S. Piro, and F. Rosso, Location of archaeological structures using GPR method: Three dimensional data acquisition and radar signal processing, *Archaeological Prospection*, vol. 3, no. 1, pp. 13–23, 1996.

[7] W. Zhao, E. Forte, S. T. Levi, M. Pipan, and G. Tian, Improved high-resolution GPR imaging and characterization of prehistoric archaeological features by means of attribute analysis, *Journal of Archaeological Science*, vol. 54, pp. 77–85, 2015.

[8] F. Prego, M. Solla, I. Puente, and P. Arias, Efficient GPR data acquisition to detect underground pipes, *NDT & E International*, vol. 91, pp. 22–31, 2017.

[9] N. Šarlah, T. Podobnikar, T. Ambrožič, and B. Mušič, Application of Kinematic GPR-TPS model with high 3D georeference accuracy for underground utility infrastructure mapping: A case study from urban sites in Celje, Slovenia, *Remote Sensing*, vol. 12, no. 8, pp. 1228, 2020.

[10] K. Grote, S. Hubbard, J. Harvey, and Y. Rubin, Evaluation of infiltration in layered pavements using surface GPR reflection techniques, *Journal of Applied Geophysics*, vol. 57, no. 2, pp. 129–153, 2005.

[11] H. Liu, Z. Deng, F. Han, Y. Xia, Q. Liu, and M. Sato, Time-frequency analysis of air-coupled GPR data for identification of delamination between pavement layers, *Construction and Building Materials*, vol. 154, no. 15, pp. 1207–1215, 2017.

[12] W. S. Hammon, G. A. McMechan, and X. Zeng, Forensic GPR: Finite-difference simulations of responses from buried human remains, *Journal of Applied Geophysics*, vol. 45, no. 3, pp. 171–186, 2000.

[13] E. R. Almeida, J. L. Porsani, I. Catapano, G. Gennarelli, and F. Soldovieri, Microwave tomography-enhanced GPR in forensic surveys: The case study of a tropical environment, *IEEE Journal of Selected Topics in Applied Earth Observations and Remote Sensing*, vol. 9, no. 1, pp. 115–124, 2016.

[14] T. G. Savelyev, L. V. Kempen, H. Sahli, J. Sachs, and M. Sato, Investigation of time–frequency features for GPR landmine discrimination, *IEEE Transactions on Geoscience and Remote Sensing*, vol. 45, pp. 118–129, 2007.

[15] A. Yarovoy, Landmine and unexploded ordnance detection and classification with ground penetrating radar, in *Ground Penetrating Radar Theory and Applications*, H. M. Jol, Ed. Amsterdam: Elsevier, 2009, pp. 445–478.

[16] L. Xiao, P. Zhu, G. Fang, Z. Xiao, Y. Zou, J. Zhao, N. Zhao, Y. Yuan, L. Qiao, X. Zhang, H. Zhang, J. Wang, J. Huang, Q. Huang, Q. He, B. Zhou, Y. Ji, Q. Zhang, S. Shen, Y. Li, and Y. Gao, A young multilayered terrane of the northern mare imbrium revealed by Chang'e-3 mission, *Science*, vol. 347, no. 6227, pp. 1226–1229, 2015.

[17] C. Li, S. Xing, S. E. Lauro, Y. Su, S. Dai, J. Feng, B. Cosciotti, F. Di Paolo, E. Mattei, Y. Xiao, C. Ding, and E. Pettinelli, Pitfalls in GPR data interpretation: False reflectors detected in lunar radar cross sections by Chang'e-3, *IEEE Transactions on Geoscience and Remote Sensing*, vol. 56, no. 3, pp. 1325–1335, 2017.

[18] B. Sun, M. Siegert, S. Mudd, D. Sugden, S. Fujita, X. Cui, Y. Jiang, X. Tang, and Y. Li, The Gamburtsev mountains and the origin and early evolution of the Antarctic Ice Sheet, *Nature*, vol. 459, pp. 690–693, 2009.

[19] K. Lamsters, J. Karušs, A. Rečs, and D. Bērziņš, Detailed subglacial topography and drumlins at the marginal zone of Múlajökull outlet glacier, central Iceland: Evidence from low frequency GPR data, *Polar Science*, vol. 10, no. 4, pp. 470–475, 2016.

[20] P. K. Fullagar, D. W. Livelybrooks, P. Zhang, A. J. Calvert, and Y. Wu, Radio tomography and borehole radar delineation of the McConnell nickel sulfide deposit, Sudbury, Ontario, Canada, *Geophysics*, vol. 65, no. 6, pp. 1920–1930, 2000.

[21] J. Tronicke and G. Hamann, Vertical radar profiling: Combined analysis of traveltimes, amplitudes, and reflections, *Geophysics*, vol. 79, no. 4, pp. H23–H35, 2014.

[22] H. Zhou and M. Sato, Subsurface cavity imaging by crosshole borehole radar measurements, *IEEE Transactions on Geoscience and Remote Sensing*, vol. 42, no. 2, pp. 335–341, 2004.

[23] H. Jang, S. Kuroda, and H. J. Kim, Efficient electromagnetic imaging of an artificial infiltration process in the vadose zone using cross-borehole radar, *IEEE Geoscience and Remote Sensing Letters*, vol. 8, no. 2, pp. 243–247, 2011.

[24] W. T. Holser, R. J. S. Brown, F. A. Roberts, O. A. Fredriksson, and R. R Unterberger, Radar logging of a salt dome, *Geophysics*, vol. 37, no. 5, pp. 889–906, 1972.

[25] H. Nickel, F. Sender, R. Thierbach, and H. Weichart, Exploring the interior of salt domes of salt domes from boreholes, *Geophysical Prospecting*, vol. 31, no. 1, pp. 131–148, 1983.

[26] C. Fairhurst, F. Gera, P. Gnirk, M. Gray, and B. Stillborg, The international stripa project: An overview, *Tunnelling and Underground Space Technology*, vol. 8, no. 3, pp. 315–343, 1993.

[27] O. Olsson, L. Falk, E. Sandberg, O. Forslund, and L. Lundmark, Radar measurements with a directional borehole antenna, in *SEG Annual Meeting*, Dallas, Texas, USA, 1989, pp. 222–225.

[28] K. W. A. van Dongen, R. van Waard, S. van der Baan, P. M. van den Berg, and J. T. Fokkema, A directional borehole radar system, *Sensing and Imaging*, vol. 3, no. 4, pp. 327–346, 2002.

[29] R. van Waard, S. van der Baan, and K. W. A. van Dongen, Experimental data of a directional borehole radar system for UXO detection, in Tenth International Conference on Ground Penetrating Radar, Delft, The Netherlands, 2004, pp. 225–228.

[30] D. L. Wright, J. D. Abraham, D. V. Smith, and S. R. Hutton, A high-resolution, short-range, directional borehole radar, in *Symposium on the Application of Geophysics to Engineering and Environmental Problems*, Denver, Colorado, USA, 2001, pp. 192–207.

[31] P. D. Pisani and D. Vogt, Borehole radar delineation of the Ventersdorp Contact Reef in three dimensions, *Exploration Geophysics*, vol. 35, no. 4, pp. 319–323, 2004.

[32] I. M. Mason, A. J. Bray, T. G. Sindle, C. M. Simmat, and J. H. Cloete, The effect of conduction on VHF radar images shot in water-filled boreholes, *IEEE Geoscience and Remote Sensing Letters*, vol. 5, no. 2, pp. 304–307, 2008.

[33] B. Zhou and M. van de Werken, Conductively guided borehole radar wave for imaging ahead of a drill bit, *IEEE Geoscience and Remote Sensing Letters*, vol. 12, pp. 1–5, 2015.

[34] L. Mao and B. Zhou, Simulation and analysis of conductively guided borehole radar wave, *IEEE Transactions on Geoscience and Remote Sensing*, vol. 55, no. 5, pp. 2646–2657, 2017.

[35] J. Zhao and M. Sato, A fully polarimetric borehole radar based numerical modeling: Fully polarimetric response to synthetic natural fractures, in *Progress in Electromagnetics Research Symposium*, Cambridge, UK, 2010, pp. 66–70.

[36] K. Mansour and M. Sato, Subsurface fracture characterisation using full polarimetric borehole radar data analysis with numerical simulation validation, *Exploration Geophysics*, vol. 43, no. 4, pp. 125–135, 2012.

[37] K. Mansour, A. Basheer, T. Rabeh, A. Khalil, A. A. Eldin, and M. Sato, Geophysical assessment of the hydraulic property of the fracture systems around Lake Nasser–Egypt: In sight of polarimetric borehole radar, *NRIAG Journal of Astronomy and Geophysics*, vol. 4, no. 6, pp. 7–17, 2014.

[38] Y.-H. Chen and M. L. Oristaglio, A modeling study of borehole radar for oil-field applications, *Geophysics*, vol. 67, no. 5, pp. 1486–1494, 2002.

[39] W. M. Heigl and M. Peeters, Can we obtain invasion depth with directional borehole radar? *Petrophysics*, vol. 46, no. 1, pp. 52–61, 2005.

[40] M. Miorali, F. Zhou, E. Slob, and R. Arts, Coupling ground penetrating radar and fluid flow modeling for oilfield monitoring applications, *Geophysics*, vol. 76, no. 3, pp. A21–A25, 2011.

[41] M. Miorali, E. Slob, and R. Arts, A feasibility study of borehole radar as a permanent downhole sensor, *Geophysical Prospecting*, vol. 59, no. 1, pp. 120–131, 2011.

[42] D. Oloumi, M. I. Pettersson, P. Mousavi, and K. Rambabu, Imaging of oil-well perforations using UWB synthetic aperture radar, *IEEE Transactions on Geoscience and Remote Sensing*, vol. 53, no. 8, pp. 4510–4520, 2015.

[43] J. Wu, C. Torres-Verdín, K. Sepehrnoori, and M. A. Proett, The influence of water-base mud properties and petrophysical parameters on mudcake growth, filtrate invasion, and formation pressure, *Petrophysics*, vol. 46, no. 1, pp. 14–32, 2005.

[44] https://petrowiki.org/Drilling_fluid_types, accessed on 06/05/2020.

[45] D. Navarro, Effects of invasion transient on resistivity time-lapsed logging, Master's thesis, University of Houston, Houston, Texas, USA, 2007.

[46] D. Allen, F. Auzerais, E. Dussan, P. Goode, and R. Williams, Invasion revisited, *Oilfield Review*, vol. 3, no. 3, pp. 10–23, 1991.

[47] C. Torres-Verdín, F. O. Alpak, and T. M. Habashy, Petrophysical inversion of borehole array-induction logs: Part II—Field data examples, *Geophysics*, vol. 71, no. 5, pp. G261–G268, 2006.

[48] J. M. Salazar and C. Torres-Verdín, Quantitative comparison of processes of oil- and water-based mud-filtrate invasion and corresponding effects on borehole resistivity measurements, *Geophysics*, vol. 74, no. 1, pp. E57–E73, 2008.

[49] L. Liang, A. Abubakar, and T. M. Habashy, Estimating petrophysical parameters and average mud-filtrate invasion rates using joint inversion of induction logging and pressure transient data, *Geophysics*, vol. 76, no. 2, pp. E21–E34, 2011.

[50] F. Zhou, X.-Y. Hu, Q.-X. Meng, X.-D. Hu, Z.-Y. Liu, Model and method of permeability evaluation based on mud invasion effects, *Applied Geophysics*, vol. 12, no. 4, pp. 482–492, 2015.

[51] C. E. Robison, Overcoming the challenges associated with the life cycle management of multilateral wells: Assessing moves towards the "intelligent well", in *Offshore Technology Conference*, Houston, Texas, USA, 1997, pp. 399–408.

[52] E. Addiego-Guevara, M. D. Jackson, and M. A. Giddins, Insurance value of intelligent well technology against reservoir uncertainty, in *Symposium on Improved Oil Recovery*, Tulsa, Oklahoma, USA, 2008, SPE-113918-MS.

[53] T. Unneland, Y. Manin, and F. Kuchuk, Permanent gauge pressure and rate measurements for reservoir description and well monitoring: Field cases, *SPE Reservoir Evaluation & Engineering*, vol. 1, no. 3, pp. 224–230, 1998.

[54] T. K. Kragas, F. X. Bostick, C. Mayeu, D. Gysling, and A. M. van der Spek, Downhole fiber-optic flowmeter: Design, operating principle, testing, and field installations, *SPE Production & Facilities*, vol. 18, no. 4, pp. 257–268, 2003.

[55] M. J. Webster, S. M. Richardson, C. Gabard-Cuoq, J. Fitzgerald, and K. E. Stephenson, Well surveillance with a permanent downhole multiphase flowmeter, *SPE Production & Operations*, vol. 21, no. 3, pp. 388–393, 2006.

[56] G. H. Aggrey, D. R. Davies, and L. T. Skarsholt, A novel approach of detecting water influx time in multi-zone and multi-lateral completions using real-time downhole pressure data, in *Middle East Oil and Gas Show and Conference*, Manama, Bahrain, 2007, SPE-105374-MS.

[57] D. Lumley and R. Behrens, Practical issues of 4D seismic reservoir monitoring: What an engineer needs to know, *SPE Reservoir Evaluation & Engineering*, vol. 1, no. 6, pp. 528–538, 1998.

[58] J. H. Saunders, M. D. Jackson, and C. C. Pain, Fluid flow monitoring in oil fields using downhole measurements of electrokinetic potential, *Geophysics*, vol. 73, no. 5, pp. E165–E180, 2008.

[59] G. Watts, O. Barkved, and J. Dickens, Seismic surveillance in the field of the future, in *Intelligent Energy Conference and Exhibition*, Amsterdam, The Netherlands, 2006, SPE-99827-MS.

[60] J. D. Jansen, A. M. Wagenvoort, V. S. Droppert, R. Daling, and C. A. Glandt, Smart well solutions for thin oil rims: Inflow switching and the smart stinger completion, in *Asia Pacific Oil and Gas Conference and Exhibition*, Melbourne, Australia, 2002, SPE-77942-MS.

[61] http://www.hazardexonthenet.net/article/24896/, accessed on 06/05/2020.

[62] R. M. Butler, *Thermal recovery of oil and bitumen*, Upper Saddle River, New Jersey, USA: Prentice Hall Inc., 1991.

[63] M. Al-Gosayir, T. Babadagli, and J. Leung, Optimization of SAGD and solvent additive SAGD applications: Comparative analysis of optimization techniques with improved algorithm configuration, *Journal of Petroleum Science and Engineering*, vol. 98, pp. 61–68, 2012.

[64] A. K. Wojtanowicz and M. Armenta, Assessment of down-hole water sink technology for controlling water inflow at petroleum wells, *Journal of Energy Resources Technology*, vol. 126, no. 4, pp. 334–341, 2004.

[65] W. Qin and A. K. Wojtanowicz, New cold production technique for heavy oil with strong bottom water drive, *SPE Journal*, vol. 19, no. 2, pp. 270-279, 2014.

[66] W. Qin, A. K. Wojtanowicz, and C. D. White, Analytical design of water-free production in horizontal wells using hodograph method, *Archives of Mining Sciences*, vol. 58, no. 2, pp. 287–300, 2013.

[67] J. A. Huisman, S. S. Hubbard, J. D. Redman, and A. P. Annan, Measuring soil water content with ground penetrating radar: A review, *Vadose Zone Journal*, vol. 2, no. 4, pp. 476–491, 2003.

[68] A. P. Annan, GPR methods for hydrogeological studies, in *Hydrogeophysics*, Y. Rubin, S. S. Hubbard, Eds. Amsterdam, The Netherlands: Springer, 2005, pp. 185–213.

[69] G. P. Tsoflias, T. Halihan, and J. M. Sharp, Monitoring pumping test response in a fractured aquifer using ground-penetrating radar, *Water Resources Research*, vol. 37, no. 5, pp. 1221–1229, 2001.

[70] J. Talley, G. S. Baker, M. W. Becker, and N. Beyrle, Four dimensional mapping of tracer channelization in subhorizontal bedrock fractures using surface ground penetrating radar, *Geophysical Research Letters*, vol. 32, no. 4, pp. 319–325, 2005.

[71] F. D. Day-Lewis, J. W. Lane, and S. M. Gorelick, Combined interpretation of radar, hydraulic, and tracer data from a fractured-rock aquifer near Mirror Lake, New Hampshire, USA, *Hydrogeology Journal*, vol. 14, pp. 1–14, 2006.

[72] C. Gregoire, P. Joesten, and J. Lane, Use of borehole radar reflection logging to monitor steam-enhanced remediation in fractured limestone—Results of numerical modelling and a field experiment, *Journal of Applied Geophysics*, vol. 60, no. 1, pp. 41–54, 2006.

[73] R. Deiana, G. Cassiani, A. Villa, A. Bagliani, and V. Bruno, Calibration of a vadose zone model using water injection monitored by GPR and electrical resistance tomography, *Vadose Zone Journal*, vol. 7, no. 1, pp. 215–226, 2008.

[74] G. P. Tsoflias and M. W. Becker, Ground-penetrating radar response to fracture-fluid salinity: Why lower frequencies are favorable for resolving salinity changes, *Geophysics*, vol. 73, no. 5, pp. J25–J30, 2008.

[75] S. Kuroda, H. Jang, and H. Kim, Time-lapse borehole radar monitoring of an infiltration experiment in the vadose zone, *Journal of Applied Geophysics*, vol. 67, no. 4, pp. 361–366, 2009.

[76] F. Ning, K. Zhang, N. Wu, L. Zhang, G. Li, G. Jiang, Y. Yu, L. Liu, and Y. Qin, Invasion of drilling mud into gas-hydrate-bearing sediments. Part I: effect of drilling mud properties, *Geophysical Journal International*, vol. 193, no. 3, pp. 1370–1384, 2013.

[77] O. Akinsete and D. Adekoya, Effects of mud filtrate invasion on well log measurements, in *SPE Nigeria Annual International Conference and Exhibition*, Lagos, Nigeria, 2016, SPE-184308-MS.

[78] F. O. Alpak, C. Torres-Verdín, and T. M. Habashy, Petrophysical inversion of borehole array-induction logs: Part I–Numerical examples, *Geophysics*, vol. 71, no. 4, pp. F101–F119, 2006.

[79] P. Zhao, R. Qin, H. Pan, M. Ostadhass, and Y. Wu, Study on array laterolog response simulation and mud-filtrate invasion correction, *Advances in Geo-Energy Research*, vol. 3, no. 2, pp. 175–186, 2019.

[80] S. Deng, Q. Sun, H. Li, N. Huo, and X. He, The sensitivity of the array resistivity log to mud filtrate invasion and its primary five-parameter inversion for improved oil water recognition, *Petroleum Science*, vol. 9, no. 3, pp. 29–36, 2012.

[81] F. Zhou, Q.-X. Meng, X.-Y. Hu, E. Slob, H.-P. Pan, and H.-L. Ma, Evaluation of reservoir permeability using array induction logging, *Chinese Journal of Geophysics*, vol. 59, no. 6, pp. 703–716, 2016.

[82] L.-H. Zhang, G.-Q, Liu, C.-C. Zhou, and Z.-C. Liu, Reservoir productivity prediction by array induction logging data, *Petroleum Exploration and Development*, vol. 32, no. 3, pp. 84–87, 2005.

[83] C. Warren, A. Giannopoulos, and I. Giannakis, gprMax: Open source software to simulate electromagnetic wave propagation for Ground Penetrating Radar, *Computer Physics Communications*, vol. 209, pp. 163–170, 2016.

[84] M. Hizem, H. Budan, B. Deville, O. Faivre, L. Mosse, and M. Simon, Dielectric dispersion: A new wireline petrophysical measurement, in *SPE Annual Technical Conference and Exhibition*, Denver, Colorado, USA, 2008, SPE-116130-MS.

[85] N. Allroggen, D. Beiter, and J. Tronicke, Ground-penetrating radar monitoring of fast subsurface processes, *Geophysics*, vol. 76, no. 2, pp. E21–E34, 2020.

[86] S. E. Hamran, D. T. Gjessing, J. Hjelmstad, and E. Aarholt, Ground penetrating synthetic pulse radar: Dynamic range and modes of operation, *Journal of Applied Geophysics*, vol. 33, no. 1, pp. 7–14, 1995.

[87] H. D. Beggs and J. R. Robinson, Estimating the viscosity of crude oil systems, *Journal of Petroleum Technology*, vol. 27, no. 9, pp. 1140–1141, 1975.

[88] J. E. Baur, Diffusion coefficients, in *Handbook of Electrochemistry*, C. G. Zoski, Ed. Amsterdam: Elsevier, 2007, pp. 829–848.

[89] T. Darling, Advanced log interpretation techniques, in *Well Logging and Formation Evaluation*, T. Darling Ed. Amsterdam, The Netherlands: Elsevier, 2005, pp. 67–102.

[90] C. Y. Yao and S. A. Holditch, Estimating permeability profiles using core and log data, in *SPE Eastern Regional Meeting*, Pittsburgh, Pennsylvania, USA, 1993, SPE-26921-MS.

[91] A. Donaldson and G. M. Clydesdale, Accurate reservoir evaluation quality core samples—a good starting point, in *Advances in Core Evaluation*, P. F. Worthington, Ed. New York, USA: Gordon and Breach Science Publishers, 1990, pp. 35–53.

[92] U. Ahmed, S. Crary, and G. Coates, Permeability estimation: The various sources and their interrelationships, *Journal of Petroleum Technology*, vol. 43, no. 5, pp. 578–587, 1991.

[93] P. Glover, I. Zadjali, and K. Frew, Permeability prediction from MICP and NMR data using an electrokinetic approach, *Geophysics*, vol. 71, no. 4, pp. F49–F60, 2006.

[94] F. Zunker, Das verhalten des bodens zum wasser, in *Physikalische Beschaffenheit des Bodens*, A. Densch, F. Giesecke, M. Helbig, V. F. Hess, J. Schubert, and F. Zunker Eds. Amsterdam, The Netherlands: Springer, 1930, pp. 66–220.

[95] P. C. Carman, *Flow of gases through porous media*, Salt Lake City, Utah, USA: Academic Press, 1956.

[96] A. Timur, An investigation of permeability, porosity and residual water saturation relationships for sandstone reservoirs, *The Log Analyst*, vol. 9, no. 4, pp. 8–17, 1968.

[97] G. R. Coates and J. L. Dumanoir, A new approach to improved log-derived permeability, in *SPWLA 14th Annual Logging Symposium*, Lafayette, Louisiana, USA, 1973, SPWLA-1973-R.

[98] H. A. Nooruddin and M. E. Hossain, Modified Kozeny–Carmen correlation for enhanced hydraulic flow unit characterization, *Journal of Petroleum Science and Engineering*, vol. 80, no. 1, pp. 107–115, 2011.

[99] A. Sirait, Permeability estimation based on Cokriged porosity data, Lehigh University, Bethlehem, Pennsylvania, USA, Tech. Rep., 2015.

[100] S. Grude, J. Dvorkin, and M. Landrø, Permeability variation with porosity, pore space geometry, and cement type: A case history from the Snøhvit field, the Barents Sea, *Geophysics*, vol. 80, no. 1, pp. D43–D49, 2014.

[101] X. M. Tang and C. H. Cheng, Fast inversion of formation permeability from Stoneley wave logs using a simplified Biot-Rosenbaum model, *Geophysics*, vol. 61, no. 3, pp. 639–645, 1996.

[102] A. Weller, S. Nordsiek, and W. Debschütz, Estimating permeability of sandstone samples by nuclear magnetic resonance and spectral-induced polarization, *Geophysics*, vol. 75, no. 6, pp. E215–E226, 2010.

[103] J. Tronicke, K. Holliger, W. Barrash, M. D. Knoll, Multivariate analysis of cross-hole georadar velocity and attenuation tomograms for aquifer zonation, *Water Resources Research*, vol. 40, no. 1, W01519, 2004.

[104] J.-G. Zhao and M. Sato, Radar polarimetry analysis applied to single-hole fully polarimetric borehole radar, *IEEE Transactions on Geoscience and Remote Sensing*, vol. 44, no. 12, pp. 3547–3554, 2006.

[105] H. Liu, X. Huang, F. Han, J. Cui, B. F. Spencer, and X. Xie, Hybrid polarimetric GPR calibration and elongated object orientation estimation, *IEEE Journal of Selected Topics in Applied Earth Observations and Remote Sensing*, vol. 12, no. 7, pp. 2080–2087, 2019.

[106] S. Liu, J. Wu, H. Dong, L. Fu, and F. Wang, The experimental results and analysis of a borehole radar prototype, *Journal of Geophysics and Engineering*, vol. 9, no. 2, pp. 201–209, 2012.

[107] H.-Y. Liang, H.-C. Yang, and J. Zhang, A cylindrical conformal directional monopole antenna for borehole radar application, *IEEE Antennas and Wireless Propagation Letters*, vol. 11, pp. 1525–1528, 2012.

[108] C. Ma, Q. Zhao, J. Huo, X. Chang, and L. Ran, Single borehole radar for well logging in a limestone formation: Experiments and simulations, *Journal of Environmental and Engineering Geophysics*, vol. 21, no. 4, pp. 201–213, 2016.

[109] D. Oloumi, J. Ting, and K. Rambabu, Design of pulse characteristics for near-field UWB–SAR imaging, *IEEE Transactions on Microwave Theory and Techniques*, vol. 64, no. 8, pp. 2684–2693, 2016.

[110] J. K. Fink, Drilling muds, in *Petroleum engineer's guide to oil field chemicals and fluids*, 2nd ed., J. K. Fink, Ed. Boston, Massachusetts, USA: Gulf Professional Publishing, 2015, pp. 1–61.

[111] J. van Lookeren, Oil production from reservoirs with an oil layer between gas and bottom water in the same sand, *Journal of Petroleum Technology*, vol. 17, no. 3, pp. 354–357, 1965.

[112] F. Zhou, Reservoir dynamic monitoring using borehole radar and its application in smart well production, Ph.D. thesis, China University of Geosciences (Wuhan), Wuhan, China, 2011.

[113] A. Y. Gunawan, P. Sukarno, and E. Soewono, Modeling of mud filtrate invasion and damage zone formation, *Journal of Petroleum Science and Engineering*, vol. 77, no. 3, pp. 359–364, 2011.

[114] K. Aziz, *Petroleum reservoir simulation*, Amsterdam, The Netherlands: Elsevier, 1979.

[115] M. Delshad and G. A. Pope, Comparison of the three-phase oil relative permeability models, *Transport in Porous Media*, vol. 4, no. 1, pp. 59–83, 1989.

[116] B. K. George, C. Torres-Verdín, M. Delshad, R. Sigal, F. Zouioueche, and B. Anderson, A case study integrating the physics of mud-filtrate invasion with the physics

of induction logging: Assessment of in-situ hydrocarbon saturation in the presence of deep invasion and highly saline connate water, in *SPWLA 44th Annual Logging Symposium*, Galveston, Texas, USA, 2003, SPWLA-2003-K.

[117] Y.-H. Chen, R. T. Coates, and W. C. Chew, FDTD modeling and analysis of a broadband antenna suitable for oil-field imaging while drilling, *IEEE Transactions on Geoscience and Remote Sensing*, vol. 40, no. 2, pp. 434–442, 2002.

[118] S. Liu, J. Liu, X. Dong, and Y. Duan, *Electromagnetic wave shielding and absorbing materials (in China)*. Beijing, China: Chemical Industry Press, 2014.

[119] W. C. Chin, *Electromagnetic Well Logging: Models for MWD/LWD Interpretation and Tool Design*, Austin, Texa, USA: Wiley-Scrivener, 2002.

[120] M. Sato and T. Miwa, Polarimetric borehole radar system for fracture measurement, *Sensing and Imaging*, vol. 1, no. 1, pp. 161–175, 2000.

[121] A. Taflove and S. C. Hagness, *Computational electrodynamics: The finite-difference time-domain method*, Boston, Massachusetts, USA: Artech House, 2005.

[122] A. Giannopoulos, Unsplit implementation of higher order PMLs, *IEEE Transactions on Antennas and Propagation*, vol. 60, no. 3, pp. 1479–1485, 2012.

[123] I. Giannakis and A. Giannopoulos, Time-synchronized convolutional perfectly matched layer for improved absorbing performance in FDTD, *IEEE Antennas and Wireless Propagation Letters*, vol. 14, pp. 690–693, 2014.

[124] J. Donadille and O. Faivre, Water complex permittivity model for dielectric logging, in *SPE Middle East Oil and Gas Show and Conference*, Manama, Bahrain, 2015, SPE-172566-MS.

[125] R. Murphy and W. Owens, Time-lapse logging, a valuable reservoir evaluation technique, *Journal of Petroleum Technology*, vol. 16, no. 1, pp. 15–19, 1964.

[126] D. Daniels, D. Gunton, and H. Scott, Introduction to subsurface radar, *IEE Proceedings F (Communications, Radar and Signal Processing)*, vol. 135, no. 4, pp. 278–320, 1988.

[127] M. Sato and T. Takayama, A novel directional borehole radar system using optical electric field sensors, *IEEE Transactions on Geoscience and Remote Sensing*, vol. 45, no. 8, pp. 2529–2535, 2007.

[128] H. Zhou and M. Sato, Application of vertical radar profiling technique to Sendai Castle, *Geophysics*, vol. 65, no. 2, pp. 533–539, 2000.

[129] K. J. Ellefsen, A. T. Mazzella, R. J. Horton, and J. R. McKenna, Phase and amplitude inversion of crosswell radar data, *Geophysics*, vol. 76, no. 3, pp. J1–J12, 2011.

[130] H. Yang, T. Li, N. Li, Z. He, and Q. H. Liu, Efficient near-field imaging for single-borehole radar with widely separated transceivers, *IEEE Transactions on Geoscience and Remote Sensing*, vol. 53, no. 10, pp. 1–11, 2015.

[131] J.-G. Zhao and M. Sato, Consistency analysis of subsurface fracture characterization using different polarimetry techniques by a borehole radar, *IEEE Geoscience and Remote Sensing Letters*, vol. 4, no. 3, pp. 359–363, 2007.

[132] J.-G. Zhao and M. Sato, Experimental implementation and assessment of two polarimetric calibration approaches applied for a fully polarimetric borehole radar, *Journal of Geophysics and Engineering*, vol. 5, no. 2, pp. 232–243, 2008.

[133] C. Guo and R. C. Liu, A borehole imaging method using electromagnetic short pulse in oil-based mud, *IEEE Geoscience and Remote Sensing Letters*, vol. 7, no. 4, pp. 856–860, 2010.

[134] H.-Y. Liang, H.-C. Yang, J. Hou, and L.-Y Cai, A compact ferrite-based dipole directional antenna for borehole radar application, *IEEE Geoscience and Remote Sensing Letters*, vol. 10, no. 3, pp. 486–489, 2013.

[135] C. A. Glandt, Reservoir management employing smart wells: A review, *SPE Drilling & Completion*, vol. 20, no. 4, pp. 281–288, 2005.

[136] M. Konopczynski and A. Ajayi, Design of intelligent well downhole valves for adjustable flow control, in *Annual Technical Conference and Exhibition*, Houston, Texas, USA, 2004, 90664-MS.

[137] S. Dyer, Y. El-Khazindar, M. Huber, I. Raw, and D. Reed, Intelligent completions—A hands-off management style, *Oilfield Review*, vol. 19, no. 4, pp. 4–17, 2007.

[138] S. M. Elmsallati, D. R. Davies, and S. M. Erlandsen, A case study of value generation with intelligent well technology in a high productivity, thin oil rim reservoir, in *Middle East Oil and Gas Show and Conference*, Bahrain, 2005, SPE-94995-MS.

[139] F. A. Dilib, M. D. Jackson, A. M. Zadeh, R. Aasheim, K. Årland, A. J Gyllensten, and S. M Erlandsen, Closed-loop feedback control in intelligent wells: Application to a heterogeneous thin oil-rim reservoir in the North Sea, *SPE Reservoir Evaluation & Engineering*, vol. 18, no. 1, pp. 69–83, 2015.

[140] R. V. D. Poel and J. D. Jansen, Probabilistic analysis of the value of a smart well for sequential production of a stacked reservoir, *Journal of Petroleum Science and Engineering*, vol. 44, no. 1, pp. 155–172, 2004.

[141] F. Zhou, X. Hu, and J. Liu, Comparative study of feedback control policies in water flooding production, *Journal of Natural Gas Science and Engineering*, vol. 27, pp. 1348–1356, 2015.

[142] D. E. Lumley, Time-lapse seismic reservoir monitoring, *Geophysics*, vol. 66, no. 1, pp. 50–53, 2001.

[143] P. Gagliardi and D. C. Lawton, Orientation analysis of borehole geophones: Calibration consistency, in *82th Annual International Meeting*, Las Vegas, Nevada, USA, 2012, SEG-2012-1258.

[144] M. F. Silva, K. M. Muradov, and D. R. Davies, Review, analysis and comparison of intelligent well monitoring systems, in *SPE Intelligent Energy International*, Utrecht, The Netherlands, 2012, SPE-150195-MS.

[145] A. Reitz, R. Krahenbuhl, and Y. Li, Feasibility of time-lapse gravity and gravity gradiometry monitoring for steam-assisted gravity drainage reservoirs, *Geophysics*, vol. 80, no. 2, pp. WA99–WA111, 2015.

[146] A. Black, J. Hare, and J. Macqueen, Borehole gravity monitoring in the aquistore CO2 sequestration well, in *86th SEG Annual International Meeting*, Dallas, Texas, USA, 2016, pp. 768–772.

[147] J. Vinogradov and M. D. Jackson, Multiphase streaming potential in sandstones saturated with gas/brine and oil/brine during drainage and imbibition, *Geophysical Research Letters*, vol. 38, no. 1, pp. 121–133, 2011.

[148] J. H. Saunders, M. D. Jackson, M. Y. Gulamali, J. Vinogradov, and C. C. Pain, Streaming potentials at hydrocarbon reservoir conditions, *Geophysics*, vol. 77, no. 1, pp. E77–E90, 2012.

[149] F. Ebadi and D. R. Davies, Should "Proactive" or "Reactive" control be chosen for intelligent well management?, in *Intelligent Energy Conference and Exhibition*, Amsterdam, The Netherlands, 2006, SPE-99929-MS.

[150] J. M. M. Regtien, M. T. van Stiphout, and F. F. van der Vlugt, Interactive reservoir simulation, in *13th SPE Reservoir Simulation Symposium*, San Antonio, Texas, USA, 1995, SPE-29146-MS.

[151] M. H. W. Verbruggen, Influence of permeability and porosity variations on horizontal well behaviour: Application of geostatistical modelling on reservoirs in the Nimr field, Shell International Exploration and Production Inc., The Hague, The Netherlands, Tech. Rep., 2005.

[152] A. Giannopoulos, Modelling ground penetrating radar by GprMax, *Construction and Building Materials*, vol. 19, no. 10, pp. 755–762, 2005.

[153] Y. Ren, Y. Wang, M. Wang, S. Wu, and B. Wei, A measuring system for well logging attitude and a method of sensor calibration, *Sensors*, vol. 14, no. 5, pp. 9256–9270, 2014.

[154] L. C. Shen, A laboratory technique for measuring dielectric properties of core samples at ultrahigh frequencies, *SPE Journal*, vol. 25, no. 4, pp. 502–514, 1985.

[155] L. Mosse, R. Carmona, E. Decoster, O. Faivre, M. Hizem, Dielectric dispersion logging in heavy oil: A case study from the Orinoco Belt, in *SPWLA 50th Annual Logging Symposium*, The Woodlands, Texas, USA, 2009, SPWLA-2009-52901.

[156] I. D. Bryant, M. Y. Chen, B. Raghuraman, I. Raw, J. P. Delhomme, C. Chouzenoux, D. Pohl, Y. Manin, E. Rioufol, G. Oddie, D. Swager, and J. Smith, An application of cemented resistivity arrays to monitor waterflooding of the Mansfield Sandstone,

Indiana, USA, *SPE Reservoir Evaluation & Engineering*, vol. 5, no. 6, pp. 447–454, 2002.

[157] B. Raghuraman, B. Couet, P. Savundararaj, W. J. Bailey, and D. J. Wilkinson, Valuation of technology and information for reservoir risk management, *SPE Reservoir Evaluation & Engineering*, vol. 6, no. 5, pp. 307–316, 2003.

[158] I. D. Bryant, M. Y. Chen, B. Raghuraman, R. Schroeder, M. Supp, J. Navarro, I. Raw, J. Smith, and M. Scaggs, Real-time monitoring and control of water influx to a horizontal well using advanced completion equipped with permanent sensors, *SPE Drilling & Completion*, vol. 19, no. 4, pp. 253–264, 2004.

[159] F. A. Dilib and M. D. Jackson, Closed-loop feedback control for production optimization of intelligent wells under uncertainty, *SPE Production & Operations*, vol. 28, no. 04, pp. 345–357, 2013.

[160] E. Addiego-Guevara, Quantifying the value of reactive and proactive feedback control strategies for intelligent wells, Ph.D. thesis, Imperial College London, London, UK, 2009.

[161] A. Vengosh, R. B. Jackson, N. Warner, T. H. Darrah, and A. Kondash, A critical review of the risks to water resources from unconventional shale gas development and hydraulic fracturing in the United States, *Environmental Science & Technology*, vol. 48, no. 15, pp. 8334–8348, 2014.

[162] T. Babadagli, Technology focus: Heavy oil, *Journal of Petroleum Technology*, vol. 57, no. 6, SPE-0605-0062-JPT, 2005.

[163] M. Delshad and G. A. Pope, Comparison of the three-phase oil relative permeability models, *Transport in Porous Media*, vol. 4, no. 1, pp. 59–83, 1989.

[164] G. E. Archie, The electrical resistivity log as an aid in determining some reservoir characteristics, *Transaction of American Institute of Mining, Metallurgical, and Petroleum Engineers*, vol. 146, no. 1, pp. 54–62, 1942.

[165] R. M. Bateman and C. E. Konen, The log analyst and the programmable pocket calculator, *The Log Analyst*, vol. 19, no. 3, pp. 3–7, 1978.

[166] J. R. Birchak, C. G. Gardner, J. E. Hipp, and J. M. Victor, High dielectric constant microwave probes for sensing soil moisture, *Proceedings of the IEEE*, vol. 62, no. 1, pp. 93–98, 1974.

LIST OF PUBLICATIONS

Publications only related to the theme of the thesis are listed here.

Journal Publications

1. F. Zhou, X.-Y. Hu, Q.-X. Meng, X.-D. Hu, and Z.-D. Liu, Model and method of permeability evaluation based on mud invasion effects, *Applied Geophysics*, vol. 12, no. 4, pp. 482–492, 2015.

2. F. Zhou, X. Hu, and J. Liu, Comparative study of feedback control policies in water flooding production, *Journal of Natural Gas Science and Engineering*, vol. 27, pp. 1348–1356, 2016.

3. F. Zhou, Q.-X. Meng, X.-Y. Hu, E. Slob, H.-P. Pan, and H.-L. Ma, Evaluation of reservoir permeability using array induction logging, *Chinese Journal of Geophysics*, vol. 59, no. 6, pp. 1348–1356, 2016.

4. F. Zhou, M. Miorali, E. Slob, and X. Hu, Reservoir monitoring using borehole radars to improve oil recovery: Suggestions from 3D electromagnetic and fluid modeling, *Geophysics*, vol. 83, no. 2, pp. WB19–WB32, 2018.

5. F. Zhou, I. Giannakis, A. Giannopoulos, K. Holliger, and E. Slob, Estimating reservoir permeability with borehole radar, *Geophysics*, vol. 85, no. 4, pp. H51–H60, 2020.

6. F. Zhou, I. Giannakis, A. Giannopoulos, K. Holliger, and E. Slob, Extracting mud invasion signals from borehole radar measurements, *Geophysics*, under review.

Conferences

1. F. Zhou, X. Hu, I. Giannakis, A. Giannopoulos, K. Holliger, and E. Slob, Borehole radar response of a mud-invaded oil-bearing layer, in *EGU General Assembly 2019*, Vienna, Austria, 2019, EGU2019-18861.

2. F. Zhou, I. Giannakis, A. Giannopoulos, and E. Slob, Associating borehole radar imaging with petrophysical properties for a mud-contaminated reservoir, in *Near Surface Geoscience Conference and Exhibition 2019*, The Hague, Netherlands, 2019, We_10GPR_03.

3. F. Zhou, I. Giannakis, A. Giannopoulos, K. Holliger, and E. Slob, Effects of petrophysical properties on time-lapse borehole radar logging, in *18th International Conference on Ground Penetrating Radar*, to be published by SEG.

CURRICULUM VITÆ

Feng ZHOU

Feng Zhou was born in Hubei Province, China in 1979. In 2002, he received a B.Sc. degree in Telecommunication Engineering at The Second Artillery Command College, China. In 2007, he completed an M.Sc. degree in Solid Earth Geophysics at China University of Geosciences (Wuhan). Thereafter, he pursued his Ph.D. study at the same university and completed his first doctorate degree in 2011. From Oct. 2009 to Nov. 2010, he worked at Delft University of Technology as a visiting scholar, funded by a NUFFIC grant. In 2013, under the supervision of Prof. Evert Slob, he started pursuing his second doctorate degree in Geophysics and Petrophysics at Delft University of Technology. His research areas to date include ground-penetrating radar, borehole geophysics, reservoir simulations, and their engineering applications.

ACKNOWLEDGMENTS

As a traditional saying goes, “If you want to go quickly, go alone. If you want to go far, go together.” This is more than true over my long Ph.D. journey. Words are never sufficient to express my gratitude, but I would like to take this chance to show my appreciation to all those who have helped me towards the completion of my Ph.D. thesis. This thesis is thus sincerely dedicated to my supervisor, friends, fellows and family.

To Prof. Evert slob, the first one I want to express my thanks. It took me plenty for getting this valuable chance to study at TU Delft. Through years of efforts, I managed to be granted NUFFIC funding. This was my first experience of working with Evert at TU Delft as a visiting Ph.D. researcher, while I was doing Ph.D. at China University of Geoscience (Wuhan). One year later following my visit, I completed my first Ph.D. in China. However, my eagerness to further broaden my expertise in the areas urged me to pursue a second Ph.D. at TU Delft in the research group of Evert’s. In particular, it was his support and help that brought me to TU Delft again, from which I started my Ph.D. journey in the Netherlands. To be honest, the journey is not smooth. My very first publication in Geophysics took six years. The efforts and patients of Evert in guiding me in this process gave me a valuable training of writing, critical thinking and, most importantly, a cautious attitude to research. Also, He is always open for my questions, which I really appreciate. Evert is not only my advisor in research but also a mentor in my life. For numerous times, I doubted whether I could reach the destination. It was his kind words that gave me courage and confidence to move forward. Furthermore, his treatment to me as a friend makes my stay in the Netherlands very comfortable. All these will be great memories along with me wherever I go. I believe the completion of my Ph.D. is not the end but a new starting for our collaboration.

I am very grateful for the other people that have helped me directly to carry out my research and finally this thesis. I would express my gratitude to my former colleague, Dr. Mattia Miorali (now at CGG). We have worked together for more than one year on the ISAPP (Integrated System Approach Petroleum Production) project. A lot of my lessons in the areas were learned from him. The publication of my very first paper in Geophysics was accredited to him as well. I am very thankful to Prof. Antonis Giannopoulos at the University of Edinburgh. Thanks for hosting me over three months of study on gprMax in his group. I have been using gprMax for years and witnessed its upgrading from 2.0 to 3.0 version. Please allow me, if I may, on behalf of the GPR community, to give a salute to Antonis for his dedication to gprMax—a great fortune which continues to benefit the entire community. I also express my gratitude to the other gprMax developers, Dr. Craig Warren at Northumbria University, and Dr. Iraklis Giannakis at the University of Aberdeen, for the priceless help on my gprMax modelling. I am very thankful to Prof. Klaus Holliger at the University of Lausanne for his inputs on borehole geophysics. I am

deeply impressed by his modesty and critical attitude to research. He set a good model in my pursuit of an academic career. I thank Dr. Ernesto Addiego-Guevara at Imperial College London for sharing his MoReS (Modular Reservoir Simulator) templates to simulate smart well productions. I would express my gratitude to Ms. Weronika Filinger at the University of Edinburgh and Mr. Jianhuan Liu at Delft University of Technology for the assistance in high-performance computing.

I acknowledge Sinopec Petroleum E&P Institute for the permission of using oil field logging and coring data. The research was funded by National Natural Science Foundation of China (41304078, 41674138, 41811530749), NWO (Netherlands Organisation for Scientific Research) Cooperation and Exchange Fund (040.22.011/7048), HPC-EUROPA3 project (INFRAIA-2016-1-730897), and China Scholarship Council grant (201806415048). I thank Shell for the permission to use the reservoir simulator MoReS in the framework of ISAPP.

To my colleagues, thanks for all the beautiful memories at TU Delft. In particular, thanks to my officemates: Lele Zhang, Binkun Yang, Youwei Wang, and Jianhuan Liu. It is my pleasure to have their accompany for both happy and sorrowful moments. Thanks to Dr. Jinyu Tang and Mr. Xiaocong Lyu in the Section of Petroleum Engineering. They gave me a lot of valuable suggestions on fluid modelling. Thanks to Musab Al Hasani and Max Holicki. They are my sincere friends that I will never forget. Thanks to all those that I have met in the Netherlands during my Ph.D. study. Their kindness and hospitality will be my eternal memories in this beautiful country and will be with me during all my life.

Last but not least, I owe a big thank to my parents and sister for all their love, support and tolerance, but never asking for any return. No words can fully express my gratitude to them. I never said this before, but today, I want to say “I love you”.

Yours Sincerely,

Feng Zhou
1 July 2020
Wuhan, China

Propositions

accompanying the dissertation

NOVEL APPLICATIONS OF GROUND-PENETRATING RADAR IN OIL FIELDS

by

Feng ZHOU

1. Application requirements drive development of novel technologies rather than technologies drive applications (This proposition pertains to this dissertation).
2. Accurate acquirement of mud invasion depth derives a precise estimation of reservoir permeability (This proposition pertains to Chapters 2 and 3 of this dissertation).
3. Adequate information of downhole monitoring actuates an optimized oil recovery strategy (This proposition pertains to Chapter 4 of this dissertation).
4. Every disadvantage has its advantage; this certainly holds for mud invasion (This proposition pertains to Chapter 3 of this dissertation).
5. It's only a dream until you write it down, and then it becomes a goal.
6. One should learn to take life as it comes!
7. It does not matter how slowly you go as long as you do not stop.
8. It is not because things are difficult that we do not dare, it is because we do not dare that things are difficult.
9. You should gracefully accept the curtain fall and appreciate your efforts irrespective of the level of applause.
10. A journey of a thousand miles begins with a single step (千里之行，始于足下) — from *Tao Te Ching* by Laozi.

These propositions are regarded as opposable and defendable, and have been approved as such by the promotor prof. dr. ir. Evert Slob.

551836-L-st-Zhou
Processed on: 27-11-2020